STATUS OF THESIS

Title of thesis	A computational approach for the modeling of short-fiber orientation in a viscous flow during the mold-filling process using different closure approximations

I _____ SUREN LIM SINNADURAI _____

hereby allow my thesis to be placed at the Information Resource Center (IRC) of

Universiti Teknologi PETRONAS (UTP) with the following conditions:

1. The thesis becomes the property of UTP.

2. The IRC of UTP may make copies of the thesis for academic purposes only.

3. This thesis is classified as

    ☐ Confidential

    ☑ Non-confidential

If this thesis is confidential, please state the reason:
_____-_____

The contents of the thesis will remain confidential for _____-_____ years.

Remarks on disclosure:
_____-_____

_____

_____

                                              Endorsed by

_____   _____
Signature of Author   Signature of Supervisor

No. 4 Jalan Taman Jaya,   Dr. Ahmed Maher S. Ali
Jalan Pusara,
20400, Kuala Terengganu,
Terengganu Darul Iman

Date:_____   Date:_____

UNIVERSITI TEKNOLOGI PETRONAS

DISSERTATION TITLE: A COMPUTATIONAL APPROACH FOR THE
MODELING OF SHORT-FIBER ORIENTATION IN A VISCOUS FLOW
DURING THE MOLD-FILLING PROCESS USING DIFFERENT CLOSURE
APPROXIMATIONS

By

SUREN LIM SINNADURAI

The undersigned certify that they have read, and recommend to The Postgraduate

Studies Programme for acceptance, for the fulfillment of the requirements for the

degree stated.

Signature: _____

Main supervisor: Dr. Ahmed Maher S. Ali _____

Signature: _____

Co-Supervisor: Dr. Shiraz M. Aris _____

Signature: _____

Head of Department: Assoc. Prof. Dr. Ahmad Majdi Abdul Rani _____

Date: _____

ii

DISSERTATION TITLE: A COMPUTATIONAL APPROACH FOR THE
MODELING OF SHORT-FIBER ORIENTATION IN A VISCOUS FLOW
DURING THE MOLD-FILLING PROCESS USING DIFFERENT CLOSURE
APPROXIMATIONS

by

SUREN LIM SINNADURAI

A Thesis

Submitted to the Postgraduates Studies Programme

as a Requirement for the Degree of

MASTER OF SCIENCE

MECHANICAL ENGINEERING

UNIVERSITI TEKNOLOGI PETRONAS

BANDAR SERI ISKANDAR,

PERAK

MAY 2011

DECLARATION OF THESIS

Title of thesis

> A computational approach for the modeling of short-fiber orientation in a viscous flow during the mold-filling process using different closure approximations

I _____ SUREN LIM SINNADURAI _____

hereby declare that the thesis is based on my original work except for quotations and citations which have been duly acknowledged. I also declare that it has not been previously or concurrently submitted for any other degree at UTP or other institutions.

Witnessed by

_____   _____

Signature of Author   Signature of Co-Supervisor

No. 4 Jalan Taman Jaya,   Dr. Shiraz M. Aris
Jalan Pusara,
20400, Kuala Terengganu,
Terengganu Darul Iman

Date: _____   Date:_____

ACKNOWLEDGEMENTS

ABSTRACT

The last half century has seen an increase in the use of fiber composites in many areas. One such class of composites is Short Fiber Reinforced Thermoplastics (SFRT), well known for their versatility in various applications. However, the physical properties of the finished molding are highly dependent upon the fiber orientation, which in turn is heavily influenced by the processing conditions. It is thus of interest to model the mold-filling process and compute the resulting fiber orientation due to the flow field that develops within the mold. This was done in this research in three stages. In the first stage, the mold-filling flow was modeled as a non-isothermal, incompressible, non-Newtonian fluid in a three-dimensional flow. The flow equations were solved numerically using the commercial Computational Fluid Dynamics (CFD) code, FLUENT 6.3. The simulation setup was validated by means of comparison with a numerical test case from literature. In the second stage, the fiber orientation evolution equation was discretized and numerically solved in Matlab, utilizing coefficients obtained from data imported from FLUENT. The third stage included a comparison of the performances of three closure models; linear, quadratic and hybrid, used to complete the fiber orientation evolution equation. The experimental data set was obtained from literature and it consisted of fiber orientation measurements from an injection molded, film-gated rectangular strip. For all three closure models, the dominant orientation component was directed along the flow direction – the a_{11} orientation tensor. The numerically computed a_{11} orientation tensor produced results which agreed well with the experimental data where the typical deviation range observed was about 45%. For the non-dominant components: a_{22}, a_{33} and a_{13} the simulation results demonstrated better agreement with the experimental data set, however there was a broader range of deviation among the three closures than was observed with the a_{11} component. From an analysis of the deviation trends for all three closure models, it was concluded that for the film-gated mold geometry simulated here, the linear closure model performed best. A qualitative comparison of the numerical and experimental data trends showed that

the hybrid closure model demonstrated over-prediction of the a_{11} orientation in regions of high shear rate in the flow. In regions of low shear rate, near the mid-plane of the flow, all three models demonstrated significant under-prediction of the a_{11} orientation. The highest degree of agreement between the numerically obtained a_{11} orientation and experimental data occurred in regions of high shear for all three closures. From the analyses performed it is clear that the simulation results were in qualitative agreement with the experimental data. Nevertheless the observed deviations between simulation and experiment highlight the importance of coupling effects between the fluid momentum and fiber orientation as well as the necessity of accurate closure models.

ABSTRAK

Penggunaan komposit gentian dalam pelbagai bidang telah melihat peningkatan dalam lima dekad akhir abad ke-20. Salah satu kelas komposit gentian ini ialah komposit gentian halus, yang secara umumnya diketahui mempunyai aplikasi yang meluas. Walau bagaimanapun, sifat fizikal komposit yang dihasilkan sangat bergantung kepada orientasi gentian halus dalam komposit tersebut. Orientasi gentian ini pula mengalami perubahan yang bergantung kepada keadaan di dalam acuan sewaktu pemprosesan. Oleh yang demikian, keadaan ini telah merangsang kajian untuk menghasilkan model bagi meramal perubahan orientasi gentian halus yang berlaku semasa pemprosesan berlangsung. Dalam thesis ini, kajian dijalankan dalam tiga peringkat. Pertama, aliran bahan cair di dalam acuan dimodelkan sebagai bendalir yang mampat, bukan Newtonian dan mengalami perubahan suhu. Simulasi ini dijalankan untuk geometri tiga-dimensi menggunakan perisian komersial iaitu FLUENT 6.3 dan dibandingkan dengan hasil dari kajian lain untuk menguji ketepatan simulasi tersebut. Kedua, persamaan matematik yang menggambarkan perubahan orientasi gentian halus diselesaikan secara numerik dalam perisian Matlab, menggunakan data yang diperolehi daripada simulasi FLUENT. Tahap ketiga kajian ini melibatkan perbandingan antara model 'closure' yang digunakan untuk melengkapkan persamaan orientasi tersebut. Tiga model 'closure' yang dibincangkan dalam tesis ini ialah model linear, kuadratik dan hibrid. Data eksperimen yang membolehkan perbandingan antara tiga model tersebut diperolehi daripada kajian lepas yang telah diterbitkan. Data ini mengandungi bacaan eksperimen untuk empat komponen orientasi untuk komposit yang dibentuk dalam acuan segi-empat. Bagi kesemua model 'closure' yang diuji, komponen a_{11} iaitu komponen orientasi yang dominan menghasilkan trend yang menyerupai data eksperimen. Bagi komponen orientasi yang bukan dominan pula: a_{22}, a_{33} dan a_{13} data yang diperolehi turut menyerupai data eksperimen. Bagaimanapun, bagi ketiga-tiga model 'closure', perbezaan antara trend yang diperoleh agak ketara berbanding trend yang diperolehi untuk komponen a_{11}. Daripada analisis yang dijalankan, model linear

dilihat sebagai model 'closure' yang menghasilkan prestasi yang paling baik secara keseluruhan. Model hibrid pula meramalkan nilai a_{11} yang lebih tinggi daripada nilai eksperimental dalam bahagian aliran yang mempunyai stres bendalir yang tinggi. Di bahagian yang mempunyai stres bendalir yang rendah seperti di tengah-tengah acuan, kesemua model 'closure' menghasilkan nilai a_{11} yang lebih rendah berbanding data eksperimen. Persamaan antara data numerik dan eksperimen dilihat lebih ketara di bahagian aliran yang mempunyai stres bendalir yang tinggi. Analisis yang menyeluruh menemui bahawa simulasi yang dijalankan menghasilkan data yang mirip dengan data eksperimen. Bagaimanapun, perbezaan antara kedua-dua set data ini turut menonjolkan kepentingan menghubungkan momentum bendalir dengan orientasi gentian serta keperluan untuk model 'closure' yang tepat.

In compliance with the terms of the Copyright Act 1987 and the IP Policy of the university, the copyright of this thesis has been reassigned by the author to the legal entity of the university,

<p style="text-align:center">Institute of Technology PETRONAS Sdn Bhd.</p>

Due acknowledgement shall always be made of the use of any material containedin, or derived from, this thesis.

TABLE OF CONTENTS

LIST OF TABLES

LIST OF FIGURES

xvii

LIST OF ABBREVIATIONS

SFRT – short fiber reinforced thermoplastic

CFD – computational fluid dynamics

CV – control volume

PRESTO – pressure staggering option

VOF – volume of fluid

SIMPLE – semi-implicit pressure linked equations

PISO – pressure implicit with splitting of operators

HRIC – high resolution interface capturing

UDF – user-defined function

NRMSD – normalized root-mean-square deviation

NOMENCLATURE

Symbol	Definition	Units
A	Control volume / cell face area	m^2
a_{ij}	Second order orientation tensor	
a_{ijkl}	Fourth order orientation tensor	
B	Suspension consistency index	Pa.s
C_I	Interaction coefficient	
c_p	Specific heat capacity	J/kg.K
D_r	Rotary diffusivity	s^{-1}
$\delta x, \delta y, \delta z$	Fluid volume length, width and height	m
$\Delta x, \Delta y, \Delta z$	Fluid cell length, width and height	
δ_{ij}	Kronecker delta ($\delta_{ij} = 1$ if $i = j$; $\delta_{ij} = 0$ if $i \neq j$)	
E	Total energy	N.m
F_B	Fluid body force	N
f	Scalar measure of orientation	
Γ	Diffusion constant	Pa.s
$\dot{\gamma}_{ij}$	Fluid strain tensor	s^{-1}
$\dot{\gamma}_i$	Fluid strain magnitude	s^{-1}
h	Enthalpy	N.m
i,j,k	Index notation to denote tensor component direction where each index may assume the value of 1,2 and 3 which corresponds to the x, y and z direction respectively	
k	Coefficient of heat conductivity	W/m.K
L	Characteristic length	m
λ	Fiber geometry constant	
m	Total mass of the system	kg
μ	Fluid viscosity	Pa.s

n	Time step number/ Time level	
Ω	cell volume	m^3
ω_{ij}	Fluid vorticity	s^{-1}
Φ , $\Phi_{air,}$ $\Phi_{suspension}$	Fluid volume fraction, the 'air' and 'polymer' subscripts refer to the volume fraction of the specific phase.	
ϕ	Arbitrary continuum variable	
p	Fiber orientation vector	
p_i , p_j , p_k	Component vectors of the vector **p** in index notation	
$\psi(\mathbf{p})$	Fiber orientation probability distribution function	
r_e	Fiber aspect ratio	
ρ	Fluid density	kg/m^3
T	Temperature	K
T_o	Reference temperature	K
τ	Deviatoric fluid stress tensor	N/m^2
U	Fluid velocity	m/s
u,v,w	x,y and z – direction component of velocity	m/s
x,y,z	x, y and z directions (*x* is directed along the bulk direction of the flow)	m
X_i , X_j , X_k	Generalized notation of distance where the index notation is used to specify *x, y* or *z* direction	
Δt	Time step	

CHAPTER 1

INTRODUCTION

1.0 Introduction

In the last fifty years, composites have found applications in diverse areas ranging from military applications and high-end sports equipment to relatively mundane household items such as chair seats. A composite may be described as a combination of two or more materials, where one material acts as a suspending matrix and the others are reinforcing particles embedded within. One such class of composites is short fiber reinforced thermoplastics (SFRTs), where a polymer matrix provides the binding medium, and the short fibers provide the reinforcement. Typical examples of short fibers used in the industry are glass, boron and graphite fibers. The commercial interest surrounding SFRTs stem from the fact that they are lightweight, provide attractive strength-to-weight ratios, and are resistant to chemical attacks and high temperatures [1]. Nevertheless, a significant problem emerges as the mechanical and thermal properties of SFRTs are highly anisotropic, depending heavily upon the direction of fiber alignment [2, 3]. Typically, the material stiffness and strength are greater in the direction of fiber alignment, as compared to across it [2]. Therefore, during processing, it is crucial to ensure that the composite has the bulk of its fibers aligned in the desired direction. Section 1.1 presents the empirical observations of the fiber orientation behaviour during mold-filling, and lays the background work of the model formulation to describe fiber orientation. Previous simulation findings are also discussed. Section 1.2 presents the research problem statement; Section 1.3 lists the research objectives, and Section 1.4 defines the research scope.

1.1 Background

Injection molding is one of the widely used methods for the mass-manufacturing of SFRTs [1]. Polymer pellets are fed into the hopper where the motion of the rotating screw and external heat supplied melt the polymer. The short fibers are added and mixed in a hopper together with the molten polymer melt before being injected at high pressure into the cold mold. A schematic of an injection molding machine is shown in Figure 1.1.
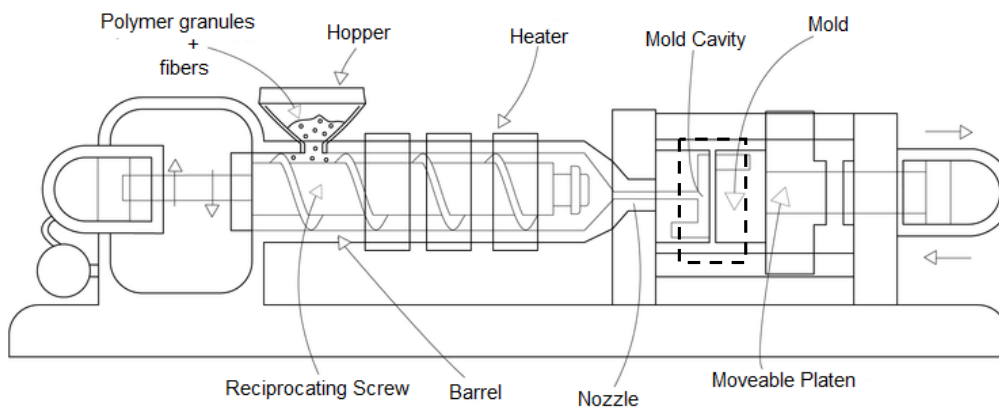
Fig.1.1:A typical injection molding machine (Adapted from [58])

Single or multiple injection points may be used, and the molds may be designed with single or multiple cavities [1]. Once the mold is filled, the polymer – fiber melt is allowed to cool and solidify before the finished composite is removed.

The behavior of short fibers during the mold filling process, (as shown in Figure 1) has been studied in the past and the process of flow induced alignment is well – documented [5]. A characteristic 'layered' structure of orientation takes place, with fibers aligned differently through the thickness of the mold, described later in this section [4]. It was also found that processing conditions, such as polymer – fiber melt temperature, mold temperature, injection speed and mold geometry strongly influence the fiber orientation in the finished composite [4,5].

2

Fiber orientation zones:
1. Skin layer
2. Shell layer
3. Core layer
4. Shell layer
5. Skin layer
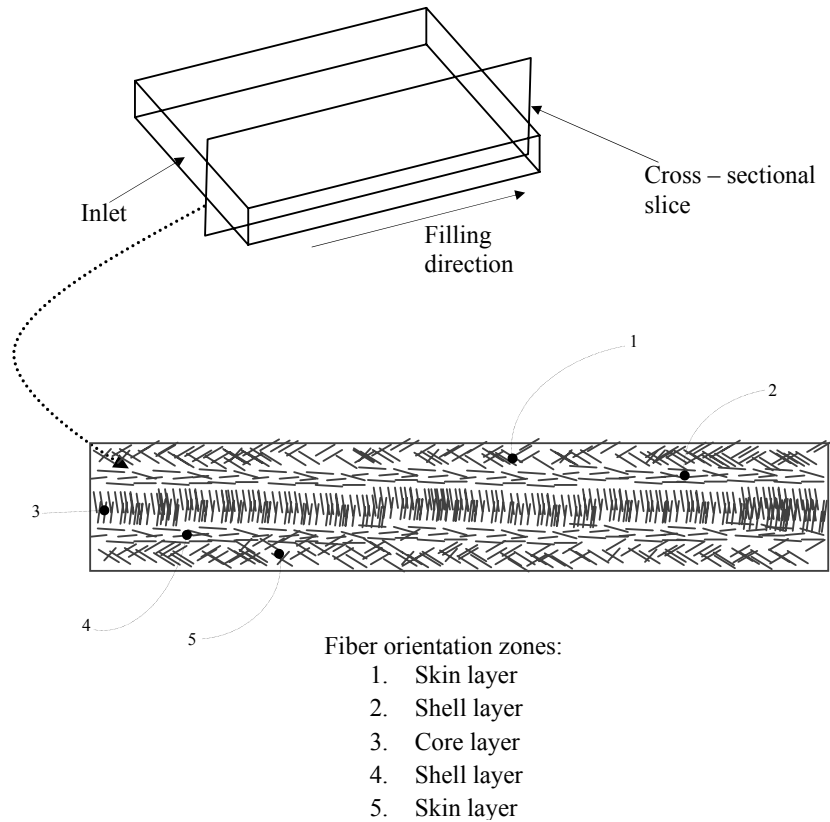
Fig.1.2: A typical rectangular molding sample (short fibers are not drawn to scale and the orientation profile through the mold thickness is exaggerated)

As shown in Figure 1.2, if a cross section of the molding is taken, cut lengthwise in the flow direction and observed under a microscope, a distinct layered structure through its thickness will be observed [5]. Typically, a 5 layer structure is observed consisting of 2 skin layers, 2 shell layers and one core layer [5]. For cavities with large length to height (aspect) ratios, the fibers near the middle of the flow, termed the 'core' layer, are usually oriented transverse to the main flow direction. The fibers immediately adjacent to the mold wall form what is termed the 'skin' layer, and usually have a random orientation. Between these two zones is the 'shell' layer, where the fibers are aligned parallel to the flow direction. These observations are reported in several studies [6, 7, 8, 9] and is generally regarded as the majority view in literature [5].

Although such general observations may be drawn, they are still insufficient to allow for the accurate prediction of fiber orientation in injection moldings which is required for a prediction of the mechanical properties of the finished composite. The modeling of composite stiffness for instance may be formulated on the basis of the orientation of short fibers present within the composite itself [3]. Thus it is vital to accurately model and predict the fiber orientation behavior during the injection molding process, and this has direct consequences for the commercial design and manufacturing of SFRTs.

CHAPTER 2

LITERATURE REVIEW

2.0 Analytical Modeling of Fiber Orientation Evolution

Research directed at modeling the orientation of a single body suspended in a flow began with Jeffery [10] who derived the equations of change governing the rotation of a single ellipsoid in a dilute Newtonian fluid. Jeffery's equations of change were further extended by Bretherton [11] to model the rotation of any single body with fore-aft symmetry, including a cylindrical fiber in a dilute suspension. A dilute suspension is defined as one where the fiber motion is affected by the surrounding fluid only, and fiber – fiber interactions are rare [12]. While the equation of change works well for one fiber, solving it for a group of fibers simultaneously quickly becomes untenable as the rotation of each individual fiber has to be directly accounted for. This lack of feasibility is readily apparent when an industrially relevant manufacturing scenario is considered: a typical industrial grade short fibre composite contains about 10000 short fibres aligned in multiple directions per cubic milimetre [13].

2.1 Numerical Solutions of Fiber Orientation Evolution

If Brownian effects of the suspending fluid are considered, Jeffery's equation has to be transformed to form a Fokker – Planck equation, governing the evolution of the fiber orientation probability [14]. The Fokker – Planck equation is adapted from statistical mechanics where it describes the probability distribution of a particle velocity in a statistical system and can be generalized to describe other particle properties (such as orientation) as well. The Fokker-Planck equation applied in this context is a transient convective-diffusive equation that describes the change in the

probability distribution of fiber orientation. The direct solution of the Fokker – Planck equation has faced difficulties in the past due to the mathematical complexity and computing resources required in order to solve the orientation of a large number of fibers [1].

However, in recent years, there has been an increase in interest in the Fokker-Planck approach due to the increase in computing power available as well as the fact that this approach precludes the necessity of closure models, a drawback of the orientation tensor approach described later. Nevertheless, application of the Fokker-Planck equation to describe fiber orientation evolution has been limited to flow regimes involving simple shear or recirculating shear flows, isothermal Newtonian fluid behaviour and involving simple two-dimensional geometries [15, 16 and 17]. These limitations restrict the applicability of the method to real world mold-filling problems involving arbitrary three-dimensional mold geometries and Non-Newtonian non-isothermal flows.

In view of this, tensorial approaches to modeling the fiber orientation were considered instead, beginning with Hinch and Leal [18, 19] and culminating with a full description of the fiber orientation evolution equation in tensor form by Advani and Tucker [20]. The orientation evolution equation is much less cumbersome, easier to implement and considerably less computationally expensive, although the accuracy is somewhat compromised [21]. However, in the case of industrial scale composite manufacturing, the aggregate behaviour of the fibers is a sufficient description of the orientation state [13]. This has been the approach of choice for many researchers in the last two decades [13, 21, 22, 23, 24, and 25].

The use of the fiber orientation evolution equation in tensorial form does give rise to a particular problem, namely the appearance of fourth order tensor components [20]. In order to close the set of equations, the fourth order tensors have to be approximated in terms of the second order ones [20]. A variety of closure models have been introduced by researchers in the recent years. Hand [26] introduced a linear closure, so termed due to the fact that it was formed through a linear combination of the second order tensor terms. The model was derived with consideration of symmetry assumptions about the second order orientation tensor,

6

and is exact for flow cases where the orientation is random in space [29]. Hinch and Leal [27] derived limiting forms of the Fokker – Planck equation for cases where Brownian motion dominated the flow, and where it was of insignificant effect. Interpolating between the two equations, an expression for the fourth order orientation tensor was obtained. In flow circumstances involving significant fiber – fiber interaction, the Brownian motion effect is limited thus allowing for a simplified closure termed the quadratic closure [27]. This closure is exact for cases where the orientation is aligned along one particular direction [29]. Advani and Tucker combined both the linear and quadratic closure model, using an absolute measure of orientation to interpolate between the two closures [20]. This model was termed the hybrid closure. Further development of the closure models involved a change in philosophy, whereby the eigenvalues of the orientation tensor are used to generate closure model forms [31]. The coefficients of these models are then computed by data – fitting to the solutions of the Fokker- Planck equation governing the fiber orientation probability distribution function. This is performed for several representative flow cases such as simple shear and stretching flow in order to obtain suitable coefficients [31]. Similar to this approach, the natural closure is conceived by first analytically solving the Fokker – Planck orientation equation for an idealized fiber, neglecting the fiber – fiber interactions [32]. These will yield canonical distributions of the fiber orientation which are then used to construct a closure model. However, while a closure model may be analytically derived for a two – dimensional orientation case, the three – dimensional orientation still requires 'tuning' of coefficients in a similar procedure to the orthotropic closures.

An additional consideration for the accurate modeling of fiber orientation behavior was the modeling of the fiber – fiber interactions and the effect of the fiber orientation upon the rheology of the suspending fluid. Lipscomb et al. [33] demonstrated that the presence of fibers in a polymer flow affected its rheology, in particular increasing its elongational viscosity or resistance to stretching. Dinh and Armstrong [34] modeled and experimentally fitted an equation model to relate the contribution of fiber orientation to the fluid stress based upon the local orientation tensor and the fiber volume fraction. Tucker [35] studied the effect of the flow field and fiber interaction in slender two-dimensional gaps, and evaluated the degree to

which fiber orientation affected the rheology of the suspending fluid. Utilizing scaling analysis, Tucker analyzed the degree to which the orientation effect could be neglected, allowing for the fiber orientation evolution equation to be effectively 'decoupled' from the fluid momentum equations. An important study of fiber – fiber interactions was conducted by Folgar and Tucker [36], where the randomizing effect of these interactions was modeled as a function of an empirical constant and the strain rate magnitude.

Once a solid framework for implementing the governing equations of fiber orientation was in place, mold – filling simulations could be performed, where parameters relevant to industrial – scale manufacture of SFRTs could be introduced. Factoring in parameters such as industrial scale injection pressures, processing temperatures, fiber volume fractions and melt viscosity behavior allow for a realistic description of the mold – filling process relevant to the industry. Bay [9, 21] simulated the non-isothermal filling of a film – gated strip mold and performed a decoupled analysis of the fiber orientation development in the mold. Chung and Kwon [22] simulated non – isothermal mold – filling flow and solved a coupled three – dimensional fiber orientation evolution equation for several three – dimensional cavities. They estimated the clamping force necessary for the mold in relation to the degree of fiber – fiber interaction. Hung and Shen [37] performed a two – dimensional analysis of the filling and subsequent fiber orientation of a rectangular mold, utilizing Jeffery's equation to model the fiber rotation. They determined that fiber motion and orientation change occurred fastest in the suspension – air interface region.

A common feature of those works was the use of the Hele – Shaw method to reduce the mathematical treatment of the mold – filling flow from three dimensions to two [38]. The mathematical simplification introduced by the Hele – Shaw method however, is unable to numerically capture the fountain flow effect. Fountain flow occurs at the suspension – air interface, where the suspension velocity reduces significantly as it approaches the interface. Due to the constraint of fluid continuity, the suspension flow is directed outward towards the wall. Capturing this feature is essential for the accurate description of the flow behaviour at the interface.

Verweyst [13] solved the coupled fiber orientation evolution equation with the full three – dimensional set of fluid equations for the filling of a radial disk and noted that there was considerable difference between the results obtained by this method and those with the Hele – Shaw approximation. Verweyst further noted that the coupling between the fiber orientation and the suspension momentum was significant in the core regions of the flow, and that this was almost negligible in the shell regions. It was further noted that the decoupled assumption is valid for slender cavities [30]. This analysis is important as it studies the fiber orientation behavior in high and low shear regions of fluid and help explain the layered structure described earlier, as parallel flow in a mold cavity exhibits both high and low shear regions [5].

Chung and Kwon [25] simulated the filling of a film – gated strip and a radial disk, and solving for the fiber orientation. They tested two approaches: the Hele-Shaw method and a full three – dimensional simulation of the flow. Their findings agree with those of Verweyst: the fountain flow effect produces a significant difference in the fiber orientation development of the flow. In addition, they also found that coupling the fiber orientation to the suspension momentum produced blunter velocity profiles as compared to the decoupled case; this is demonstrated in Figure 2.1. Further, they also noted that the effects of coupling were significant in the core and transition (from core to shell) layers, and that this effect diminished rapidly in the shell layer.
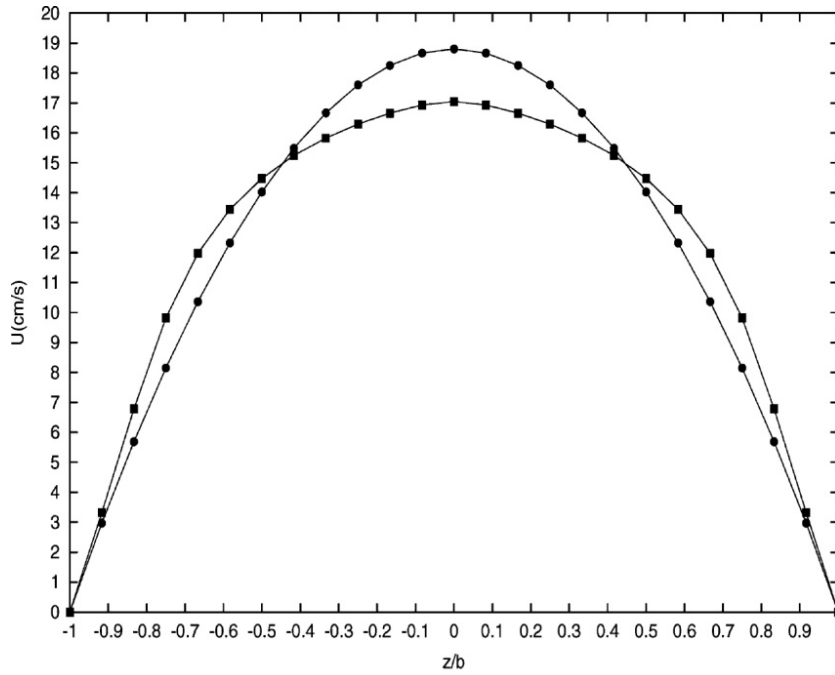
Fig.2.1: Fiber orientation coupling effects on the radial flow velocity of a center –
gated disk. The circles represent a decoupled analysis and the squares
represent the coupled one. (Adapted from Chung and Kwon [25])

2.2 Problem Statement

In recent years, short-fiber reinforced composites have become materials of choice in many areas of mass and specialized manufacturing. As the properties of a finished composite depend highly upon the orientation of short fibers during the processing phase, there is a necessity to effectively model the entire mold filling process. The orientation tensor description of fiber orientation has found favour due to the ease of numerical implementation and its relative computational cheapness as compared to the Fokker-Planck method. In recent years, it has also been featured in commercial numerical codes for solving mold-filling problems involving SFRTs, such as Moldex3d and Moldflow. However, these commercial softwares are 'black-box' applications that do not allow for the free modification of their internal workings. Thus, important aspects of the simulation of fiber orientation evolution

such as the model equations used and the solution algorithms which may require modification with passing time are inaccessible. Therefore, there is a strong motivation for the development of in-house mold-filling numerical software that solves for the fiber orientation evolution as well. This research project represents a step in that direction; a numerical code that solves the fiber orientation evolution is 'piggybacked' on a mold-filling flow simulation performed with the commercial CFD code, FLUENT 6.3.

2.3 Research Objectives

This research's objectives are as follows:

1. Simulate the filling of an initially empty mold by a suspension consisting of a mixture of molten polymer and short fibers.

2. Develop a code to numerically solve the discretized fiber orientation evolution equation, with coefficients derived from the flow field results extracted from the three – dimensional mold – filling flow simulation.

3. Implement three closure models: linear, quadratic and hybrid closures, and compare the numerically computed orientation against an experimental data set obtained from literature. The performance of each closure model is assessed.

2.4 Scope of Study

The scope of this study may be divided into two phases. The first phase involves the numerical simulation of the filling of an initially empty mold with the aid of the commercial CFD code, FLUENT 6.3. The mold is a rectangular, film-gated strip [29]. The mold-filling flow is treated as an incompressible three-dimensional, laminar, unsteady, non-isothermal flow, and the fluid is treated as a polymeric Non-Newtonian fluid. Velocity, pressure, temperature and volume fraction parameters are supplied at the mold inlet boundary and outlet. A slip condition and temperature parameter is applied at the wall. The effects of the slip condition type (dynamic vs.

traditional no-slip) are studied and a grid independence test is also carried out. Verification of the mold-filling simulation setup is performed by comparison with a solved two-dimensional problem from literature [39]. The second phase of this study is the simulation of the two-dimensional fiber orientation on a segment of the flow domain extracted from the FLUENT results. The simulation of fiber orientation is pursued via decoupled analysis and three closure models: linear [26], quadratic [27] and hybrid [20] are implemented, and their performance is assessed against experimental data from literature [29]. The parameters supplied for the simulation of fiber orientation are the inlet orientation state and the initial orientation field. A numerical code was written in Matlab for this purpose.

2.5 Summary

SFRTs find application in diverse areas. As the properties of the finished composite depend strongly on the fiber orientation, there is strong research and commercial interest to ensure that that the fiber orientation development during the processing phase is well modeled. This research is directed towards simulating the fiber orientation during the filling of an initially empty mold. A numerical code is developed to solve the fiber orientation evolution equation, and three closure models are implemented separately. The numerical results are compared against experimental data in order to assess the predictive capability of each closure model.

CHAPTER 3

GOVERNING EQUATIONS

3.0 Introduction

In the analysis of mold-filling flows, the numerical solution of the Navier-Stokes equations describes the behavior of the fluid flow. Physical conservation laws which have to be satisfied are mass, momentum and energy conservation. Further, additional equations that model the non-Newtonian viscosity have to be included as well. These are described in Sections 3.1 through Section 3.4. For the fiber orientation modeling, the governing equation solved is the fiber orientation evolution equation. These equations may be formulated about an imaginary fluid volume that possesses the extensive properties of mass, momentum and energy. The fiber orientation tensor may be treated as an extensive scalar property, as it derives from ensemble averages of fibers about a fluid volume. This is described in Section 3.5.

3.1 Mass Conservation

The mass conservation laws states that the mass of the system is conserved, i.e. there is no creation or destruction of mass during the mold-filling flow. Thus, the total rate of change of mass of the system is zero as seen in Equation 1:

$$\frac{dm}{dt} = 0$$

(1)

Conceptually, the mass balance of a fixed fluid volume may be expressed as follows: The rate of mass increase in the fluid volume is equal to the net rate of mass flow through the fluid volume.

This concept can be written mathematically as:

$$\frac{\partial}{\partial t}\left(\rho \delta x \delta y \delta z\right) + \nabla \cdot \left(\rho U \delta x \delta y \delta z\right) = 0$$

(2)

If the working fluid is regarded as incompressible and steady, then the density is constant and the set of equations reduces to:

$$\frac{\partial u}{\partial x} + \frac{\partial v}{\partial y} + \frac{\partial w}{\partial z} = 0$$

(3)

This is known as the continuity equation for an incompressible, steady working fluid.

3.2 Momentum Conservation

The momentum conservation principle applied to the fluid volume implies that the rate of momentum change of the fluid across the volume is equal to the sum of the external forces applied to the volume itself. Mathematically, this is described as follows:

(4)

Where m is the mass of the fluid volume, U is the fluid velocity and F represents the forces applied. The left hand side of Equation 4 may be expanded by means of the Burger's expansion, and the external forces applied may also be expanded to include surface and body forces. Surface forces are those that act upon the surface of the fluid volume, and are thus surface orientation dependant (i.e. pressure and viscous forces), whilst the body forces are those that act independently of orientation

14

(i.e. gravitational, centrifugal and magnetic forces). Mathematically, this is described by the following equation:

$$\rho \frac{\partial U}{\partial t} + \rho U \cdot \nabla U = -\nabla P + \nabla \cdot \tau + F_B$$

(5)

The deviatoric stress tensor τ is defined as follows:

$$\tau = 2\mu \dot{\gamma}_{ij}$$

(6)

and the fluid strain tensor, $\dot{\gamma}_{ij}$ is derived as:

(7)

where the tensor notation $i,j = 1,2,3$

The polymer-fiber (suspension) mixture displays Non-Newtonian behaviour and thus its viscosity changes with respect to the temperature and local strain rate. In addition, due to the fact that a two-phase filling process is encountered here, the phase present in a fluid volume may be the suspension or air, or a combination of both. The air phase is assumed to have a constant Newtonian viscosity. The suspension viscosity however is modeled with a Power Law model as follows:

$$\mu = B \dot{\gamma}^{n-1} e^{T_o/T}$$

(8)

where n refers to the fluid index and the strain rate magnitude γ_{ij} is defined as:

(9)

For flows which are near-creeping (Re < 2), such as those observed in mold-filling, it has been demonstrated that the body force term, consisting of the

15

gravitational and surface tension terms is negligible [23, 40], thus dropping F_B from Equation 5.

3.3 Energy Conservation

The principle of energy conservation states that the rate of change of energy of the fluid volume must equal the net amount of energy entering and leaving the volume. The energy of the fluid volume is the sum of the fluid internal energy and kinetic energy. The energy flow into the fluid volume comes primarily from heat conduction and viscous dissipation. In the event that the change in kinetic energy of the fluid is negligible, constant thermal properties and the pressure work done on the volume is also negligibly small, then the energy equation may be written as:

$$\rho c_p \left(\frac{\partial T}{\partial t} + U \cdot \nabla T \right) = \nabla \cdot k \nabla T + \mu \dot{\gamma}^2 \tag{10}$$

3.4 Fluid Volume Fraction Conservation

The mold-filling flow is a two-phase filling process, and the gradual filling of the mold is modeled by the volume fraction equation. The scalar Φ represents the volume fraction of the phase occupying a fluid volume. The volume fraction $\Phi = 1$ indicates that the volume is occupied by the polymer-fiber mixture while $\Phi = 0$ indicates that the volume is occupied by air and values in between indicate that the volume is occupied by a combination of both fluids. The volume fraction equation is written as follows:

$$\rho \left(\frac{\partial \Phi}{\partial t} + U \cdot \nabla \Phi \right) = 0 \tag{11}$$

The volume fraction equation serves two purposes: first, it allows for the tracking of the fluid interface and second, the material properties at each control volume are evaluated as a volume fraction average of the existing individual phases.

16

3.5 Fiber Orientation

The orientation of fibers in suspension is modeled based upon two major assumptions. First, the fibers are assumed to be rigid cylinders, uniform in length and diameter [11, 20]. Second, the concentration of fibers throughout the suspension is uniform. The orientation of a single fiber may be described by a single vector **p** aligned along its principle axis as shown in Figure 3.1.
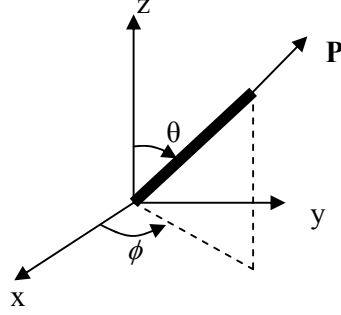
Fig.3.1: The orientation of a single fiber

The *x*, *y*, and *z* components of **p** are represented as follows:

$$p_x = p_1 = \sin\theta\cos\phi$$
$$p_y = p_2 = \sin\theta\sin\phi$$
$$p_z = p_3 = \cos\theta \tag{12}$$

The change in indices (from alphabets to numbers) is used to facilitate the use of tensor notations. The second order and fourth order tensors are taken as spatial ensemble averages of the orientation vectors of individual fibers, as follows:

$$a_{ij} = \left\langle p_i p_j \right\rangle = \oint p_i p_j \psi(\mathbf{p}) \, d\mathbf{p} \tag{13}$$

$$a_{ijkl} = \left\langle p_i p_j p_k p_l \right\rangle = \oint p_i p_j p_k p_l \psi(\mathbf{p}) \, d\mathbf{p} \tag{14}$$

The second and fourth order tensors are a suitably compact and accurate description of the fiber orientation state [29].

Following this, several tensor properties may be invoked in order to provide simplifications to the system of tensors. A subscript notation is used here to describe

17

a tensor, a_{ij}, where i,j and k represent the tensor indices (1,2,3). The components '11', '22' and '33' represent the x, y and z directions respectively. The out of plane or mixed components '12', '13' and '23' represent projections of the tensor onto the x-y, x-z and y-z plane respectively. The orientation tensor for a single fiber is shown relative to the Cartesian axes in Figure 3.2.
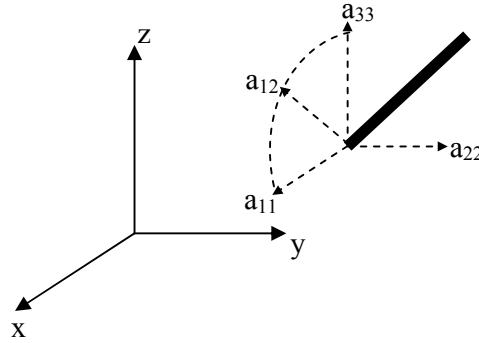
Fig.3.2: The orientation tensor for a single fiber relative to the Cartesian axes

The second order orientation tensor consists of five independent components a_{11}, a_{22}, a_{12}, a_{13} and a_{23}, and forms a 9-element matrix where the components a_{11}, a_{22} and a_{33} represent the principal directions of orientation, and the magnitude of each term represents the strength of the orientation in the direction. The non-diagonal terms represent the degree to which the orientation frame of the fiber is rotated out of the principal axis system. If the fiber is oriented within the principal axis system, the diagonal terms reduce to zero.

3.5.1 Fiber Orientation Evolution Equation

The fiber orientation evolution equation models the change of the fiber orientation as a function of the local fluid flow field, fiber orientation and fiber-fiber interaction effects. The evolution equation used in this research project is the Advani-Tucker orientation tensor equation [20], which is essentially a re-writing of the Folgar-Tucker evolution equation [36] using orientation tensors to characterize the fiber orientation. Once the normalization and the symmetry condition are considered, there are five independent components to the a_{ij} tensor: a_{11}, a_{22}, a_{12}, a_{13} and a_{23}. Thus,

18

there are five independent evolution equations to describe the evolution of each tensor component separately.

$$\frac{\partial a_{ij}}{\partial t} + U_k \frac{\partial a_{ij}}{\partial X_k} = -\frac{1}{2}\left(\omega_{ik}\, a_{kj} - a_{ik}\, \omega_{kj}\right) + \frac{1}{2}\lambda\left(\dot{\gamma}_{ik}\, a_{kj} + a_{ik}\, \dot{\gamma}_{kj} - 2\dot{\gamma}_{kl}\, a_{ijkl}\right)$$
$$+ 2D_r\left[\delta_{ij} - \alpha\, a_{ij}\right] \tag{15}$$

ω_{ij} is the fluid vorticity defined as:

$$\omega_{ij} = \frac{1}{2}\left[\frac{\partial U_j}{\partial X_i} - \frac{\partial U_i}{\partial X_j}\right] \tag{16}$$

The parameter α equals 3 for a three dimensional version of the equation and 2 for planar orientation, and λ is a constant that depends on the geometry of the fiber, being defined as $\lambda = (r_e^2 - 1)/(r_e^2 + 1)$ with r_e being fiber aspect ratio.

The rotary diffusivity, D_r models the Brownian-like motion of the fibers arising from fiber-fiber interactions within the suspension. It should be noted that although a basic assumption introduced at the beginning of the analysis is that the fibers are large enough not to be affected by the Brownian motion of the fluid molecules, the effect of fiber interactions on the fibers themselves are modeled as a Brownian motion. A simple inspection of the right hand side of the fiber orientation evolution equation illuminates the factors affecting orientation change. The first two terms represent the effect of the fluid vorticity and strain rate acting upon the current fiber orientation. The third term represents the effect of fiber-fiber interactions on the orientation change.

The effect arising from the D_r term is two-fold [41]: Firstly, the diffusivity acts to randomize the fiber motion - as the value of D_r increases, the fiber motion becomes more random. Secondly, it makes the fiber orientation in simple shear flows asymmetrical. In the Folgar-Tucker model, the diffusivity term was modeled to be a function of the magnitude of strain rate tensor, and an interaction coefficient [36].

This is described as follows:

$$D_r = C_I \dot{\gamma} \tag{17}$$

where C_I is the interaction coefficient. The following expression was derived by Bay for the interaction coefficient in concentrated suspensions [29]:

$$C_I = 0.0184 \, e^{-0.7148 \, \phi \, r_e} \tag{18}$$

The fourth order tensor that appears in Equation 15 has to be approximated by means of a closure approximation. This is explained in the next section.

3.5.2 Closure Approximations

Closure approximations are introduced in order to close the orientation tensor evolution equation. In essence, it represents the higher order tensor as a function of the lower order ones. For the case of the second order tensor, a closure approximation of the fourth order is required:

$$a_{ijkl} = f(a_{ij}) \tag{19}$$

The closure models which are to be assessed are described in this section. These models are built on purely analytical analysis where combinations of the second order tensor are used to construct the fourth order one. Thus, these are as stand-alone models, and do not need to be 'tuned' in any sort of way with respect to solutions of the Fokker-Planck version of the orientation probability distribution function [14]. By contrast, more modern models such as the orthotropic class of closures require this [31, 32].

i. Linear Closure Model

The linear closure model constructs the fourth order tensor from a combination of the second order orientation tensor and the Kronecker delta [26]. This model is linear in the sense that only first order terms appear.

$$
\begin{aligned}
a_{ijkl} &= -\frac{1}{35}\left(\delta_{ij}\delta_{kl} + \delta_{ik}\delta_{jl} + \delta_{il}\delta_{jk}\right) \\
&+ \frac{1}{7}\left(\begin{array}{l} a_{ij}\delta_{kl} + a_{ik}\delta_{jl} + a_{il}\delta_{jk} \\ + a_{kl}\delta_{ij} + a_{jl}\delta_{ik} + a_{jk}\delta_{il}\end{array}\right)
\end{aligned}
$$

(20)

ii. Quadratic Closure Model

The quadratic closure model makes the simple assumption that the fourth order tensor is a product of two second order orientation tensor terms, with the appropriate choice of indices [27].

$$
a_{ijkl} = a_{ij}a_{kl}
$$

(21)

iii. Hybrid Closure Model

The hybrid closure model is actually a result of the combination of two earlier models: the linear closure model and the quadratic closure model [28].

$$
a_{ijkl} = (1-f)a_{ijkl}^{linear} + f\, a_{ijkl}^{quadratic}
$$

(22)

where $f = 1 - 27\det\left[a_{ij}\right]$ is the scalar measure of the orientation. It should also be noted that the hybrid closure is a popular model used in the simulation of real manufacturing processes due to its stability [23].

21

3.6 Summary

The mathematical equations governing the mold-filling flow are built on the basis of conservation of mass, momentum and energy principles and are listed as follows:

1. Continuity equation

2. Momentum equation

3. Energy equation

4. Fluid volume fraction equation

The fiber orientation is governed by an orientation evolution equation, and is closed by a closure model. The three closure models implemented in this research are as follows:

Linear closure

Quadratic closure

Hybrid closure

As these equations are not amenable to direct analytical solution, they are implemented numerically. This is described in the Chapter 3 of the thesis.

CHAPTER 4

THEORY AND IMPLEMENTATION

4.0 Introduction

The equations described in Chapter 3 model the physical process of mold – filling and the consequent fiber orientation. These equations have to cohere with the actual physical processes which occur during mold – filling. Further, these equations are numerically implemented and solved iteratively. Section 4.1 presents a physical overview of the injection molding process. Section 4.2 describes the numerical implementation of the equations governing mold-filling flow. Section 4.3 describes the numerical implementation of the fiber orientation evolution equation.

4.1 A Physical Description of the Injection Molding Process

A brief description of the physical process of injection molding is necessary in order to have a good idea of what exactly is being modeled. Figure 4.1 shows a simple mold geometry that accords with the rectangular film gated strip from Bay's work [29]. Bay performed mold – filling experiments to study fiber orientation during the filling process, and the experimental data Bay obtained is used in this work for comparison with our numerical simulation results. This is expanded in greater detail in Chapter 4.2.
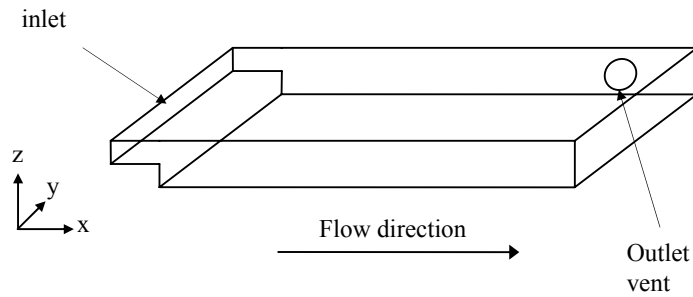
Fig.4.1:Schematic of a film-gated strip

The physical process of mold filling, from an injection molding standpoint may be outlined in three broad stages as follows:

Prefilling: (Initial condition)

- The mold is initially empty (air-filled) at an initial ambient temperature

Filling:

- Hot polymer melt is injected into the mold via a film gate.

- The polymer melt is subject to cooling as the mold walls are kept at a constant temperature, much lower than the solidifying temperature of the melt.

- As the mold fills, the polymer melt displaces the air, and the air escapes through a vent at the far end of the mold

Post- filling:

- The injection filling stops once the mold is completely filled

- The filled mold is allowed to cool and then the finished composite is removed.

As may be observed, the filling phase is of greatest concern in this research project, and it is to this phase of injection molding that the fiber orientation evolution is especially pertinent. The physical mold-filling flow consists of a polymer resin with suspended short fibers within, which is injected at high pressure and high temperature into an empty mold. This suspension is modeled as a three-dimensional laminar, incompressible, non-isothermal, non-Newtonian flow. Several key assumptions of the flow have to be addressed here:

24

- The mold-filling flow is treated as a filling problem, whereby the hot polymer and fiber mixture is injected into an empty mold, and gradually fills it whilst displacing air from the mold.
- Incompressibility of the polymer-fiber mixture is assumed, and solidification effects due to cooling of the mixture are neglected.
- The viscosity of the polymer-fiber suspension is regarded as non-Newtonian, and varies with the local strain rate and temperature of the flow.
- The mold-filling phase is decoupled from the fiber orientation, thus the flow equations are solved separately from the fiber orientation. This disregards the effects the fiber orientation may have on fluid momentum.

The simulation of the fiber orientation evolution was performed via a two – stage process; first, a simulation of the mold-filling flow was performed with the aid of the commercial Computational Fluid Dynamics (CFD) software, FLUENT 6.3. Second, the resultant flow field was used to perform numerical computation of the fiber orientation evolution equation, implemented in Matlab. A two – dimensional plane was extracted from FLUENT, and the two – dimensional fiber orientation evolution equation was solved on this plane utilizing the flow field data obtained for a fully filled mold.

4.2 Numerical Implementation of the Governing Equations of the Mold – Filling Process

The governing equations describing the mold-filling flow were numerically solved using FLUENT 6.3 which utilizes the finite volume (FV) method to solve a series of descretised flow equations on a discrete spatial and temporal numerical grid. This section presents a brief description of the finite volume method where this process is elaborated by the discretization of a one – dimensional steady diffusion equation. The temporal discretization of transient terms is also addressed. The numerical treatment of each of the significant flow equations: momentum, energy and volume fraction equations are addressed individually. The implementation of the fiber orientation evolution equation is also addressed.

4.2.1 Finite Volume Method

The FV method is popular in fluid dynamics simulations due to the use of the conservation form of the flow equations in the discretization of these equations [42]. In this section, simplified equations are used to describe the methods used in the numerical treatment of the flow equations solved by FLUENT. The discretization of the flow equations is performed on a control volume (CV). A CV may be a one, two or three dimensional structure. For simplicity, a rectangle is used here as the CV for the two dimensional case and a cube for the three dimensional one. It should be noted that the discretization of the flow equations about a control volume may be performed for any arbitrary shape. A rectangle or cube simplifies the discretization process as they are easily referenced to the Cartesian axes. Figures 4.2 and 4.3 present a visualization of the numerical grid for both a two – dimensional and three – dimensional case.
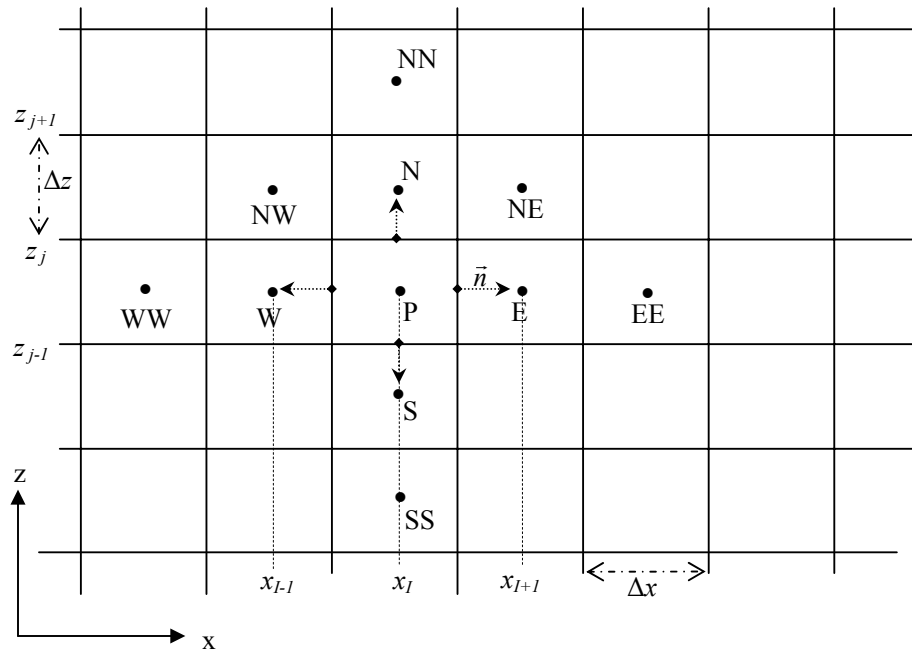
Fig.4.2: Typical rectangular two-dimensional finite volume grid [42] (the N – S direction coincides with the z axis)
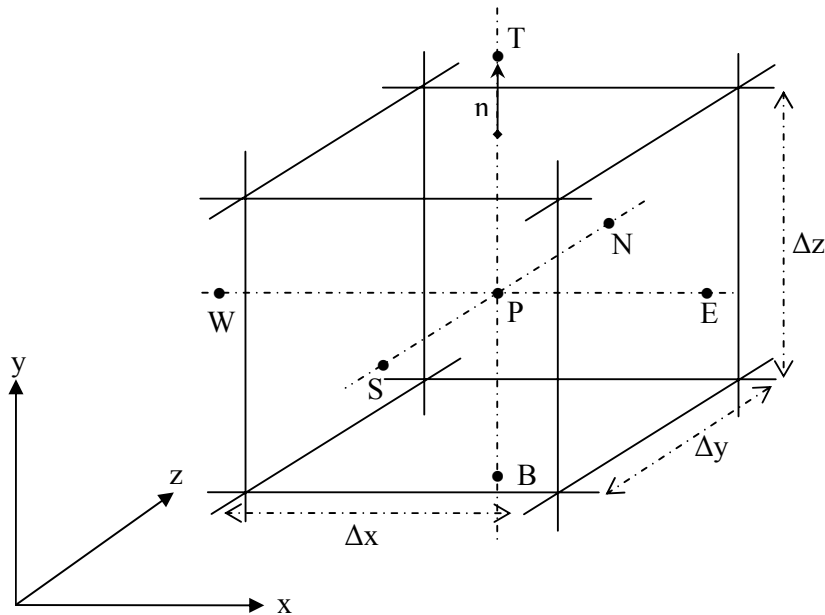
Fig.4.3: Typical rectilinear control volume (CV) in a three – dimensional grid [42]
(the N – S direction coincides with the y axis and the T – B direction coincides with
the z axis)

The notation for both the two and three – dimensional grids here follow the magnetic compass convention for simplicity of notation, where the symbols mean; North (N), South (S), East (E), West (W), North-East (NE), North-West (NW), South-East (SE), South-West (SW), North-North (NN), South-South (SS), East-East (EE), West-West (WW), Top (T) and Bottom (B).

The node (P) here refers to the reference or principal node. Other quantities of interest are Δx , Δy and Δz (grid spacing in the *x*, *y* and *z* direction). and *n*, the normal vector to the line or area bounding the cell. The principal node (P) is bounded by four lines (in the 2D grid) and six planes (in the 3D case) the area or volume bounded by these lines or planes is referred to as the control volume. It may also be referred to as a 'cell'. The principal node is located in the center of the cell and *n* is the normal vector projected from the line or area bounding the cell [42]. The flow equations are then descretised in a manner where the change in the scalar quantity of

a principal node is related to the quantities at its neighbouring nodes through scalar fluxes through the boundaries of the cell.

To describe the discretization process, a simple 1-dimensional steady convective – diffusive equation is considered:

$$\frac{\partial(\rho\phi u)}{\partial x} = \frac{\partial}{\partial x}\left(\Gamma\frac{\partial\phi}{\partial x}\right) \qquad (23)$$

where ϕ is any arbitrary scalar continuum variable and Γ is the diffusion constant.

A central differencing scheme is employed where the gradient at node P is approximated by values one node to the left (West) and one node to the right (East) of node P as shown in Figure 4.4.

It may be descretised for a one – dimensional grid as follows:
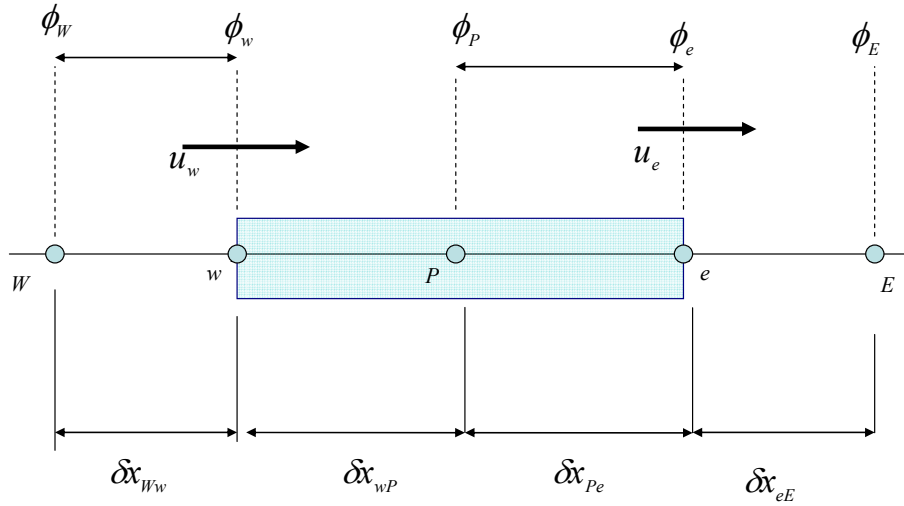
Fig.4.4: A representative one – dimensional finite volume grid

$$(\rho\phi u)_e A_e - (\rho\phi u)_w A_w = \frac{\Gamma_e}{\delta x_E}(\phi_E - \phi_P)A_e - \frac{\Gamma_w}{\delta x_W}(\phi_P - \phi_W)A_w$$

$$\delta x_E = \delta x_{Pe} + \delta x_{eE}$$

$$\delta x_W = \delta x_{wP} + \delta x_{Ww}$$

$$(24)$$

For a grid with equal spacing as a special case, the face areas are the same, thus they cancel out, simplifying the equation to:

$$F_e\phi_e - F_w\phi_w = D_e(\phi_E - \phi_P) - D_w(\phi_P - \phi_W)$$

$$\text{where} \quad F_e = (\rho\phi u)_e, \quad F_w = (\rho\phi u)_w, \quad D_e = \frac{\Gamma_e}{\delta x_E} \quad \text{and} \quad D_w = \frac{\Gamma_w}{\delta x_W}$$

$$(25)$$

The quantities ρ, ϕ and u have to be approximated on the cell faces, and are assumed to be known or guessed. Various schemes exist for the treatment of the discretized variable, if the first order upwind scheme is employed for instance, the flow direction is from west to east so we set $\phi_w = \phi_W$ and $\phi_e = \phi_P$. The equation then becomes:

30

$$[(D_w + F_w) + D_e + (F_e - F_w)]\phi_P = (D_w + F_w)\phi_W + D_e\phi_E \qquad (26)$$

<div align="right">Or,</div>

$$a_P\phi_P = a_W\phi_W + a_E\phi_E$$

where a_P denotes the coefficient of the principal node and a_W and a_E denote those of the nodes to the West and East of the principal node respectively. The 'upwind' term refers to the node position relative to the flow direction. In this case, as the flow direction is from west to east, thus the cell on the west of the cell P is 'upwind' relative to cell P. This may be generalized to a series of nodes terminating on both ends with known boundary values of ϕ, and we then have a system of linear equations such that:

$$a_P\phi_P = \sum_{neigh} a_{neigh}\,\phi_{neigh} + B$$

<div align="right">(27)</div>

where '*neigh*' denotes the neighbouring nodes and B is a scalar constant. The system of equations may then be solved iteratively.

The flow equations encountered in this work involve transient terms as the mold – filling flow and fiber orientation evolution are treated as unsteady processes. Thus, temporal discretization is required as well in order to 'march' the solution forward in time. The FLUENT solver used for the two and three – dimensional simulations in this research is first order implicit which can be described by considering the temporal discretization of Equation (28).

$$\frac{\partial(\rho\phi)}{\partial t} + \frac{\partial(\rho\phi u)}{\partial x} = \frac{\partial}{\partial x}\left(\Gamma\frac{\partial\phi}{\partial x}\right) \qquad (28)$$

where a transient term has been added on the left – hand side of Equation (23). The spatial terms may be discretized as described previously. The transient term is approximated by a first order backward difference (implicit) such that:

$$\frac{\partial(\rho\phi)}{\partial t} \approx \frac{(\rho\phi)_P^{n+1} - (\rho\phi)_P^n}{\Delta t} \tag{29}$$

where the spatial terms are evaluated at time step '$n+1$'. For a time step size, Δt the system of linear equations that arises from the discretization of Equation 28 is:

$$a_P \phi_P^{n+1} = a_P \phi_P^n + \Delta t \left[\sum_{neigh} a_{neigh} \ \phi_{neigh}^{n+1} + B \right] \tag{30}$$

The choice of the implicit scheme is motivated by the fact that it is stable for a large range of time steps [52]. In a similar manner, the flow equations may be discretized on a three-dimensional grid which results in a system of equations identical in form to Equation 30.

4.2.2 Solver

A segregated solver was applied whereby the numerical iteration of the flow equations; continuity, momentum, energy, etc. proceeds sequentially as depicted in Figure 4.5.

```
                        ┌─────────┐
                        │  Start  │
                        └─────────┘
                             │
                             ▼
                ┌────────────────────────┐
      ┌────────►│   Update properties    │
      │         └────────────────────────┘
      │                    │          Guess x, y and z velocities:
      │                    ▼                  u*,v*,w*
      │         ┌────────────────────────┐
      │         │  Solve the momentum    │
      │         │  equation: x, y and z  │
      │         │      velocities        │
      │         └────────────────────────┘
      │                    │
      │                    ▼
      │         ┌────────────────────────┐
      │         │  Solve the pressure –  │
      │         │  correction equation   │
      │         └────────────────────────┘
  ┌───────────────────────────┐
  │ Set computed x, y and z   │
  │    velocities: u, v and w │
  │ to be the guess velocities│
  │  for the following        │
  │  iteration: u*,v*,w*      │
  └───────────────────────────┘
      │                    │
      │                    ▼
      │         ┌────────────────────────┐
      │         │  Correct and update    │
      │         │  pressure and velocity │
      │         │  values over the       │
      │         │  entire flow field     │
      │         └────────────────────────┘
      │                    │
      │                    ▼
      │         ┌────────────────────────┐
      │         │  Solve energy and      │
      │         │  volume fraction       │
      │         │  equation              │
      │         └────────────────────────┘
      │                    │
      │  No                ▼             Yes   ┌──────┐
      └────────┤ Convergence Check ├──────────►│ Stop │
                                               └──────┘
```

Fig.4.5 : solution algorithm of the segregated pressure-based solver in FLUENT

FLUENT solves a general conservation equation defined in Equation 32 that serves as a template for the physically meaningful flow equations. Due to the two-phase nature of the flow, a control volume or cell may be filled with either one or both fluids at the same time. Thus, the fluid properties in a particular cell may be considered to be representative of the composition of the two different fluid species present and are taken as the volume averages of the species properties as follows:

$$\phi_{CV} = \phi_{polymer} \times \Phi_{polymer} + \phi_{air} \times \Phi_{air}$$

$$\Phi_{polymer} = \frac{volume\ occupied\ by\ polymer\ phase}{cell\ volume}$$

$$\Phi_{air} = \frac{volume\ occupied\ by\ air\ phase}{cell\ volume}$$

(31)

In this thesis, unless explicitly stated, all the coefficients of the flow equations are volume averaged. A generic conservation equation is used to demonstrate this here, in Equation 30. The differential equation governing the evolution of a flux in and through a fluid volume is cast in conservation form:

$$\int_{\Omega} \frac{\partial(\rho\phi)}{\partial t} d\Omega + \int_{A} \rho\phi U \cdot \vec{n}\, dA = \int_{A} \Gamma_{\phi} \nabla\phi \cdot n dA + \int_{Q} q_{\phi} d\Omega$$

(32)

where $\vec{n}$ is the normal vector to the differential area dA, q_{ϕ} is an arbitrary source term of the variable ϕ, $\nabla\phi$ is the gradient of ϕ and Ω is the cell volume.

Equation 32 is descretised as follows:

$$\frac{\partial(\rho\phi)}{\partial t}\Omega + \sum_{f}^{N} \rho_f \phi_f \vec{U}_f \cdot n A_f = \sum_{f}^{N} \rho_f \Gamma_{\phi} \nabla\phi \cdot n A_f + q_{\phi}\Omega$$

(33)

$\vec{U}_f$ is the fluid velocity vector on the face of the control volume, $\vec{n}$ is the normal vector to the area dA, The subscript f denotes the faces of the cell and N is the total number of faces. The value of ϕ on a particular face is interpolated from the values at two neighbouring cell centers (nodes). For instance, the value of ϕ on the North

34

face of the two-dimensional control volume as shown in Figure 4.2 is determined from the interpolation of the two values at the cell centers of node P and node N. The form of the interpolation is determined by the type of differencing scheme used. This results in a system of linear equations as in Equation (29). The coefficients of the linear equations form a sparse matrix, and the system is solved iteratively in FLUENT by means of a Gauss-Seidel type linear solver.

The discretization of the flow conservation equations results in systems of linear equations. However, different discretization schemes are suited for the conservation equations encountered in a variety of physical flow problems. For instance, the numerical treatment of the model equations for a convection-dominated flow would be different from a diffusion-dominated one. To this end, a parameter used to characterize the relative significance of these two flow features is the Peclet number; a dimensionless number that describes the ratio of the convective to diffusive term in the conservation equation:

$$Pe = \frac{\rho U_{avg} L}{\Gamma}$$
(34)

where U_{avg} is the fluid characteristic velocity (usually average velocity) and L is the characteristic length of the geometry.

4.2.3 Momentum

The three-dimensional conservation of momentum equation is obtained by substituting the velocities u, v and w in place of the term ϕ in Equation (32); the pressure gradient and shear stress terms may be incorporated into the gradient term on the right hand side, as follows:

X – momentum:

$$\frac{\partial(\rho u)}{\partial t}\Omega + \sum_{f}^{N}\rho_f u_f \vec{U}_f \cdot n\,A_f = \sum_{f}^{N}\rho_f \mu \nabla u \cdot n\,A_f \qquad (35)$$

Y – momentum:

$$\frac{\partial(\rho v)}{\partial t}\Omega + \sum_{f}^{N}\rho_f v_f \vec{U}_f \cdot n\,A_f = \sum_{f}^{N}\rho_f \mu \nabla v \cdot n\,A_f \qquad (36)$$

Z - momentum:

$$\frac{\partial(\rho w)}{\partial t}\Omega + \sum_{f}^{N}\rho_f w_f \vec{U}_f \cdot n\,A_f = \sum_{f}^{N}\rho_f \mu \nabla w \cdot n\,A_f \qquad (37)$$

where, u, v and w are described on the faces, 'f' of the control volume. As the Peclet number of the flow is larger than 1, a second order upwind scheme is used in the discretization of the momentum equation. A second order scheme implies that the approximation of the terms in the momentum equation takes place by accounting for a higher number of nodes on the grid, thus leading to greater accuracy. A first order scheme approximates values at a node based on data from one adjacent node, a second order scheme approximates values based on data from two adjacent nodes. Higher accuracy schemes have higher order truncation errors but tend to be more computationally expensive as they require data from more computational nodes on the grid. This is especially true in the case of the discrete approximation of scalar gradient terms.

4.2.4 The Staggered Grid Approach

Due to the fact that a second order scheme is implemented in the solution of the momentum equation, a staggered grid is used to prevent 'checkerboarding' of the resulting velocity and pressure field. This occurs when central differences are used to approximate all or some of the gradient terms in the flow equations. 'Checkerboard' results satisfy the discretised equations, but the values obtained are physically

36

unrealistic. The staggered grid option is enabled by turning on the Pressure Staggering Option (PRESTO).This scheme is offered in FLUENT 6.3 when the Volume of Fraction (VOF) equation is solved. A staggered grid essentially means that the pressure (and other scalars) and velocity values (and other vectors) are computed on different areas on the numerical grid. This is depicted for a two-dimensional grid in Figure 4.6.
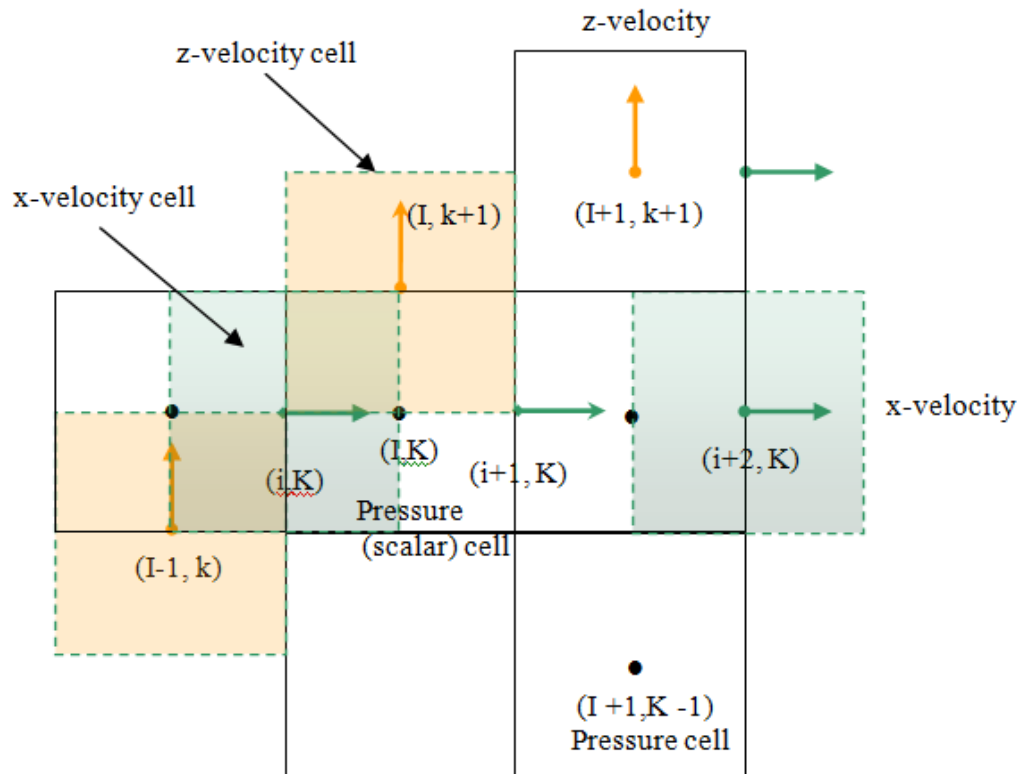
Fig.4.6: A two-dimensional staggered grid

As may be observed, the velocity cells (shaded) are displaced by half a grid distance from the pressure cell center. Thus, for the pressure control volume (CV), the velocity nodes appear on the face of the cell, and for the velocity control volume, the reverse occurs. In this manner, the discretised expressions for pressure and velocity are formulated on different control volumes which are distanced half a grid apart. The pressure and velocity gradients that appear on the faces of a control volume (for a pressure CV and velocity CV) are approximated from neighbouring pressure and velocity nodes respectively. The staggered grid scheme is readily extended to a three-dimensional case. The staggered grid formulation and the issue

37

of pressure-velocity coupling are quite closely related. In interest of clarity, the following section employs a slightly different form of notation – the compass notation used earlier is less convenient when applied to a staggered grid, thus a different notation system is used to locate pressure and velocity nodes. In addition to this, for simplicity, the momentum equation used here is the two-dimensional unsteady momentum equation. The methods for pressure-velocity coupling are easily extended to a three-dimensional case [43]. With reference to Figure 4.6, the pressure control volume(CV) is centred at node (I, K), the x – velocity (*u*) CV is centred at node (i+1,K) and the z-velocity (*w*) is centred at node (I, k+1).

The x -momentum conservation equation in discrete form may then be recast as follows:

$$
\frac{(\rho u)_{i,K}^{n+1} - (\rho u)_{i,K}^{n}}{\Delta t} \Omega = (\rho u u)_{I-1,K} A_{I-1,K} - (\rho u u)_{I,K} A_{I,K} + (\rho w u)_{i,k} A_{i,k} - (\rho w u)_{i,k+1} A_{i,k+1}
$$
$$
+ \left(\mu \frac{\partial u}{\partial x}\right)_{I,K} A_{i,J} - \left(\mu \frac{\partial u}{\partial x}\right)_{I-1,K} A_{i,J} + \left(\mu \frac{\partial u}{\partial z}\right)_{i,k+1} A_{i,K} - \left(\mu \frac{\partial u}{\partial z}\right)_{i,k} A_{i,K}
$$
$$
- (P_{I,K} - P_{I-1,K}) A_{i,K}
$$

(38)

where $\partial u/\partial x$ and $\partial u/\partial z$ are the velocity gradients, $A_{i,j}$ is the area of the face of the control volume at node (i,j) perpendicular to the velocity vector $u_{i,j}$ or $w_{i,j}$. The constituents (velocity and density) of the momentum and gradient terms are evaluated at the same nodes. Following this, as the momentum balance takes place on a x – velocity centred node, the velocities on the face of the control volume have to be interpolated from neighbouring velocity nodes. This is also true of the gradient terms. The interpolation method then depends upon the choice of discretization scheme used. As mentioned earlier, the second order upwind scheme has been chosen for the discretization of the momentum equation as the flow Peclet number is larger than 1. This is shown in Equation (39).

$$
u_{face} = u_{upwind} + (\nabla u \cdot r)_{upwind}
$$

(39)

38

where u_{face} is the face x-velocity of the control volume, and u_{upwind}, and $(\nabla u \cdot r)_{upwind}$ are determined at the cell center (node) of the cell immediately 'upwind' of the control volume. The term 'upwind' is taken with reference to the flow direction; r is the distance vector from the cell centre of the upwind cell to the face of the downwind cell.

The gradient term, $(\nabla u)_{upwind}$ is determined by means of the Green Gauss theorem:

$$(\nabla u)_{upwind} = \frac{1}{\Omega} \sum_f \bar{u}_{face} \cdot n \, A_f$$

(40)

where $\bar{u}_f$ is taken to be the average of the values at two neighbouring cell centers (nodes) adjacent to the face.

$$\bar{u}_{face} = \frac{u_{neigh\,1} + u_{neigh\,2}}{2}$$

(41)

neigh 1 and *neigh 2* denote the two neighbouring cells. This is termed the Green-Gauss Cell-based Gradient Evaluation. For instance,

$$u_{I,K} = u_{i-1,K} + (\nabla u \cdot r)_{i-1,K}$$

(42)

where

$$
\begin{aligned}
(\nabla u)_{i-1,K} &= \frac{1}{\Omega}\left(u_{I-1,K} A_{I-1,K} - u_{I-2,K} A_{I-2,K}\right) \\
&= \frac{1}{\Omega}\left[\frac{1}{2}\left(u_{i,K} + u_{i-1,K}\right)A_{I-1,K} - \frac{1}{2}\left(u_{i-2,K} + u_{i-1,K}\right)A_{I-2,K}\right]
\end{aligned}
$$

(43)

The gradient of u is evaluated with only x components of velocity, due to the fact that for a regular grid, the distance vector r solely points in the x – direction.

For the z – momentum equation,

39

$$w_{i,k+1} = w_{i,K-1} + \left(\nabla w \cdot r\right)_{i,K-1} \tag{44}$$

$$\begin{aligned}
\left(\nabla w\right)_{i,K-1} &= \frac{1}{\Omega}\left(w_{i,k}A_{i,k} - w_{i,k-1}A_{i,k-1}\right) \\
&= \frac{1}{\Omega}\left[\frac{1}{2}\left(w_{i,K} + w_{i,K-1}\right)A_{i,j} - \frac{1}{2}\left(w_{i,K-2} + w_{i,K-2}\right)A_{i,k-1}\right]
\end{aligned} \tag{45}$$

The discretised x-momentum equation results in a system of linear equations:

$$a_{i,K}u_{i,K} = \sum a_{neigh}u_{neigh} + \left(P_{I-1,K} - P_{I,K}\right)A_{i,K} + q_{i,K}\,\Omega \tag{46}$$

And the y – momentum equation in discrete form is:

$$a_{I,k}w_{I,k} = \sum a_{neigh}w_{neigh} + \left(P_{I,K-1} - P_{I,K}\right)A_{I,k} + q_{I,k}\Omega \tag{47}$$

Where a is the coefficient of the x-velocity term u. The conservation of momentum equation in the y – direction is treated in a similar matter.

Provided P and the mass flux, $\rho u_{i,J}$ are known, the system of equations may be solved. However, the pressure and velocity are not known a priori and have to be guessed or obtained as part of the solution. In FLUENT, the initial values are used for the first set of guess values.

4.2.5 Pressure – Velocity coupling: The Pressure Correction Method

The pressure and velocity terms are coupled in the sense that pressure values throughout the flow field may be obtained once the velocity field is known, and vice versa. The solution algorithm used by FLUENT guesses pressure values first then uses these values to solve the momentum equation to obtain the x, y and z velocities (u*, v*, w*) as shown in Figure 4.5. Back-substituting these values into the momentum equation to obtain the pressure field is meaningless, unless they are 'corrected' first. This process termed 'pressure correction' operates in the following manner:

1. Guess initial pressure field, pressure values are denoted P^*

2. Use P^* to solve the momentum equation to obtain u^*, v^* and w^*

3. Derive the expression for the corrector velocities u', v' and w' in terms of the pressure correction term P'.

4. Substitute u^*, v^* and w^* and P' into the continuity equation and solve for the pressure correction P' that will satisfy the discretized continuity equation. The corrected pressure field is obtained.

$$P = P^* + P'$$

5. The corresponding 'corrections' u', v' and w' may be obtained from P' such that:

$$u = u^* + u'$$
$$v = v^* + v'$$
$$w = w^* + w'$$

6. Setting the new $P^* = P$, the sequence is repeated until the pressure correction terms are minimized and the guess velocities satisfy the continuity equation. When this is achieved, then the correct velocity field is obtained.

This process is described in greater detail for a two-dimensional case:

First, the initial pressure field is guessed, P^* resulting in a guessed velocity field as follows:

x- velocity:

$$a_{i,K} u_{i,K}^* = \sum a_{nb} u_{nb}^* + \left(P_{I-1,K}^* - P_{I,K}^* \right) A_{i,K}$$

(48)

z-velocity:

$$a_{I,k} w_{I,k}^* = \sum a_{nb} w_{nb}^* + \left(P_{I,K-1}^* - P_{I,K}^* \right) A_{I,k}$$

(49)

The pressure and velocity correction terms are defined as follows:

41

$P' = P - P*$

$u' = u - u*$

$w' = w - w*$

Then, the guessed velocity field in terms of the velocity corrections may be written:

x- corrected velocity:

$$a_{i,K} u'_{i,K} = \sum a_{nb} u'_{nb} + \left(P'_{I-1,K} - P'_{I,K} \right) A_{i,K} \tag{50}$$

z- corrected velocity:

$$a_{I,k} w'_{I,k} = \sum a_{nb} w'_{nb} + \left(P'_{I,K-1} - P'_{I,K} \right) A_{I,k} \tag{51}$$

The scheme used for the two and three – dimensional simulations in this work is the Pressure-Implicit with Splitting of Operators (PISO) scheme. This choice is motivated by the fact that pressure and velocity are strongly coupled for mold – filling flows. Thus, an accurate and robust guess – correct algorithm is required. It is a modification of the Semi-Implicit Method for Pressure-Linked Equations or SIMPLE [45] algorithm.

The SIMPLE algorithm applies an approximation to compute the corrected velocities. It is assumed that the corrected velocity at a particular node is a function of the corrected pressures at the node only, such that:

$$u'_{i,K} = \frac{A_{i,K}}{a_{i,K}} \left(P'_{I-1,K} - P'_{I,K} \right) = d_{i,K} \left(P'_{I-1,K} - P'_{I,K} \right) \tag{52}$$

and

$$w'_{I,k} = \frac{A_{I,j}}{a_{I,j}}\left(P'_{I,K-1} - P'_{I,K}\right) = d_{I,k}\left(P'_{I,K-1} - P'_{I,K}\right)$$

(53)

It should be noted that this omission of the velocities at the neighbouring nodes is only enforced when the momentum equation has been fully discretised, and thus it is merely a numerical trick and is in no way due to any physical insight of the flow [41]. What this does however, is to effectively decouple the velocity at a particular node from other velocity nodes in the grid so that the velocity value may be known once the pressure at the two neighbouring scalar nodes is known.

Now, the 'real' velocities may be expressed as follows:

$$u_{i,K} = u^{*}_{i,K} + d_{i,K}\left(P'_{I-1,K} - P'_{I,K}\right)$$

(54)

$$w_{I,k} = w^{*}_{I,k} + d_{I,k}\left(P'_{I,K-1} - P'_{I,K}\right)$$

(55)

Now that the formulation for the 'real' velocity in terms of the guessed velocity and pressure correction terms is derived, these terms are in turn substituted into the flow continuity equation.

The incompressible flow continuity equation derived at node (I,K) in discretised form is:

$$\left(\frac{\rho^{n} - \rho^{n-1}}{\Delta t}\right)\Omega + \left(\rho u A\right)_{i+1,k} - \left(\rho u A\right)_{i,K} + \left(\rho w A\right)_{I,k+1} - \left(\rho w A\right)_{I,k} = 0$$

(56)

The other two discrete expressions for velocity required are:

$$u_{i+1,K} = u^*_{i+1,K} + d_{i+1,K}\left(P'_{I,K} - P'_{I+1,K}\right)$$

(57)

$$w_{I,k+1} = w^*_{I,k+1} + d_{I,k+1}\left(P'_{I,K} - P'_{I,K+1}\right)$$

(58)

Substituting these discrete approximations of the velocity into the flow continuity equation, a linear system of equations in terms of the pressure correction term is obtained:

$$\begin{bmatrix} (\rho dA)_{i+1,K} + (\rho dA)_{i,K} \\ + (\rho dA)_{I,k+1} + (\rho dA)_{I,k} \end{bmatrix} P'_{I,K} = \begin{bmatrix} (\rho dA)_{i+1,K}\, P'_{I+1,K} + (\rho dA)_{i,K}\, P'_{I-1,K} \\ + (\rho dA)_{I,k+1}\, P'_{I,K+1} + (\rho dA)_{I,k}\, P'_{I,k-1} \end{bmatrix} + \begin{bmatrix} \left(\rho u^* A\right)_{i,K} - \left(\rho u^* A\right)_{i+1,K} \\ + \left(\rho v^* A\right)_{I,k} - \left(\rho v^* A\right)_{I,k} - \left(\dfrac{\rho^n - \rho^{n-1}}{\Delta t}\right)\Omega \end{bmatrix}$$

(59)

or,

$$C_{I,K} P'_{I,K} = C_{i+1,K} P'_{I+1,K} + C_{I-1,K} P'_{I-1,K} + C_{I,K+1} P'_{I,K+1} + C_{I,K-1} P'_{I,K-1} + b'_{I,K}$$

(60)

As may be observed, the equation now reduces to a system of linear equations which may be solved iteratively to obtain the values of P'. The term $b'_{I,K}$ is basically the steady continuity equation discretised by a central difference scheme about node (I,K), such that for a control volume centered at node (I,K), the guess velocities u^* and w^* are located on the faces of the control volume. With progressing iterations, the term $b'_{I,K}$ should reduce gradually to zero. Once this happens, the solution p' added to p^* will yield the solution to the 'real' pressure P. In order to aid the convergence of the solution, under-relaxation of the solution is used in this manner:

$$P^{N+1} = P^N + \alpha_P P'$$

(61)

44

where N denotes the number of iterations, P^{N+1} becomes the guessed value for iteration number N+1. α_P is the relaxation factor ranging from 0 to 1 which is introduced in order to regulate the change in pressure values from one iteration to the next in order to prevent divergence in the solution. The velocity (momentum) solution is similarly under-relaxed.

The PISO scheme introduces an additional corrector step performed within the pressure correction loop. In essence, the 'real' velocity values obtained from the SIMPLE algorithm are used to generate a second approximation of the pressure values (while the pressure was initially guessed at the beginning of the SIMPLE algorithm, once the 'real' velocities are obtained, the momentum equation may be re-solved to obtain the 'real' pressure. This is then substituted into a second velocity approximation scheme). In effect, the SIMPLE algorithm is performed twice, one loop within another. By way of a trade-off, the convergence rate of the pressure correction term increases at the expense of greater computational cost. This is shown in Figure 4.7.

START

Initialize u,v, *P* and other transport variables, Set the time step size Δ*t*.

Set t = t + Δ*t*, u*=u, v*=v, set the initial guess values of the other transport equation parameters to be the values of the previous time step

1

Solve the pressure correction equation to obtain the pressure correction terms *P'*

2

Solve the discretized momentum equation in order to obtain the guess velocities u* and v*

3

Obtain the corrected pressure and velocity fields, *P*, *u* and *v*

Utilizing the corrected pressure and velocity values as guess values, steps 1,2 and 3 are performed for a second time in order to obtain a second set of corrected pressure and velocity values. Solve the other transport equations.

No
Convergence
Set *P**=P*

Yes

Is t > t$_{max}$?
Set *P**=P*

Yes

Stop

Fig.4.7: PISO solution algorithm for a transient flow

4.2.6 Energy

The energy equation has to be solved in order to model the temperature of the fluid; a second order upwind scheme is also used here. As the energy equation is a scalar equation, the discrete form of the equation is solved on the pressure control volume. Therefore, the temperature is calculated on the same set of nodes as the pressure. The form of the energy equation solved in FLUENT is a more general form of the energy equation presented in the theory section of this report. However, as will be demonstrated, they are equivalent if certain assumptions are introduced. The energy equation model solved in FLUENT is:

$$\frac{\partial(\rho E)}{\partial t} + \nabla \cdot [U(\rho E + P)] = \nabla \cdot \left[k\nabla T + \bar{\tau}_{eff} \cdot U \right]$$

(62)

where

$$E = h - \frac{P}{\rho} + \frac{U^2}{2}; \quad h = \int_{T_{ref}}^{T} c_p dT$$

(63)

where $\bar{\tau}_{eff}$ is the effective shear stress, and S_h is the source term. For a two-dimensional case, this may be expanded to give:

$$
\begin{bmatrix}
\dfrac{\partial}{\partial t}\left[\rho\displaystyle\int_{T_{ref}}^{T} c_p dT - P + \dfrac{u^2 + w^2}{2} \right] + \\[4mm]
\dfrac{\partial}{\partial x}\left[u\left(\rho\displaystyle\int_{T_{ref}}^{T} c_p dT + \dfrac{u^2 + w^2}{2} \right) \right] + \\[4mm]
\dfrac{\partial}{\partial z}\left[w\left(\rho\displaystyle\int_{T_{ref}}^{T} c_p dT + \dfrac{u^2 + w^2}{2} \right) \right]
\end{bmatrix}
=
\begin{bmatrix}
\dfrac{\partial}{\partial x}\left[k\dfrac{\partial T}{\partial x} \right] + \dfrac{\partial}{\partial z}\left[k\dfrac{\partial T}{\partial z} \right] + \\[4mm]
\dfrac{\partial}{\partial x}\left[\mu\left(\dfrac{\partial u}{\partial x} + \left(\dfrac{\partial u}{\partial z} + \dfrac{\partial w}{\partial x} \right) \right) \cdot u \right] + \\[4mm]
\dfrac{\partial}{\partial z}\left[\mu\left(\dfrac{\partial w}{\partial z} + \left(\dfrac{\partial w}{\partial x} + \dfrac{\partial u}{\partial z} \right) \right) \cdot w \right]
\end{bmatrix}
$$

(64)

The viscous energy terms may be manipulated to yield:

$$\left[\begin{array}{c} \dfrac{\partial}{\partial x}\left[\mu\left(\dfrac{\partial u}{\partial x}+\left(\dfrac{\partial u}{\partial z}+\dfrac{\partial w}{\partial x}\right)\right)\cdot u\right]+ \\ \dfrac{\partial}{\partial z}\left[\mu\left(\dfrac{\partial w}{\partial z}+\left(\dfrac{\partial w}{\partial x}+\dfrac{\partial u}{\partial z}\right)\right)\cdot w\right] \end{array}\right] = \left[\begin{array}{c} \mu\left[2\left(\dfrac{\partial u}{\partial x}\right)^2+\left(\dfrac{\partial u}{\partial z}+\dfrac{\partial w}{\partial x}\right)^2+2\left(\dfrac{\partial w}{\partial z}\right)^2\right]+ \\ \mu\left[2u\dfrac{\partial^2 u}{\partial x^2}+u\dfrac{\partial^2 u}{\partial z^2}+v\dfrac{\partial^2 w}{\partial z^2}+w\dfrac{\partial^2 w}{\partial x^2}\right] \end{array}\right]$$

(65)

If it is assumed that the specific heat capacity c_p is constant, that the kinetic energy terms are small and that the rate of change of pressure P is also small, and if it is also further assumed that the second derivatives of velocity are small in comparison to the square of the first derivatives, then the energy equation readily simplifies to:

$$\rho c_p\left(\dfrac{\partial T}{\partial t}+u\dfrac{\partial T}{\partial x}+w\dfrac{\partial T}{\partial z}\right)=\dfrac{\partial}{\partial x}\left[k\dfrac{\partial T}{\partial x}\right]+\dfrac{\partial}{\partial z}\left[k\dfrac{\partial T}{\partial z}\right]+\mu\dot{\gamma}^2$$

(66)

where

$$\dot{\gamma}=\sqrt{\left[2\left(\dfrac{\partial u}{\partial x}\right)^2+\left(\dfrac{\partial u}{\partial z}+\dfrac{\partial w}{\partial x}\right)^2+2\left(\dfrac{\partial w}{\partial z}\right)^2\right]}$$

(67)

Equation (66) is a two – dimensional equivalent of Equation (10) described in Chapter 2.

4.2.7 Volume Fraction Equation

The solution of the volume fraction equation (Equation (11)) described in the previous chapter is necessary in order to model the mold – filling process. Of special interest is the capture of a clearly defined suspension – air interface that marks the transition from the suspension flow to the air domain as shown in Figure 4.8. The

48

implementation of the volume fraction equation is also popularly known as the Volume – of – Fluid (VOF) method [46]. A High-Resolution Interface Capturing (HRIC) scheme is used to numerically solve the volume fraction equation [47]. The HRIC scheme allows for the smooth switching between an Upwind, Central and Downwind differencing scheme of the volume fraction equation depending upon the local distribution of the phase volume fraction [47]. This scheme is known to produce a clear definition of the fluid interface, whilst being relatively cheap in terms of computational cost as compared with geometry reconstruction schemes [47].
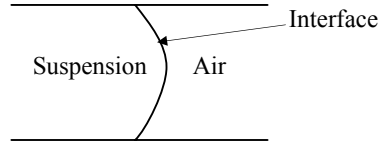
Fig.4.8: The suspension-air interface

The volume fraction equation in the volume integral form is:

$$\int_{\Omega} \frac{\partial(\rho\,\Phi)}{\partial t} d\Omega + \int_{A} \rho\,\Phi\,U \cdot n\,dA = 0 \tag{68}$$

The volume fraction itself is defined as follows:

$$\Phi_{polymer} = \frac{cell\ volume\ occupied\ by\ suspension\ phase}{cell\ volume}$$

$$\Phi_{air} = \frac{cell\ volume\ occupied\ by\ air\ phase}{cell\ volume}$$

From the conservation of volume, it may be seen that:

49

$$\Phi_{air} + \Phi_{suspension} = 1$$

Thus, $\Phi_{air} = 1 - \Phi_{suspension}$ or vice versa, and so, the volume fraction equation has to be solved for one variable only, as once the volume fraction of one phase is known, the other can be found easily.

As the volume fraction Φ is a scalar, this equation is discretised and solved on the pressure grid as shown in Figure 4.9.
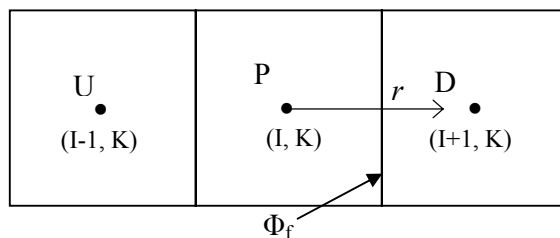
Fig.4.9: Volume fraction equation discretization and solution on the pressure grid

A description of the HRIC scheme is limited to a consideration of only one spatial dimension (the x-direction) in favour of simplicity and clarity.

Φ_f is the volume fraction value on the face of the principal cell (cell P). Φ_f has to be numerically approximated; however, the numerical scheme used to achieve this is switched depending upon the local cell-centered values of Φ; Φ_P, Φ_U and Φ_D.

A normalized variable of the cell-centred values of Φ, termed $\widetilde{\Phi}_c$ is introduced. It is a measure of the gradient of the volume fraction between cells U, D and P, and is the criteria for switching the numerical schemes used to estimate the parameter Φ_f.

$$\widetilde{\Phi}_C = \frac{\Phi_D - \Phi_U}{\Phi_P - \Phi_U}$$

(70)

The numerical schemes are the: first order upwind, central difference and first order downwind scheme.

$$\tilde{\Phi}_f = \tilde{\Phi}_C \quad if \quad \tilde{\Phi}_C < 0 \quad or \quad \tilde{\Phi}_C > 1 \; (upwind)$$
$$\tilde{\Phi}_f = 2\tilde{\Phi}_C \quad if \quad 0 \leq \tilde{\Phi}_C < 0.5 \; (central)$$
$$\tilde{\Phi}_f = 1 \quad if \quad 0.5 \leq \tilde{\Phi}_C \leq 1 \; (downwind) \tag{71}$$

In the event that the flow at the interface is parallel to the interface surface itself, 'wrinkles' in the interface may occur, where there could be jumps in values of the volume fraction Φ_f from one adjacent cell to another. In order to prevent this, the value of the face volume fraction is corrected, taking into account the direction of the flow, and the location of the interface. This correction scheme is termed ULTIMATE-QUICKEST [48].

$$\tilde{\Phi}_f^{UQ} = \tilde{\Phi}_C \quad if \quad \tilde{\Phi}_C < 0 \quad or \quad \tilde{\Phi}_C > 1$$
$$\tilde{\Phi}_f^{UQ} = \min\left(\tilde{\Phi}_f, \frac{6\tilde{\Phi}_C + 3}{8}\right) \quad if \quad 0 \leq \tilde{\Phi}_C \leq 1 \tag{72}$$

The volume fraction correction term is:

$$\tilde{\Phi}_f^* = \tilde{\Phi}_f \sqrt{\cos\theta} + \left(1 - \sqrt{\cos\theta}\right)\tilde{\Phi}_f^{UQ} \tag{73}$$

where,

$$\cos\theta = \frac{\nabla\Phi \cdot \vec{r}}{\left|\nabla\Phi \right| \cdot \left| \vec{r}\right|} \tag{74}$$

The unit vector normal to the fluid interface is given as:

$$\vec{n} = \frac{\nabla\Phi}{\left|\nabla\Phi\right|} \tag{75}$$

And the unit vector representing the x-velocity direction is drawn from the centre of cell P to cell D as shown in Figure 4.9.

51

$$\hat{r} = \frac{\vec{r}}{|r|} \tag{76}$$

Thus the dot product of the two may be manipulated to give the angle between the vector normal to the interface and the vector parallel to the velocity.

The face volume fraction may then be expressed as:

$$\Phi_f = \tilde{\Phi}_f^* (\Phi_A - \Phi_U) + \Phi_U \tag{77}$$

4.2.7.1 Pseudo-concentration Method

The simulation of the mold – filling flow encounters two separate fluids – suspension and air, of vastly different densities, viscosities and thermal properties. This creates problems with the numerical stability of the equations to be solved. For instance, the suspension density and viscosity is of the order $O(10^3\,\text{kg/m}^3)$ and $O(10^3$ Pa.s) respectively, while the air density and viscosity is of the order $O(1\,\text{kg/m}^3)$ and $(10^{-5}$ Pa.s) respectively. In cells that are a mixture of air and suspension, the properties of the fluid in the cell are averaged by considering the volume fraction of the individual phases, for instance:

$$\rho = \rho_{suspension} \times \Phi_{suspension} + \rho_{air} \times \Phi_{air}$$
$$\mu = \mu_{suspension} \times \Phi_{suspension} + \mu_{air} \times \Phi_{air}$$
$$\tag{78}$$

Due to the large differences in the properties of the suspension and air, even a small amount of the suspension phase results in a significant change in the fluid properties of a particular cell. This may cause blow-ups, especially in the momentum equations when fluid momentum is transferred across the interface from the predominantly suspension zone, to the predominantly air one. A possible solution is to solve two separate momentum equations: one for the suspension and another for the air. This however, consumes system resources. The pseudo-concentration method introduced by Haagh and Vosse is an intelligent way of dealing with this potential problem [49]. Scaling arguments may be used to demonstrate that, the most

52

significant terms in the momentum equation for the suspension phase, are the viscous and pressure gradient terms:

$$0 = -\nabla P + \nabla \cdot \left(\mu \nabla U \right)$$ (79)

Similarly, scaling arguments may also be used to show that for the air phase, the most significant terms are the inertial and gravity terms:

$$\rho \frac{\partial U}{\partial t} + U \cdot \nabla U = \rho g$$ (80)

The scaling arguments used to demonstrate this are elaborated in detail in Appendix A of this thesis.

As the phase of concern is the suspension phase – this is the phase in which the short-fibers are suspended, the behaviour of the air phase is of significantly less concern. By introducing a fictitious fluid or a 'pseudo-fluid' in place of air, the momentum equation of the air phase may be altered so that the significant terms are the pressure gradient and the viscous terms. Then, only one momentum equation has to be solved for both suspension and air phases. This process is simply done by substituting the physical properties of air with 'pseudo-fluid' properties: in effect, the viscosity is changed to a constant 1 Pa.s. This value is small enough that it doesn't cause unrealistic pressure buildups in the air phase, but large enough that the viscous terms in the air phase is large.

However, as FLUENT solves a generic transport equation for the entire domain, the modification of air viscosity to that of 'pseudo-air' is necessary only so that the gravity term of the momentum equation may be dropped. In order to avoid confusion, the 'pseudo – air' phase is referred to simply as 'air' for the remainder of this thesis.

Additionally, the presence of two phases of vastly different viscosities presents difficulties for the definition of the slip boundary at the wall due to the fact that a stress singularity develops at the contact point of the suspension, air and wall [50].

In order to remedy this, a dynamic slip boundary is imposed where the slip condition on the wall is switched depending upon the phase present: no-slip for suspension and free-slip for air. A User-Defined Function (UDF) was written into FLUENT 6.3 to allow for the dynamic switching of slip conditions from no-slip to free-slip (traction free) depending upon the phase present at the wall.

The algorithm is as follows:

1. Access cells on wall boundary:

2. Check polymer volume fraction (Φ) of wall boundary cell

    If ($\Phi >= 0.5$)
        Set velocity in wall boundary cell to zero. (no-slip)

    Else
        Set velocity in wall boundary cell to the velocity of the
        cell adjacent to the wall boundary (free-slip)

For a predominantly suspension – filled wall boundary cell (defined as a cell with a volume fraction Φ equal to or greater than 0.5) the slip condition is 'no-slip' whereby the fluid velocity is set to zero at the wall boundary. For a predominantly air filled cell, the condition is 'free-slip' and the velocity in the cell is equal to that of the adjacent cell. The UDF was written in C – programming language and compiled in FLUENT.

4.3 Numerical Implementation of the Fiber Orientation Evolution Equation

The two – dimensional fiber orientation evolution equation was solved utilizing flow field data extracted on Plane A as shown in Figure 5.6. The numerical solution of the fiber orientation was performed in Matlab. Due to the decoupled approach to solving this problem, the fiber orientation evolution equation may be independently solved. Breaking up the tensor a_{ij} into its five independant constituent components; a_{11}, a_{22}, a_{12}, a_{13} and a_{23}, as explained in 2.5.1 results in five separate orientation equations that have to be solved in tandem. The a_{33} component is obtained from the normalization condition ($a_{33} = 1 - a_{11} - a_{22}$).

Each of these orientation equations is descretized by means of the finite difference method, utilizing the flow field data obtained from FLUENT as the coefficients of the resulting system of linear equations.

4.3.1 Finite Difference Method

The finite difference method implements the discretization of Equation 30 in its non - conservation or differential form. This is achieved by representing the differential forms of Equation 30 as truncated forms of Taylor series, and is demonstrated here by re-examining the one-dimensional convective-diffusive from Equation 23. With respect to Equation 24, the finite difference form of the equation is:

$$\frac{(\rho \phi u)_e - (\rho \phi u)_w}{2\delta x} = \Gamma_P \frac{\phi_E - 2\phi_P - \phi_W}{\delta x^2} \tag{81}$$

The reference for the discretization process are the nodes themselves, not the fluid volumes. The grid points upon which the fiber orientation equation is discretized coincides with the cell centers of the finite volume grid, as shown in Figure 4.10. Two grids, one a finite difference grid, and another finite volume one are superimposed to demonstrate how the finite difference grid is obtained from the latter by shifting the reference from the cell center to the grid points.
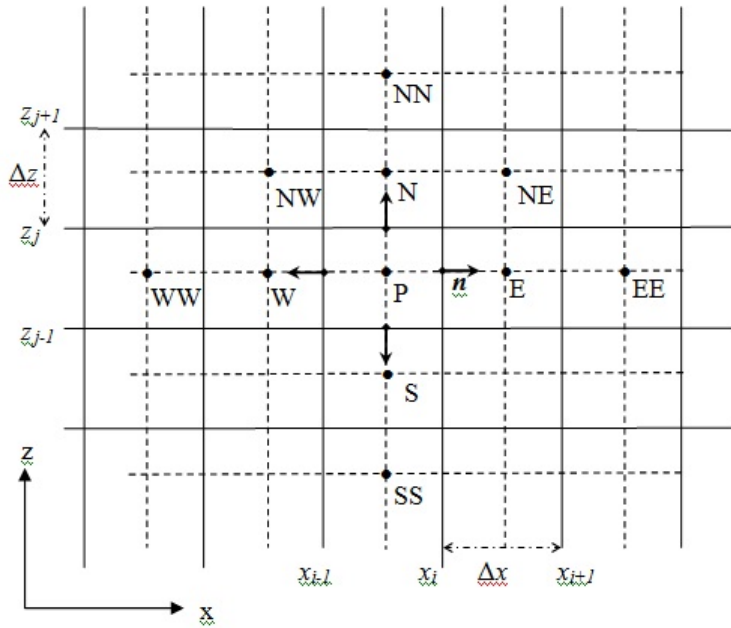
Fig.4.10: A two-dimensional finite difference grid superimposed over a finite volume grid. (The finite difference grid is drawn with broken lines and the finite volume one is drawn with solid lines)

4.3.2 Fiber Orientation Evolution Numerical Scheme

The Crank-Nicolson scheme is used to discretize the fiber orientation evolution equation. This choice was predicated upon the fact that the Crank-Nicolson (C-N) scheme is stable for a broad range of time steps [52]. The philosophy behind the C-N scheme is to combine an explicit or forward differencing scheme which is first order accurate in time, with an implicit or backward one, and central differencing for the spatial terms to obtain a stable numerical scheme that is second order accurate in both time and space. Consider for instance the one dimensional unsteady convective equation:

$$ \tag{82} $$

The C – N scheme selects the time $t+0.5\Delta t$ as the point in time around which the equation is discretized. A central difference scheme is used for the spatial terms, and in addition the spatial terms are averaged at two different time steps to obtain an expansion around $t+0.5\Delta t$. This is demonstrated as follows:

$$\frac{1}{2}\frac{(\rho\phi)_I^{n+1} - (\rho\phi)_I^{n+0.5}}{0.5\Delta t} + \frac{1}{2}\frac{(\rho\phi)_I^{n+0.5} - (\rho\phi)_I^{n}}{0.5\Delta t} + \dots$$

$$\frac{1}{2}\left[\frac{(\rho\phi)_{I+1}^{n+1} - (\rho\phi)_{I-1}^{n+1}}{2\Delta x}\right] + \frac{1}{2}\left[\frac{(\rho\phi)_{I+1}^{n} - (\rho\phi)_{I-1}^{n}}{2\Delta x}\right] = 0$$

(83)

Applied to the two – dimensional fiber orientation evolution equation, this results in:

$$\frac{(a_{ij})_{I,K}^{n+1} - (a_{ij})_{I,K}^{n}}{\Delta t} + \frac{1}{2}\left[u_{I,K}\frac{(a_{ij})_{I+1,K}^{n+1} - (a_{ij})_{I-1,K}^{n+1}}{2\Delta x} + u_{I,K}\frac{(a_{ij})_{I+1,K}^{n} - (a_{ij})_{I-1,K}^{n}}{2\Delta x}\right] + \dots$$

$$+ \frac{1}{2}\left[w_{I,K}\frac{(a_{ij})_{I,K+1}^{n+1} - (a_{ij})_{I,K-1}^{n+1}}{2\Delta z} + w_{I,K}\frac{(a_{ij})_{I,K+1}^{n} - (a_{ij})_{I,K-1}^{n}}{2\Delta z}\right] =$$

$$- \left[(\omega_{ik}a_{kj})_{I,K}^{n} - (a_{ik}\omega_{kj})_{I,K}^{n}\right] + \lambda\left[(\dot{\gamma}_{ik}a_{kj})_{I,K}^{n} + (a_{ik}\dot{\gamma}_{kj})_{I,K}^{n} - 2(\dot{\gamma}_{kl}A_{ijkl})_{I,K}^{n}\right] + \dots$$

$$+ 2C_I|\dot{\gamma}|_{I,K}^{n} \cdot (\delta_{ij} - 3a_{ij})_{I,K}^{n}$$

(84)

where λ is the aspect ratio of the short fibers, taken to be 1 in this work. Δx and Δz represent the grid spacing in the x and z directions and are identical to those used in the FLUENT simulations. It should be noted here that the source terms on the right-hand side of the equation are evaluated at time level t, however, tensor components which are part of the source term that match the i,j index are averaged between the two time steps.

These terms may then be re-combined and re-arranged to yield the following set of linear equations:

$$A\left(a_{ij}\right)_{I,K}^{n+1} = B\left[\left(a_{ij}\right)_{I+1,K}^{n+1}, \left(a_{ij}\right)_{I-1,K}^{n+1}, \left(a_{ij}\right)_{I,K+1}^{n+1}, \left(a_{ij}\right)_{I,K-1}^{n+1}\right] + \ldots$$

$$+ C\left[\left(a_{ij}\right)_{I+1,K}^{n}, \left(a_{ij}\right)_{I-1,K}^{n}, \left(a_{ij}\right)_{I,K}^{n}, \left(a_{ij}\right)_{I,K+1}^{n}, \left(a_{ij}\right)_{I,K-1}^{n}\right] + \ldots$$

$$+ S\left[\left(a_{kj}\right)_{I,K}^{n}, \left(A_{ijkl}\right)_{I,K}^{n}\right]$$

(85)

where A is the coefficient matrix of the time dependant term, $(a_{ij})^{t+1}$. B and C are the convective coefficients at time level $t+1$ and t respectively. S is the source term which includes the fourth order orientation closure terms. This results in a 5-diagonal sparse matrix that is diagonally dominant and thus may be solved by the Gauss-Seidel iteration method [53].

Although the Crank-Nicolson scheme is unconditionally stable, oscillations may develop if the ratio of the time step size to grid size is large. Furthermore, the fourth order orientation closure terms are non-linear for the case of the hybrid and quadratic closure. Thus, von Neumann stability analysis was performed in order to find a suitable time step size that would ensure a stable solution of the system of linear equations. The detailed workings for the a_{11} orientation evolution with the quadratic closure implemented are included in the Appendix B of this thesis. Due to the fact that the orientation components derive from ensembles of unit vectors, the range of possible real values are bounded. It was found that allowing any tensor component to 'stray' out of this range resulted very quickly in numerical blow-up within a few time steps, thus they have to be constrained:

$$0 \le a_{ij} \le 1 \quad for \; a_{11}, a_{22}$$
$$-0.5 \le a_{ij} \le 0.5 \quad for \; a_{12}, a_{13}, a_{23}$$

(86)

This is achieved by implementing a bounding function at the end of each iterative loop in order to capture values which drift out of bounds and push them back within the appropriate limits.

58

4.3.3 Solution Method and Algorithm

The series of linear equations developed from the discretization of the fiber orientation evolution equation may then be solved iteratively. The solution algorithm is laid out in Figure 4.11. As may be observed, there are two separate iteration loops which are in actual fact nested, one inside the other. First, there is the time advancement loop which governs the incremental increase in the number of time steps, and second, nested inside is the iteration loop that iterates the evolution equations of a_{11}, a_{22}, a_{12}, a_{13} and a_{23} to convergence. The converged solution is then checked to assess if it has achieved a steady-state result. This is assessed based upon a 'steadiness' criterion where the results from two consecutive time steps are compared to assess if the difference between them have fallen below a certain threshold. If this has not been achieved, then the time step is advanced and the iteration loop begins again.

START

The flow field data from FLUENT is imported into Matlab via MS Excel.
The coefficient matrices for the discretized orientation terms are generated

The fiber orientation is initialized over the numerical grid:
a11, a22, a12, a13 and a23 values are supplied for each node.

Guess a11, a22, a12, a13 and a23

Fiber orientation evolution equations are solved in sequence for each tensor component: a11, a22, a12, a13 and a23

Set computed a11, a22, a12, a13 and a23 values to be the 'guess' values

No — Convergence

Update a11, a22, a12, a13 and a23 values over the entire grid

Yes

Steadiness — No

Yes

Stop

Fig.4.11: Solution algorithm of the fiber orientation evolution equation

4.4 Summary

Due to the fact that the fiber orientation evolution equation is solved in a decoupled manner, the numerical solution proceeds in two stages. First, the gradual filling of the empty mold is simulated; this is accomplished through a commercial CFD code. The finite volume method is employed to accomplish this. A two dimensional segment of the flow field is extracted, and the fiber orientation evolution equation is solved, using the flow field data as coefficients for the numerical solution. This is implemented by means of the finite difference method.

CHAPTER 5

5.0 Introduction

Two test cases were used to verify the accuracy of the simulation as a whole. A solved numerical problem from literature due to Hieber [39] was used to assess the validity of the mold – filling solution method. The setup of the validation case is elaborated in Section 5.1. Section 5.2 discusses the setup for the three-dimensional simulation of the mold-filling flow and the subsequent solution of the fiber orientation equation. The experimental results of Bay [29] were used to assess the accuracy of the numerical solution to the fiber orientation evolution equation and the related closure models.

5.1 Test Case 1: Hieber's Mold – Filling Simulation

Hieber [39] performed a two-dimensional simulation of the gradual filling of an empty rectangular cavity of dimensions 200mm x 25mm x 2mm, by a hot polystyrene-type polymer. This work was used by Bay [21] as a test case for the numerical solution algorithm of the mold – filling flow, and is used here in this work for the same purpose. The choice of this problem as a test case was motivated by the fact that the salient features of the polymer flow encountered in Hieber's work are similar to ours, namely, a high viscosity, non-isothermal flow nature where the length of the flow domain is much greater than its height.

A two-dimensional simulation was performed where the choice of flow equations and solution controls are identical to those described earlier in Chapter 4.2.

The pseudo-concentration method and the dynamic slip model described in Chapter 3.2.8 was applied.

Hieber [39] simplified the three – dimensional geometry of the empty cavity to a two – dimensional rectangular domain of dimensions 200mm x 2mm. As the geometry exhibits top-bottom symmetry, a symmetry line is implemented through the middle of the domain. This effectively reduces the computational cost by half. A diagram of the computational domain is shown in Figure 5.1.
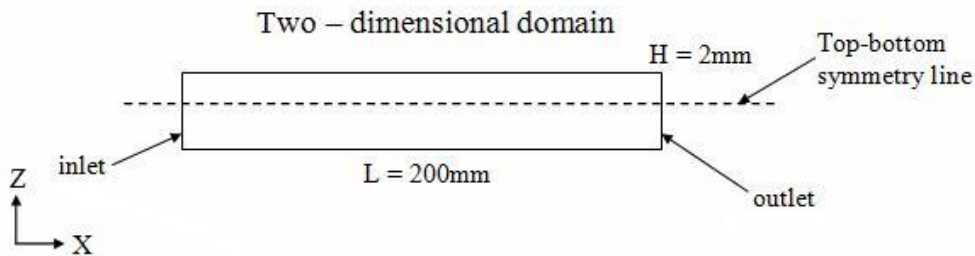
Fig.5.1: Two dimensional domain of the Hieber case [39]

A velocity boundary was used for the inlet with an inlet velocity of 0.2m/s (computed with respect to a filling time of 1s) with an inlet temperature of 473 K. An initial inlet pressure was specified to be 10^7 Pa. The wall temperature was 300K, and a pressure outlet was used for the mold outlet, where the pressure was set to 0 Pa (gage). The generation of the two – dimensional mesh was performed in Gambit 2.4, a preprocessing software accompanying FLUENT 6.3. A uniform grid size of 0.0001m was used in both the x and z directions. This choice of grid size is identical to that used by Hieber [39]. The polymer was modeled with a Power Law relation and Arrhenius temperature dependence. The material properties of the polymer are listed in Table 5.1. For the air phase, the pseudo-air properties listed in Table 5.5 are used. Simulation data was extracted from a location corresponding to a distance of 0.1m from the mold inlet, after complete filling of the mold was achieved. The time step size and relaxation factors for each iteration are the same as those used for Test Case 2, as listed in Table 5.6.

64

Table 5.1

Polymer material properties of the Hieber case [39]

Property	Value	Units
Density, ρ	940	kg/m3
Specific heat capacity, Cp	2100	J/kg.K
Thermal conductivity, k	0.15	W/m.K
Consistency index, B	3.43	Pa.s
Power law index, n	0.312	
Reference Temperature	3910	
Maximum viscosity limit	2648	
Minimum viscosity limit	33.7	

5.2 Test Case 2: Bay's Fiber Orientation Experiment

Bay [29] conducted injection molding experiments with Zytel 43B which consisted of nylon 6/6 (DuPont Zytel 101L) reinforced with 43wt% glass fibers for a film-gated strip and a center-gated disk. The fiber orientation at several mold locations was measured once the filling process and the subsequent solidification of the suspension melt were complete. The orientation data for the film-gated strip is used for comparison with the numerical results in this research project. The mold geometry is drawn in Figure 5.2 and its dimensions are 203.2mm x 25.4mm x 3.18mm.
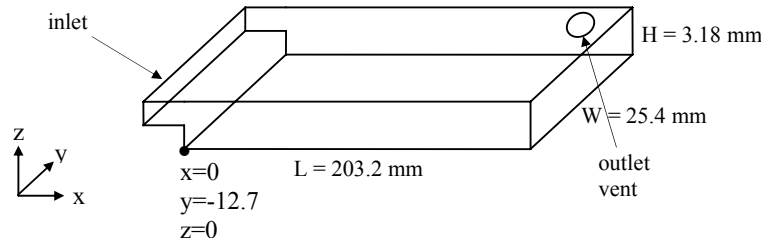
Fig.5.2: Schematic of the film-gated strip (Bay [29])

Bay measured the fiber orientation at 6 points along the mold at various heights and distances from the inlet. Four orientation components were measured; the component along the flow (a_{11}), in the height direction (a_{33}), and in the width direction (a_{22}), as well as the in-plane component (a_{13}). These measurement points lie along the middle plane of the mold and are approximately 9mm, 54mm, 77mm, 96mm, 146mm, and 167mm from the inlet in the length direction.

5.2.1 Simulation Setup

The film – gated strip from Bay's [29] work was simplified by observing that the gate region could be neglected. Due to the fact that the suspension phase is highly viscous, the flow development region is extremely short, thus the vicinity of the gate is important only if the flow behaviour in this area is to be studied. The effect of the gate in the flow simulation has a limited distance of influence from the inlet itself, allowing a mold flow simulation without consideration of the thin-gate. This is demonstrated by scaling arguments in the Appendix A of this report. The presence of the outlet vent shown in the mold geometry of Figure 5.2 serves to vent out air from the mold during the filling process. This maintains the air phase at atmospheric pressure throughout the filling process, and is adequately modeled as a pressure boundary. The simplified computational domain with the gate removed is shown in Figure 5.3.

66
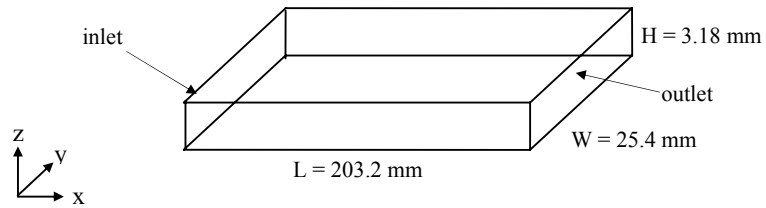
Fig.5.3: Computational domain

As the flow exhibits top-bottom and left-right symmetry, two symmetry boundaries were applied to the geometry which effectively reduces the computational domain to a quarter of the original and consequently the computational cost is reduced. The computational domain, boundaries and location of the symmetry planes are shown in Figure 5.4.
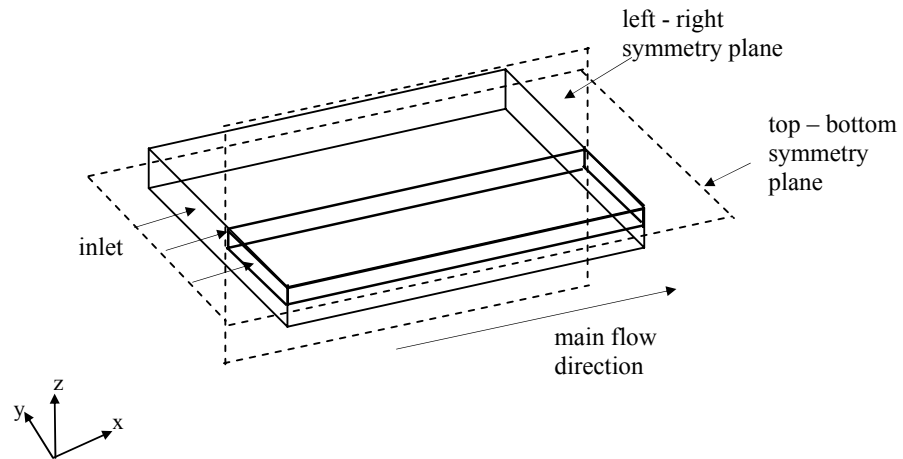
Fig.5.4: The inlet boundary and symmetry planes of the three-dimensional mold. The darkened region is the resulting computational domain.

The three – dimensional mesh was generated in Gambit 2.4 with a variety of grid sizes, and grid independence tests were performed to determine the optimal grid size. This is described later in Chapter 6 of this thesis. The optimal grid sizes are listed in Table 5.2 and Figure 5.5 displays the meshed geometry.

Table 5.2

Optimal grid size of the film-gated strip

Grid	Size
X – direction	0.00048m
Y – direction	0.00048m
Z – direction	0.00016m
Total number of meshes	113778
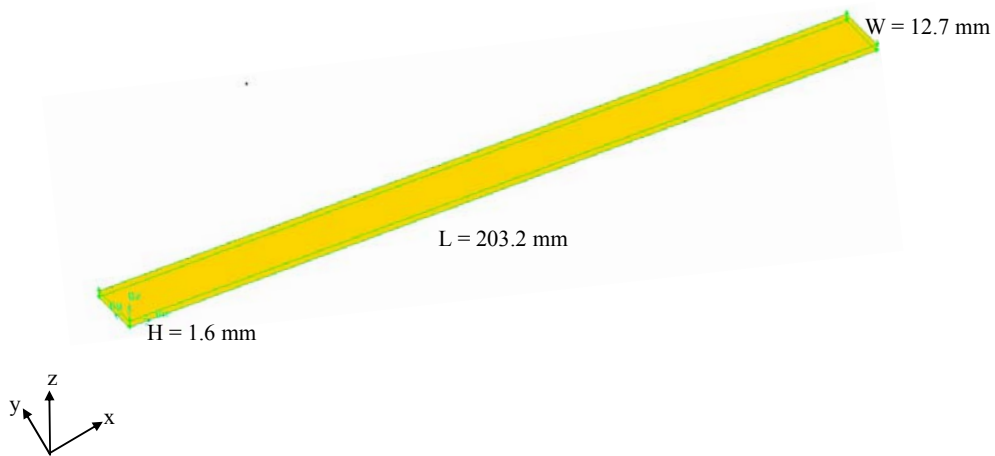
Fig.5.5: Meshed geometry of the mold in Gambit 2.4

A velocity boundary was defined for the mold inlet where the inlet velocity was computed from a recorded filling time of 0.4s [29], and an initial injection pressure was defined as well. In addition, the inlet admits solely the suspension phase into the mold. A pressure boundary was defined for the outlet, and in the event of reversed flow (fluid entering the outlet in the reversed direction to the main flow direction), only air was admitted through this boundary. Further, a temperature was specified for the inlet, outlet (in the event of reversed flow) and the walls. For the initial condition, the volume fraction of the air phase was set to 1 in the whole interior of the mold, mirroring an empty mold at the beginning of the filling process. The boundary and initial conditions are summarized in Table 5.3.

Table 5.3

Boundary and initial conditions

Boundary/ Zone	Boundary /Zone Type	Boundary condition		Initial Condition	
		Parameter	Value	Parameter	Value
Inlet	Velocity inlet	Velocity Magnitude	0.508 m/s	Pressure	0 Pa (gage)
		Suspension Volume Fraction	1		
		Temperature	550 K	Temperature	550K
Outlet	Pressure outlet	Pressure	10^7 Pa (gage)		
		Suspension Volume Fraction	0		
		Reversed Flow Temperature	297K		
Mold interior	Interior			Temperature	297 K
				Suspension volume fraction	0

As mentioned earlier in Chapter 3, the suspension phase is modeled as a non-Newtonian, Power Law fluid. Based upon experiments conducted by Bay [29], the coefficients of the viscosity relation were derived through data-fitting of viscosity values under strain rate and temperature variance. Although the presence and orientation of glass fibers affects the local fluid viscosity, globally, the Power Law viscosity relation adequately represents the bulk viscosity of the mixture. It is treated as such by Bay [21], Chung and Kwon [23, 24, 25] and Verweyst et al. [54], who performed similar analysis with Bay's data set for comparison. Table 5.4 lists the suspension properties.

Table 5.4

Zytel 43B suspension properties

Property	Value	Units
Density ρ	1330	kg/m^3
Specific heat capacity, C_p	1970	J/kg.K
Thermal conductivity, k	0.26	W/m.K
Consistency index, B	1.003×10^{-5}	Pa.s
Power law index, n	0.58	
Reference Temperature	10790	K
Maximum viscosity limit	2648	
Minimum viscosity limit	33.7	

Table 5.5 lists the properties of the air, where the viscosity has been set to 1 Pa.s (the original viscosity of air at 25°C is 1.86×10^{-5} Pa.s) in accordance with the pseudo – concentration method while retaining the other physical properties of air. The dynamic slip model described in Section 3.2.8 is applied here as well.

Table 5.5

Air (pseudo-air) properties

Property	Value	Units
Density ρ	1.225	kg/m^3
Specific heat capacity, C_p	1.003×10^{-3}	J/kg.K
Thermal conductivity, k	0.025	W/m.K
Viscosity	1	Pa.s

5.2.2 Solution Controls

As the flow is time-dependant, the simulation is transient. The total mold-filling time is 0.4s. In order to observe the filling process, data was extracted at the flow time; 0.1s, 0.2s, 0.3s and 0.4s.

An adaptive iteration control was used, where minimum and maximum time steps are specified, and the code is allowed to decide on the change in time step, based upon an evaluation of the Courant number. Relaxation values were used to aid convergence. The iteration parameters are listed in Table 5.6 and the Courant number is defined as:

$$C = U \frac{\Delta t}{\delta x}$$

(87)

Table 5.6

Iteration parameters

Parameter	Value	Units
Minimum time step	0.00001	s
Maximum time step	0.0001	s
Courant number limitation	2	
Flow times	0.1, 0.2,0.3, 0.4	s
Pressure relaxation factor	0.4	
Momentum relaxation factor	0.3	

5.2.3 Grid Independence and the Effect of the Wall Boundary Slip Condition

Grid independence tests were conducted for the simulation of mold – filling flow in order to obtain the optimal mesh size at which further refinement did not produce any significant change in the results. In addition, the effects, if any, of the dynamic slip boundary applied to the wall boundary were studied. An assessment of grid independence was conducted by comparison of the velocity magnitude profiles on 'Plane A', of Figure 5.6 for a halfway filled mold at time t = 0.2s at a distance of 0.00016m from the inlet. Several grids, tabulated in Table 5.7 were examined applying each slip condition.

71

Table 5.7

Computational domain grid sizes

Run number	Slip Condition Tested		Grid Size		
	Dynamic Slip	Traditional No-Slip	X – direction	Y – direction	Z – direction
Run 1	Yes	No	0.00048m	0.00048m	0.00032m
Run 2	Yes	Yes	0.00032m	0.00032m	0.00032m
Run 3	Yes	Yes	0.00032m	0.00032m	0.00016m
Run 4	Yes	Yes	0.00032m	0.00032m	0.00011m
Run 5	Yes	Numerically Unstable	0.00048m	0.00048m	0.00016m
Run 6	No	Yes	0.00024m	0.00024m	0.00016m

5.2.4 Fiber Orientation Evolution

The two – dimensional fiber orientation evolution equation was solved using the flow field data from FLUENT extracted on 'Plane A' as shown in Figure 5.6.   The flow field data was taken from a simulation for a flow time of $t = 0.399$s in order to ensure that the mold was completely filled. The x and z – direction grid sizes correspond with those of the three – dimensional mold – filling simulation. The three closure models were tested; the linear, quadratic and hybrid models and were implemented separately, and the results were compared against Bay's [29] fiber orientation measurements.
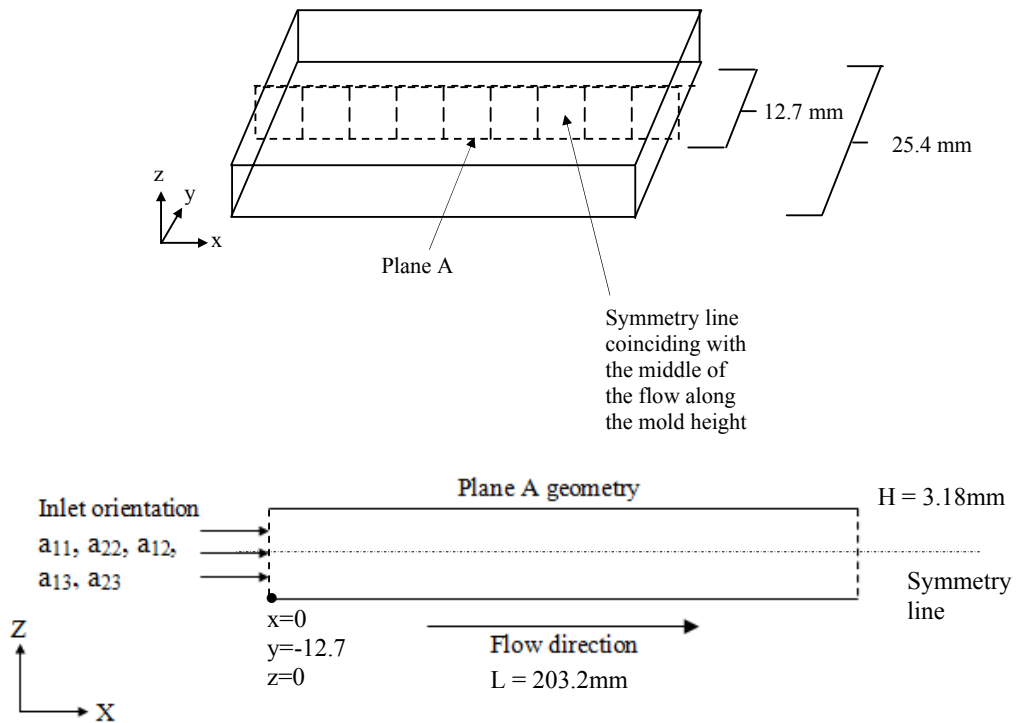
Fig.5.6: 'Plane A': The two – dimensional data extraction plane for the solution of the fiber orientation evolution equation.

The fiber orientation evolution equation is solved over the two-dimensional computational domain subject to a set of initial and boundary conditions. An initial orientation is specified over the entire domain and the inlet boundary carries fixed orientation values for each tensor component. Only the inlet orientation needs to be supplied, and the orientation at the wall and outlet are left to evolve along with the rest of the domain. The boundary and initial conditions sets have identical values and are specified in Table 5.8. They are identical to those that have been employed in Chung and Kwon [24], and match Bay's experimental observations at the mold gate.

Table 5.8

Inlet (Initial) Boundary Condition of each Orientation Tensor Component

Orientation Tensor Component	Value
a_{11}	0.5
a_{22}	0.2
a_{33}	0.3
a_{12}	0
a_{13}	0
a_{23}	0

5.2.5 Fiber Orientation Evolution Solution Controls

As described in Figure 4.11, there are two sets of iteration loops; one is the time-stepping loop and nested inside is the iteration loop of the a_{11}, a_{22}, a_{12}, a_{13} and a_{23} tensor components at a particular time step. The convergence criterion, ε, defined as the difference between the values of two consecutive iterations is used as the measure of convergence of the iteration loop. This is defined as follows:

$$\varepsilon = \frac{\left(a_{ij}\right)_{I,K}^{new} - \left(a_{ij}\right)_{I,K}^{old}}{\left(a_{ij}\right)_{I,K}^{old}} \times 100\%$$

(88.0)

Where a_{ij} is the orientation tensor component at iteration number n, at location (I,K) on the grid.

Further, due to the decoupled approach, the time domain of the fiber orientation evolution equation is distinct and independent of the time domain of the mold-filling flow equations. Thus, there are two different sets of 'times'. It may be mathematically demonstrated that a unique solution exists for the fiber orientation equation for any point in time, solved with the use of the linear, quadratic and hybrid closure [55]. However, this does not guarantee that a steady orientation will be obtained after a sufficiently long time has passed. To circumvent this, a 'steadiness'

74

criteria, S, is used to halt the time-stepping of the discretized fiber orientation equation. Once the difference between the orientation values at two successive time steps falls below preset criteria, a steady orientation state is considered to have been achieved. This is defined in Equation 85.0, and the criterion for each orientation tensor component is listed in Table 5.9. The basis for selecting these criteria were that they were the most stringent possible without causing the time-stepping to go on indefinitely. It was found that very large time-steps (>300) produced completely unrealistic results. A time step size of Δt=0.0001s was found to produce stable iterations.

$$S = \frac{\left(a_{ij}\right)_{I,K}^{n+1} - \left(a_{ij}\right)_{I,K}^{n}}{\left(a_{ij}\right)_{I,K}^{n}} \times 100\,\%$$

(89.0)

Where a_{ij} is the orientation tensor component at time step n, at location (I,K) on the grid. An average relaxation factor was introduced in order to aid the convergence of the fiber orientation evolution equation. This is listed in Table 5.9.

Table 5.9

Solver parameters

Property	Orientation Tensor Component				
	a_{11}	a_{22}	a_{12}	a_{13}	a_{23}
Time step (s)	0.0001	0.0001	0.0001	0.0001	0.0001
Relaxation factor	0.8	0.8	0.8	0.8	0.8
Convergence criteria, ε (%)	0.01	0.01	0.01	0.01	0.01
Steady criteria, S (%)	1	1	5	5	5

5.3 Summary

The validation of the simulation of fiber orientation during mold-filling was carried out in two stages. First a two-dimensional test case from literature [39] was used to validate the simulation setup of the mold-filling flow. The same simulation setup was used to perform a three-dimensional simulation of mold-filling for a geometry corresponding to Bay's [29] work. Grid independence tests were carried out to obtain the optimal mesh size and to study the effects of the dynamic slip condition. A two-dimensional segment of the flow field data was used to solve the fiber orientation. The simulation results for the validation test, three-dimensional mold-filling flow and fiber orientation are presented and discussed in the following chapter.

CHAPTER 6

RESULTS AND DISCUSSION

6.0 Validation of the Mold – Filling Simulation Setup

The results of the simulations for Test Case 1 and Test Case 2 are presented and discussed here. Test Case 1 involved the simulation of the two – dimensional filling of an empty cavity, and the results were used to 'validate' the simulation setup which would be applied to the three – dimensional simulation in Test Case 2. This is presented and discussed in Section 5.1. Section 5.2 discusses the results obtained from Test Case 2 which involved the simulation of the three – dimensional filling of an initially empty mold. Section 5.3 discusses the subsequent computation of the fiber orientation profile along the mold and assessment of closure model performance.

6.1 Validation of the Mold – Filling Simulation Setup

The 'validation' of the mold – filling simulation setup was performed with Test Case 1, where computed velocity and temperature profiles were compared against those obtained by Hieber [39] from a previous simulation. Figures 6.1 and 6.2 show a comparison of the velocity and temperature results between the two simulations.
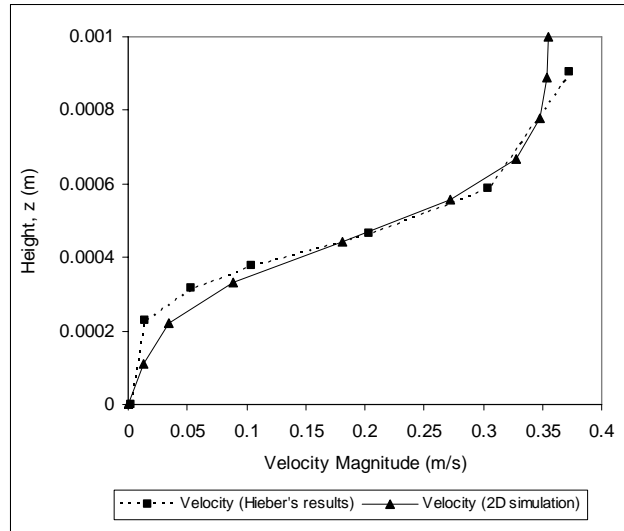
Fig. 6.1: A comparison of velocity data extracted on 'Plane A' after complete filling at a distance 0.1m from the mold inlet
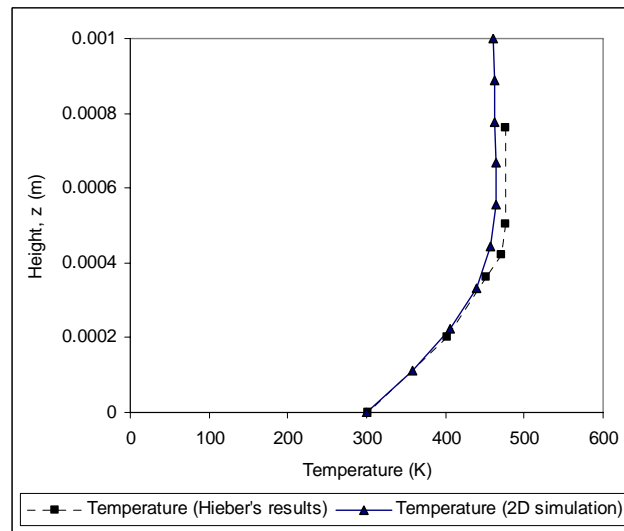
Fig. 6.2: A comparison of temperature data extracted on 'Plane A' after complete filling at a distance 0.1m from the mold inlet

Beginning at the wall, the velocity trends in Figure 6.1 depict a slight deviation between the computed results and those obtained from Hieber's work [39]. After 0.0004m from the wall, and moving towards the middle of the flow, the discrepancy between the two sets of data is diminished with an exception of the last data point. As for temperature, the computed results match Hieber's almost exactly for locations

78

near the wall as shown in Figure 6.2. After 0.0004m from the wall however, a slight deviation develops where the computed results slightly under-predict the temperature of the flow, as compared with Hieber's results. The deviation that appears after this height is of a constant value. This indicates that the simulation setup is capable of accurately predicting velocity and temperature profile of the test case. In addition, this validates the use of the dynamic slip condition in conjunction with the PC method as a viable means of defining the fluid slip at the walls.

6.2 Three – dimensional Mold – Filling Flow

The simulation results of Test Case 2 are presented here. Several flow features of interest were investigated, discussed and qualitatively assessed against experimental and numerical observations from literature. These flow features are: the flow front progression during the mold – filling process, the suspension velocity profiles developed within the mold, fountain flow at the suspension air interface, and grid independence results. In addition the effect of using the dynamic slip boundary as opposed to the traditional no-slip boundary is also investigated.

6.2.1 Data Visualization and Extraction

The flow field data presented here was extracted from the simulation of Test Case 2 along a plane that cuts halfway through the width of the mold. This plane is termed 'Plane A' as depicted in Figure 5.6. This choice was motivated by the fact that the mold height is much smaller when compared to the width and length of the mold, thus the flow gradients are greatest across the mold height and therefore best represent the flow conditions in the mold.

Plane A coincides with the left – right symmetry plane described in Figure 5.4 and is also the plane along which Bay's [29] fiber orientation measurements were made, thus the flow field data on this plane was also used to numerically solve the two – dimensional fiber orientation evolution equation.

As a top – bottom symmetry plane was also employed, as shown in Figure 5.6, the results obtained along Plane A extend from the mold wall to the symmetry line at the middle of the flow.

6.2.2 Grid Independence and the Effect of the Wall Boundary Slip Condition

In order to study grid independence, the velocity magnitude profiles for several grid sizes were compared to observe the size at which the velocities profiles no longer changed, and further refinement would be unnecessary. As the choice of wall boundary slip could conceivably affect the results, comparisons were performed for both the dynamic slip and traditional no – slip boundaries. The grid sizes and details of each run are listed in Table 5.7. Simulations performed for the dynamic slip condition are denoted with the term 'dyn' added to the run number, i.e. 'Run # dyn', and those with the traditional no-slip condition are identified by an addition of 'no-slip' after the run number, i.e. 'Run # no-slip'.

Not all the runs successfully produced results however, as stability issues were encountered for 'Run 5 no-slip'. This was attributed to the numerical instability introduced by grids with significant aspect (length to height) ratios (X/Z = 3) whilst applying the no-slip condition universally, as defined by Fluent.

Two runs; 'Run 1 no-slip' and 'Run 6 dyn' were not performed. It was reasoned from the results obtained on the other runs, that for 'Run 1 no-slip', further coarsening would not resolve the problem of a skewed interface described later. In like manner, from the grid independence results for the grids using the dynamic slip boundary, it was observed that further refinement of the grid, 'Run 6 dyn' was unnecessary.

A comparison of the velocity magnitude profiles for the dynamic slip case is made first. Figure 6.3 presents velocity magnitude data extracted for 'Run 1 dyn' through 'Run 5 dyn'. As may be observed in Figure 6.3, the data are clustered into two groups based on their trends: 'Run 1 dyn' and 'Run 2 dyn' tend to group, whilst 'Run 3 dyn', 'Run 4 dyn' and 'Run 5 dyn' form another. Runs of the two different trends are separated in Figures 6.4 and 6.5. An analysis of 'Run 1 dyn' and 'Run 2 dyn' in Figure 6.4 demonstrates a profile that is almost linear between the heights of 0m and 0.0009m from the wall. Progressing from 'Run 3 dyn' through 'Run 5 dyn' the velocity trends between these two points on the mold interior begin to exhibit a non-parabolic profile as observed in Figure 6.5, where the velocity gradients in the near wall region (less than 0.0004m from the wall) are reduced. However, near the flow core (0.01 to 0.016m from the mold wall), the velocity trends for all the runs begin to converge together as seen in Figure 6.3. Due to the imposition of fluid continuity, this results in a speeding up of the fluid between the heights of 0.0004m to 0.001m from the mold wall. It should be noted as well, that the grids used for 'Run 3 dyn', 'Run 4 dyn' and 'Run 5 dyn' have smaller mesh sizes in the height direction as compared to 'Run 1 dyn' and 'Run 2 dyn'.

Fig. 6.3: Velocity magnitude data on 'Plane A' for 'Run 1 dyn' to 'Run 5 dyn', taken at time t = 0.2s at a distance 0.06m from the mold inlet.
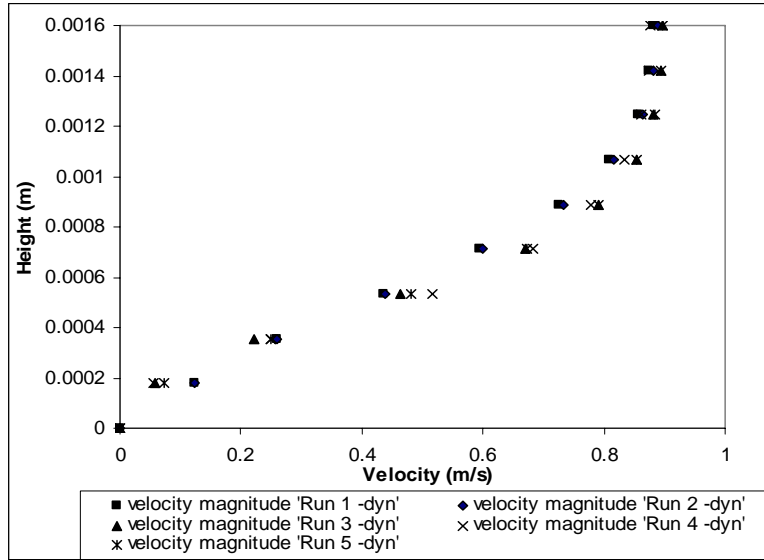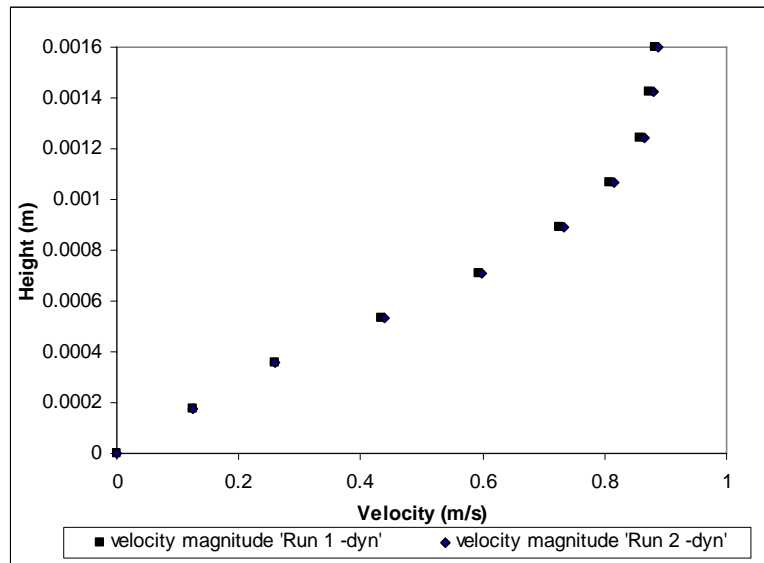

Fig. 6.4: Velocity magnitude data on 'Plane A' for 'Run1 dyn' and 'Run 2 dyn', taken at time t = 0.2s at a distance 0.06m from the mold inlet.

The effect of grid refinement in the height (z) direction may be clearly seen when the velocity trends in Figure 6.4 and 6.5 are compared. The trends in Figure 6.4 are closely clustered, where both grids have a grid size of 0.00032m in the height

(z) direction, but different grid sizes in the length (x) and width (y). This demonstrates that the grid refinement in the length (x) and width (y) directions yields little effect. Refinement in the height (z) direction produces noticeable effects, as demonstrated in Figure 6.5. This is readily explained by the fact that the largest fluid gradients occur across the mold height, as it is the shortest dimension in comparison to the mold length and width, thus refinement in the height direction captures these gradients better.
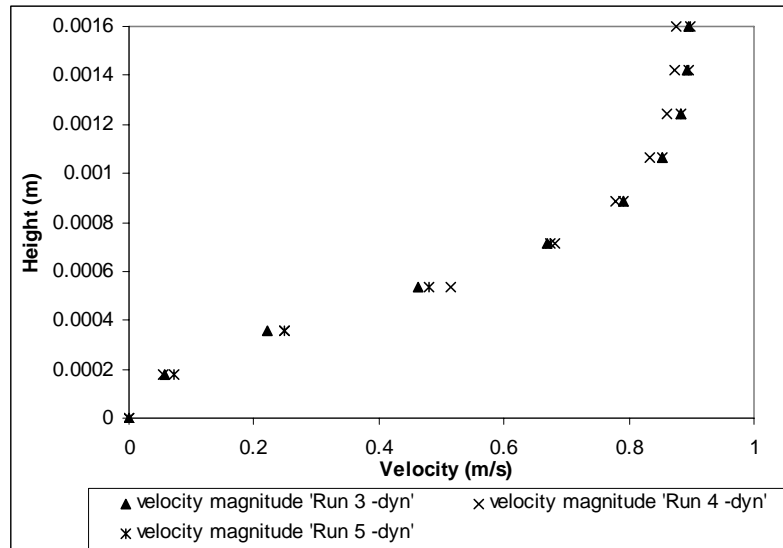

Fig. 6.5: Velocity magnitude data extracted on 'Plane A' for 'Run 3 dyn', 'Run 4 dyn' and 'Run 5 dyn', taken at time t = 0.2s at a distance 0.06m from the mold inlet.

It may be seen from further analysis of Figure 6.5 that the velocity magnitude profiles are clustered together for most of the points, with differences between the two sets of results pronounced near the wall (less than 0.06m from the wall). These differences are small however, in comparison to the velocity magnitude itself – less than 10% deviation between 'Run 3 dyn', 'Run 4 dyn' and 'Run 5 dyn' results. Following this, it is understood that the finer grids in Run 3 and Run 4 do not show a considerable difference in the simulated results. Therefore, 'Run 5 dyn' gives a grid independent solution.

Identical simulations were performed for several runs (termed 'Run # no-slip') with the traditional no-slip boundary conditions applied to both phases as listed in Table 5.7. With the exception of 'Run 6 no-slip', the results produced demonstrated

a highly stretched interface which was physically unrealistic. 'Run 5 no-slip' was found to be unstable even for very small time steps (Courant number = 0.25). An example of the stretched interface taken from 'Run 3 no-slip' is shown in Figure 6.6.

Fig. 6.6: Fluid phase profile extracted on 'Plane A' for 'Run 3 no-slip', taken at time t = 0.2s. The red phase is the polymer, and the blue one is pseudo-air.

For contrast, Figure 6.7 shows a fluid phase profile from 'Run 5 dyn'. As may be observed, the interface is a rounded quarter circle, which is in agreement with results obtained by others [56, 57].
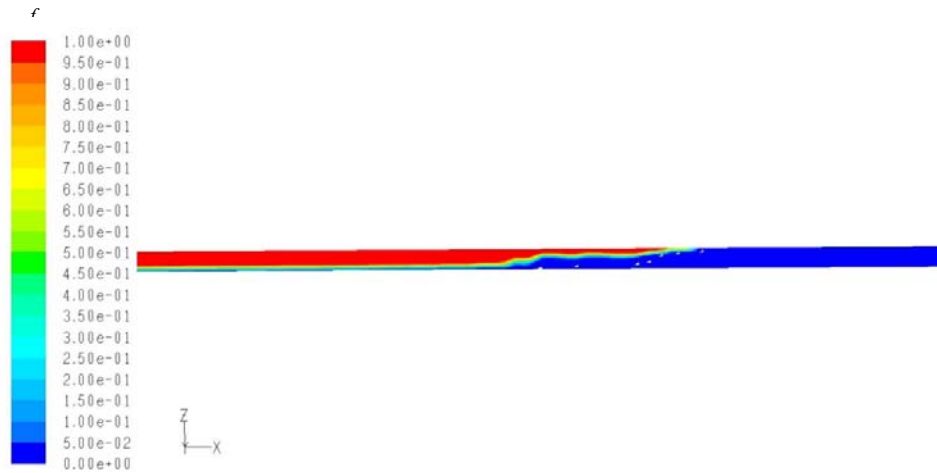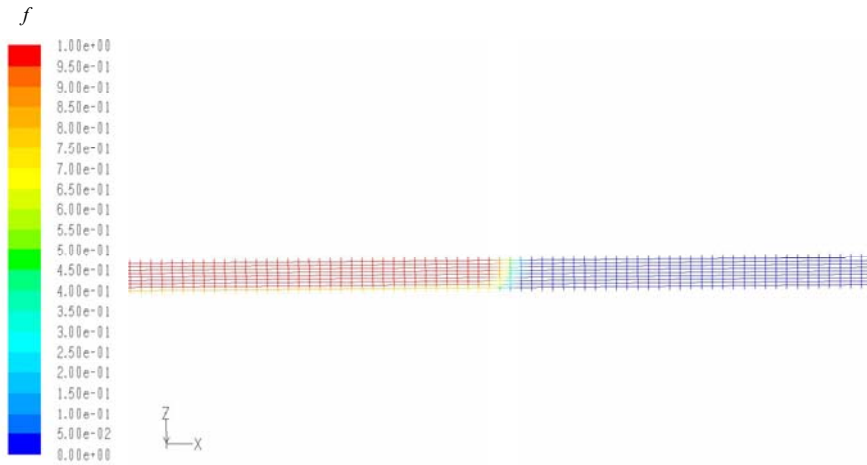
Fig. 6.7: Fluid phase profile extracted on 'Plane A' for 'Run 5 dyn', taken at time t = 0.1s. The red phase is the polymer, and the blue one is pseudo-air.

The simulation with 'Run 6 no-slip' produced results with a reasonable interface shape and location; the velocity magnitude results were very close to those obtained on 'Run 5 dyn', as shown in Figure 6.8.
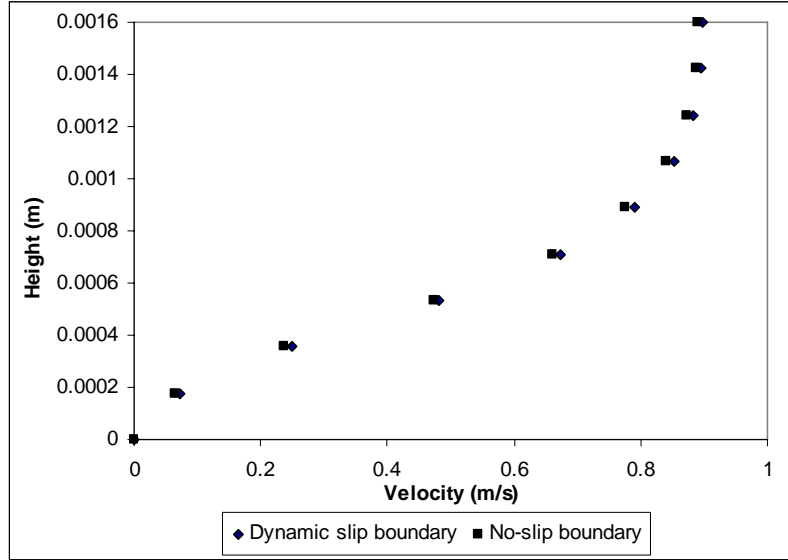
Fig. 6.8: A comparison of the velocity magnitudes on 'Plane A' for 'Run 5 dyn' and 'Run 6 no-slip' taken at time t = 0.2s at a distance of 0.06m from the mold inlet.

A plausible reason for the stretched interface observed in Figure 6.6 and the improvement in the quality of results (with reference to 'Run 2 dyn' and 'Run 5 dyn') may be elaborated here. FLUENT defines the no-slip boundary by specifying a large wall shear stress of order 10^9 Pa at the wall boundary, resulting in large velocity gradients across the height direction in cells near the wall. When the meshes used have a large aspect (length to height) ratio, the area of the cell face across the height is larger than that across the length leading to comparably higher convection through the height direction of the cell. Considering the volume fraction of cells near the wall, increased convection through the height direction leads to the movement of polymer away from the walls resulting in a higher proportion of air filled cells. Due to the conservation of polymer mass, this leads to a commensurate convection of polymer along the flow direction from cells in the middle of the flow, the net effect of which is the skewed interface observed in Figure 6.6. The grid used in 'Run 6 no-slip' has a small aspect ratio of 1.5 and thus a smaller difference in the face areas of the cell. This balances out the convection across the height and along the length of the cell resulting in a more balanced distribution of polymer (and air), thus a more gradual, curved interface is observed. Due to the similarity in the velocity

86

magnitudes trends shown in Figure 6.8, it is considered that 'Run 6 no-slip' produces grid independent results for the traditional slip cases. However, it should be pointed out that the grid 'Run 6 no-slip' has four times as many meshes as 'Run 5 dyn' for similar quality of results. Thus there is a considerable increase in computational resources required in the earlier case as opposed to the latter one.

Due to the fact that the velocity profiles from 'Run 5 dyn' demonstrate grid independence, the remainder of the flow field data presented in this thesis is derived from 'Run 5 dyn'. In addition, the velocity and strain rate data used to solve the fiber orientation evolution equation was derived from this particular simulation run as well.

6.2.3 Suspension – Air Interface Progression

As the inlet velocity used in this simulation was estimated from the actual filling time of the mold, the interface progression should agree with the elapsed flow time. The interface at various times; 0.1s, 0.2s, 0.3s and 0.39s should be at the approximate locations at the corresponding times, as tabulated in Table 6.1:

Table 6.1

Interface location at corresponding flow times

Flow Time	Interface location (distance from mold inlet)
0.1 s	0.05m
0.2 s	0.1m
0.3 s	0.155m
0.39 s	0.19m

Figure 6.9 shows the volume fraction plots of the mold at the corresponding times as those in Table 6.1, viewed from above. The red phase is the suspension, the blue phase is the pseudo-air and the light green band represents the interface.

The plots show that the interface locations correspond to the filling times that would be expected during the actual filling process. In addition, the interface shape viewed from above demonstrates a curvature that extends from the wall to the

symmetry plane. This is expected, and is in keeping with the no-slip condition applied to the suspension phase at wall.
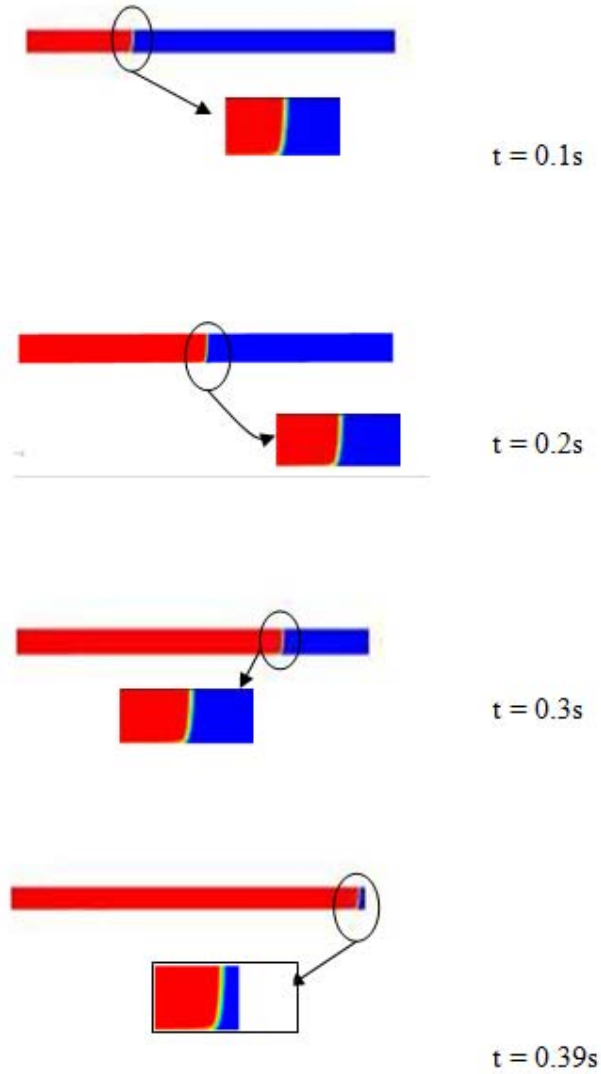

$t = 0.1s$

$t = 0.2s$

$t = 0.3s$

$t = 0.39s$

Fig. 6.9: Volume fraction plots of mold geometry viewed from above at times 0.1s, 0.2s, 0.3s and 0.39s

6.2.4 Suspension Velocity

Velocity profiles across the mold height were obtained at various points along 'Plane A', at four different flow times: 0.1, 0.2, 0.3 and 0.39s in order to observe the velocity field development as the filling process occurs. A sampling of these data at a distance of 0.04m from the mold inlet are presented at the four different times, in Figures 6.10 through 5.13. It was observed that running the simulation for a full 0.4s resulted in the suspension 'over-flowing' the pressure outlet boundary, thus only values close to 0.4s were used. The flow field for which the fiber orientation is computed was obtained at flow time t = 0.399s. A general picture of the velocity profile within the mold may be gleaned from Figure 6.10 through Figure 6.13 where it may be observed that the velocity profile changes gradually with respect to time especially near the wall. As may be seen, the shape of the profile does not approach the parabolic curve typical of Newtonian flows. Rather, it features a sharp increase in velocity near the wall which corresponds with the viscous and thermal boundary layer occurring there. The viscous boundary layer occurs due to the effect of zero slippage at the wall, and in conjunction with the rapid decrease in temperature near the wall, the viscosity of the polymer increases dramatically, slowing the fluid down further. This classic 'nipple' shape conforms to the velocity profile observed in typical mold filling flows [56]. It illustrates the importance of using a Non-Newtonian formulation for the viscosity that allows for variation with respect to local fluid strain rates and temperature.

Fig. 6.10: Velocity Components vs. mold height, 'Plane A' at x =0.04m, t = 0.1s

Fig. 6.11: Velocity Components vs. mold height, 'Plane A' at x =0.04m, t = 0.2s
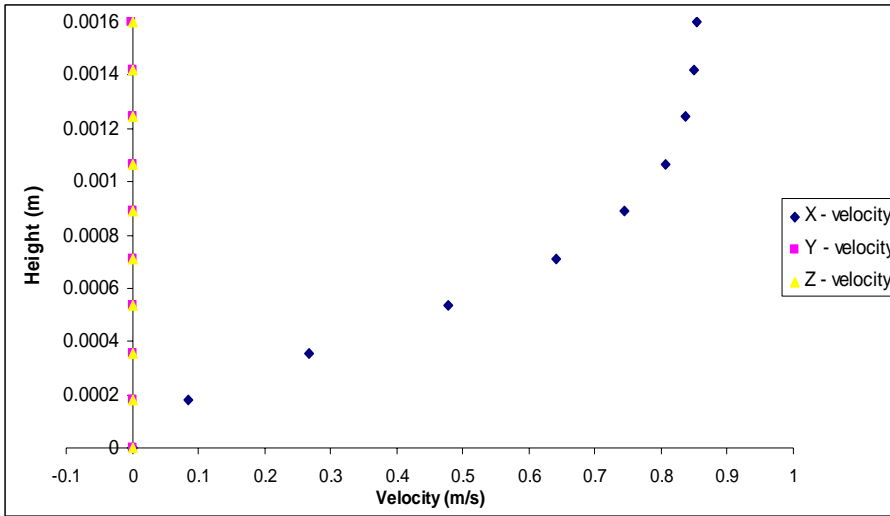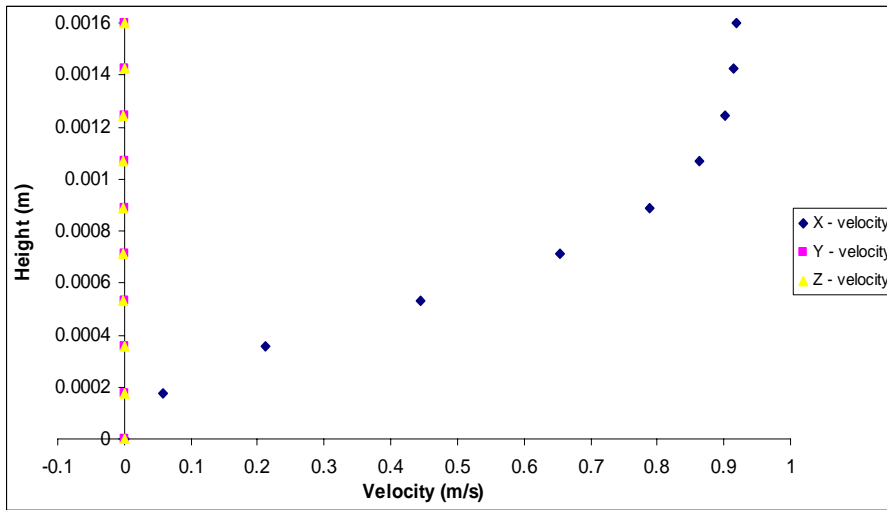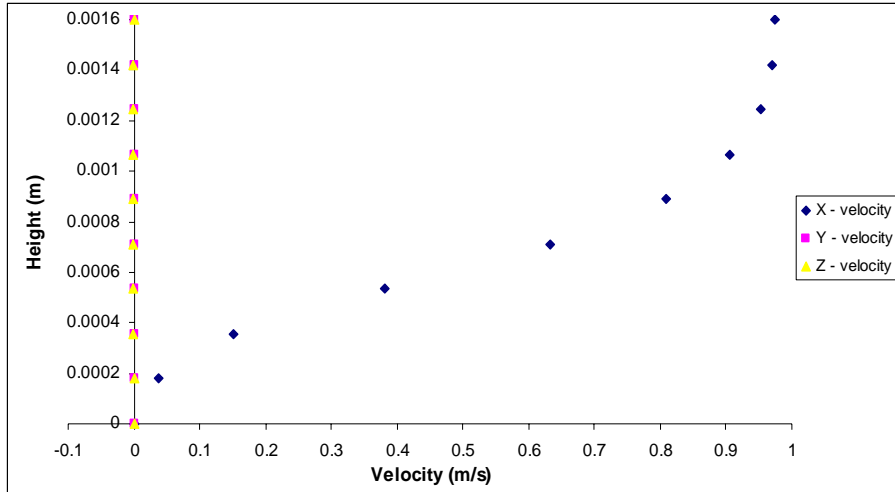
Fig. 6.12: Velocity Components vs. mold height, 'Plane A' at x =0.04m, t = 0.3s
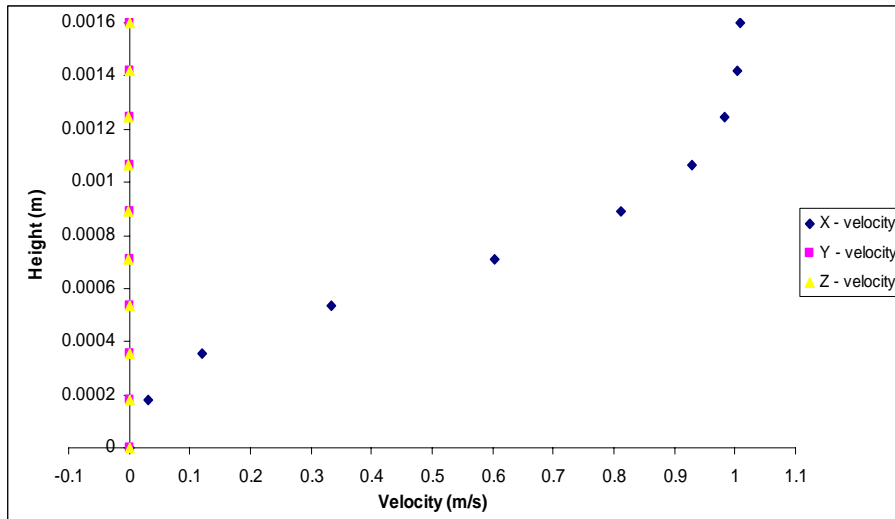
Fig. 6.13: Velocity Components vs. mold height, 'Plane A' at x =0.04m, t = 0.39s

6.2.5 Fountain Flow

The phenomenon of fountain flow has been described in the introduction of this report, and the necessity of a complete three-dimensional simulation to capture this effect has been clarified. The occurrence of fountain flow in the simulations carried out is visualized by velocity vectors. A view of this is presented in Figure 6.14. The vectors are coloured according to the phase present: red for suspension and blue for air, colours in between represent a mixture of suspension and air. The vector lengths correspond to the velocity magnitude, and the direction of the vectors indicates the predominant direction of the velocity.
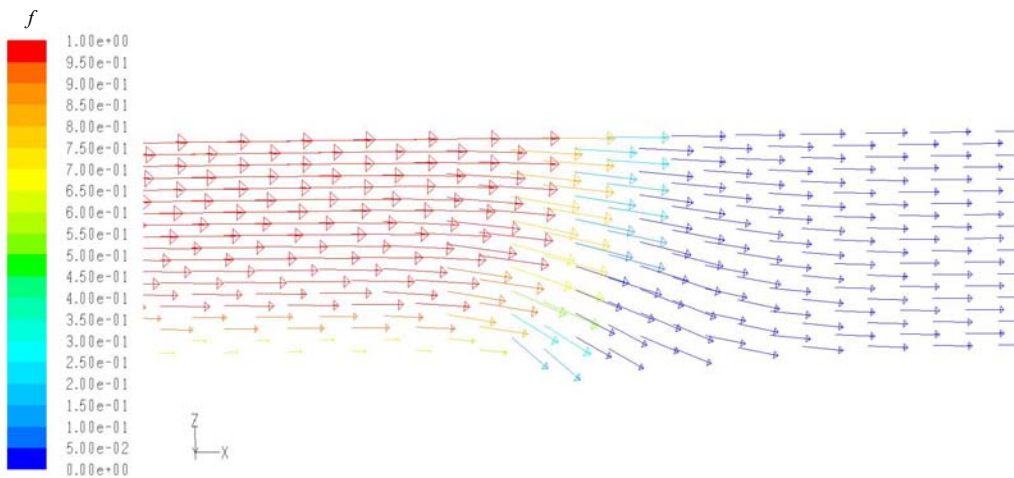
Fig. 6.14: Velocity vectors on 'Plane A' at location x = 0.1m, flow time, t = 0.2s

At the interface, the suspension velocity vectors are directed away from the predominant flow direction and towards the mold wall. This is caused by the bulk flow decelerating at the suspension – air interface due to the curvature of the interface itself. A similar result was obtained by Chang and Yang [57], where they noted that this effect may only be captured with a full three-dimensional simulation, without the use of any mathematical simplifications such as the Hele-Shaw method [38]. This naturally has an effect on the fiber orientation near the interface, thus

92

capturing this flow feature is necessary in order to permit an accurate simulation of the fiber orientation during mold-filling flow.

6.3 Fiber Orientation Calculation

The two – dimensional fiber orientation evolution equation was solved using the velocity and strain rate data extracted on Plane A as the coefficients of the orientation tensors. As shown in Figure 5.6, the symmetry line extends through the middle of the flow along the mold height, thus, due to the fact that the symmetry boundary is employed for the solution domain of the fiber orientation evolution, the simulation results produced extend from the mold wall to the mid-plane of the domain (0m to 0.0016m). Bay's [29] data consists of fiber orientation measurements that extend the entire mold height, from 0m to 0.0032m. Due to this disparity, the numerical data is 'mirrored' across the symmetry plane in order to allow for a comparison with the full set of experimental data.   The experimental data used for the analysis is tabulated in Appendix D, where the magnitude for each orientation component is listed together with the error range of each measurement. In order to allow for a comparison, the experimental data used consists of the average orientation values measured at each data sampling point. In addition, the experimental data sampling points do not match the simulation grid points, thus linear interpolation is applied where necessary to the numerical data in order to facilitate a point by point analysis.

The data comparison between the numerical and experimental sets is organized on the basis of the closure model used. Three closure models are employed (linear, quadratic and hybrid), with four orientation tensor components of interest (a_{11}, a_{22}, a_{33} and a_{13}), at six measurement locations (9, 54, 77, 96, 146, and 167mm from the mold inlet).

Simulations with each closure model met the halting or 'steadiness' criteria listed in Table 5.9, and for each time step, a converged solution was typically achieved within eight iterations. However, there were halting issues with the a_{13} and a_{23} components for the linear and the a_{12} and a_{23} components for the hybrid closure which did not resolve with further time-stepping. Thus for these two closure models,

only three of the five steady criteria were met. Plots of a_{13}, a_{23} and a_{23} values against iteration time-steps at several locations within the mold, for the linear and hybrid closure model are provided in the Appendix C section of this report. It was observed that the bulk of the data trends demonstrated steady values when the time-stepping was terminated, and that the inability to meet the steady criteria was due to the skew introduced by several data points. Taking this into account, the steady solution for the simulation utilizing the linear closure was obtained at 157 time-steps or corresponding to a real time of 0.0157s. The simulation with the quadratic closure steadied at 103 time steps or 0.0103s, and the one with the hybrid closure attained steadiness at 152 time steps or 0.0152s.

6.3.1 Fiber Orientation Profiles

Due to the sheer volume of data generated by the simulation; four orientation components by three closure models at six locations within the mold, a composite image of the orientation data along the mold superposed over the mold geometry for each closure model is presented here. The composite images afford an overall view of the fiber orientation along the mold, and allow for qualitative descriptions of the closure model performance at various locations along the mold. The individual fiber orientation profiles for each orientation component are attached in Appendix H (linear closure), I (quadratic closure) and J (hybrid closure) of this thesis and allow for a closer observation of the numerically predicted fiber orientation values against the experimental data.

The composite images in Figures 6.15 through 6.26 are arranged in order of orientation components as follows: a_{11}, a_{22}, a_{33} and a_{13}. Figures 6.15 through 6.18 present the data obtained for the linear closure, Figures 6.19 through 6.22 present the data for the quadratic closure and Figures 6.23 through 6.26 present the data for the hybrid closure model.

Fig. 6.15: a_{11} orientation tensors computed along the mold length at several locations using the linear closure model. The solid lines represent the numerical data and the dots are the experimental data. (The mold length to height ratio is not to scale)

Fig. 6.16: a_{22} orientation tensors computed along the mold length at several locations using the linear closure model. The solid lines represent the numerical data and the dots are the experimental data. (The mold length to height ratio is not to scale)

Fig. 6.17: a_{33} orientation tensors computed along the mold length at several locations using the linear closure. The solid lines represent the numerical data and the dots are the experimental data. (The mold length to height ratio is not to scale)

Fig. 6.18: a_{13} orientation tensors computed along the mold length at several locations using the linear closure. The solid lines represent the numerical data and the dots are the experimental data. (The mold length to height ratio is not to scale)

Fig. 6.19: a_{11} orientation tensors computed along the mold length at several locations using the quadratic closure model. The solid lines represent the numerical data and the dots are the experimental data. (The mold length to height ratio is not to scale)

Fig. 6.20: a_{22} orientation tensors computed along the mold length at several locations using the quadratic closure model. The solid lines represent the numerical data and the dots are the experimental data. (The mold length to height ratio is not to scale)

Fig. 6.21: a_{33} orientation tensors computed along the mold length at several locations using the quadratic closure model. The solid lines represent the numerical data and the dots are the experimental data. (The mold length to height ratio is not to scale)

Fig. 6.22: a_{13} orientation tensors computed along the mold length at several locations using the quadratic closure model. The solid lines represent the numerical data and the dots are the experimental data. (The mold length to height ratio is not to scale)

Fig. 6.23: a_{11} orientation tensors computed along the mold length at several locations using the hybrid closure model. The solid lines represent the numerical data and the dots are the experimental data. (The mold length to height ratio is not to scale)

Fig. 6.24: a_{22} orientation tensors computed along the mold length at several locations using the hybrid closure model. The solid lines represent the numerical data and the dots are the experimental data. (The mold length to height ratio is not to scale)

Fig. 6.25: a_{33} orientation tensors computed along the mold length at several locations using the hybrid closure model. The solid lines represent the numerical data and the dots are the experimental data. (The mold length to height ratio is not to scale)

Fig. 6.26: a_{13} orientation tensors computed along the mold length at several locations using the hybrid closure model. The solid lines represent the numerical data and the dots are the experimental data. (The mold length to height ratio is not to scale)

6.3.2 Fiber Orientation Profile Analysis

A brief idea of the fiber orientation profile may be gleaned from a simple consideration of the fluid shear within the mold. The mold geometry has a large length-to-height ratio, resulting in flow that exhibits considerable shear and may be termed a shear dominated flow. It is a well understood process that short fibers in a flow tend to orient in the direction of fluid strain [1, 31]. When the predominant strain rates occur in the flow direction, it may then be argued that the most significant change in the orientation tensor will occur in the flow direction. The exception to this will occur near the middle of the flow where fluid stretching tends to dominate leading to orientation transverse to the flow direction. In the case under study here, the orientation tensor component directed along the flow is the a_{11} tensor, and as may be observed in the experimental data trends of Figures 6.15, 6.19 and 6.23 this is indeed the predominant orientation tensor component as it is the largest in magnitude. In addition, due to the fact that the numerical solution of the evolution equation of the 5 independent tensor components proceeds sequentially (in the following order: a_{11}, a_{22}, a_{12}, a_{13} then a_{23}), an accurate prediction of the a_{11} component is necessary in order to ensure the accurate prediction of the others.

Therefore, this indicates that the a_{11} tensor is the primary component of interest in the simulation utilizing the current mold geometry, and it should be the key indicator in assessing the performance of the closure models.

6.3.2.1 Symmetry Analysis

The computed orientation profiles observed in Figures 6.15 through 6.17, Figures 6.19 through 6.21 and Figures 6.23 through 6.25 corresponding to the a_{11}, a_{22} and a_{33} orientations demonstrate symmetry about the mold height of 0.0016m, and the numerical trends in Figures 6.18, 6.22 and 6.26 corresponding to a_{13} orientation demonstrate anti-symmetry. This is the consequence of imposing the symmetry boundary condition through the mid-plane of the mold. The experimental a_{11}, a_{22}, a_{33} and a_{13} trends qualitatively demonstrate this behaviour, however, there are quantitative differences in the orientation values across the mold height of 0.0016m. This may be readily confirmed in closer detail by studying the orientation plots in

Appendix H, I and J of this thesis. Neglecting post-filling effects, this behaviour may be best accounted for by the occurrence of anisotropic fiber-fiber interactions which are not accounted for by the Folgar-Tucker model [36] used in this work. Thus further research in this direction is necessary in order to develop models that account for interaction anisotropy. Nevertheless, it should be noted that the implementation of an anisotropic model would immediately invalidate the mathematical symmetry of the fiber orientation evolution equation and the mold-filling flow, thus requiring a numerical solution with the entire mold geometry.

6.3.2.2 a_{11} Orientation Component

The computed a_{11} orientation profiles in Figures 6.15, 6.19 and 6.23 generally demonstrate qualitative agreement with the experimental trends and this is most pronounced at locations 54, 96 and 170 mm from the mold inlet. This may be confirmed quantitatively by the orientation plots in Appendix H, I and J. The experimental trends tend to follow a profile where the a_{11} magnitude at the wall is low, then it increases some distance away to a maximum, and then drops off towards the middle of the flow. A commensurate increase in the magnitude of a_{22} and a_{33} may be observed in Figures 6.16, 6.20 and 6.24 and Figures 6.17, 6.21 and 6.25. This coheres well with the received view of the 5 layer orientation profile described earlier. The layer immediately adjacent to the wall corresponds with the 'skin' layer, the 'shell' layer is encountered next where the maximum alignment of the fibers in the flow direction (maximum a_{11}). Last, near the middle of the flow the 'core' layer is observed, where the orientation in the flow direction reduces (a_{11} decreases). This trend is captured well by all three closure models; however, there is a tendency in all of them to under-predict the a_{11} orientation near the flow core (0.001 to 0.0016m along the mold height) and in the skin layer (0 to 0.0002m and 0.003 to 0.0032m along the mold height).

6.3.2.3   Non – dominant Orientation Components

Both experimental and numerical a_{22} and a_{33} values are significantly smaller than a_{11} as may be observed in Figures 6.16, 6.20 and 6.24 and Figures 6.17, 6.21 and 6.25, even in regions near the middle of the flow where fluid stretching should be dominant. Generally, all three closure models demonstrate an over-prediction of a_{33} in the core region (0.001 to 0.0016 m along the mold height) and at the skin layer (0 to 0.0002m and 0.003 to 0.0032m along the mold height) as shown in Figures 6.17, 6.21 and 6.25. These findings may be confirmed in closer detail with reference to the figures in Appendix H, I and J of this thesis.

The a_{13} component is also qualitatively predicted by the quadratic and hybrid closure as seen in Figures 6.22 and 6.26, and especially well by the linear closure, where the trend of numerical data closely follows the experimental data, as seen in Figure 6.18.

6.3.3 Closure Model Performance Comparison

The deviation between the experiment and numerical results was used to assess the prediction capabilities of each closure model. The normalized root-mean-square of the deviation (NRMSD) between the two sets of data was computed using the following formulation:

$$NRMSD = \frac{\sqrt{\left.\sum_{n=1}^{N}\left({a_{ij}^{num}}_n - {a_{ij}^{exp}}_n\right)^2 \middle/ N\right.}}{{a_{ij}^{exp}}_{max} - {a_{ij}^{exp}}_{min}} \times 100\% \qquad (90)$$

where a_{ij}^{exp} is the measured orientation component magnitude at a particular mold location and height and a_{ij}^{num} is the orientation tensor component obtained by numerical simulation at the corresponding point. N is the total number of points along the mold height at a given mold distance from the inlet. ${a_{ij}^{exp}}_{max}$ refers to the global maximum a_{ij} and ${a_{ij}^{exp}}_{min}$ refers to the global minimum a_{ij} experimental

values. Thus the NRMSD is used as a measure of deviation for each tensor component. Given the fact that the experimental measurements are taken at 6 locations in the mold at several different heights, the average deviation may be computed for each location. Table 6.2 lists the average deviation for each tensor component at each mold location for each closure model. The NRMSD calculations at each location are tabulated for each closure model in Appendix E, F and G.

Table 6.2

Average deviation of each tensor component

Closure Model		Orientation Tensor Component	Mold location (distance from the inlet) (mm)					
			9	54	77	96	146	170
NRMSD (%)	Linear	a_{11}	34.79	31.87	44.34	42.41	48.87	36.35
		a_{22}	29.35	31.41	31.17	30.39	33.17	31.48
		a_{33}	33.66	27.10	31.32	32.14	30.69	28.36
		a_{13}	24.95	11.39	9.36	12.66	12.40	11.49
	Quadratic	a_{11}	43.38	30.39	42.16	39.53	45.1	31.94
		a_{22}	24.98	28.10	27.37	26.42	29.20	28.11
		a_{33}	38.03	27.16	29.41	30.61	29.59	27.53
		a_{13}	27.90	22.94	23.10	28.55	32.34	26.33
	Hybrid	a_{11}	56.11	32.07	43.30	40.55	46.01	34.11
		a_{22}	29.65	25.95	22.14	20.75	23.12	24.50
		a_{33}	44.15	32.87	35.32	35.99	35.40	32.99
		a_{13}	42.28	44.76	43.78	35.51	38.85	43.69

A profile of the average deviation at each grid location for each closure model may be used to observe the change in deviation as we proceed downstream from the inlet, and to compare the performance of each closure model. Figure 6.27 through Figure 6.30 plots the average deviation profile for the orientation tensor components in the following order: a_{11}, a_{22}, a_{33} and a_{13}.

As has been argued earlier, the a_{11} tensor is the dominant orientation tensor and from Figure 6.27 it is clear that the numerically computed values are in agreement with the experimental data and that the trends of deviation are identical for each closure model. As mentioned earlier, an inspection of the a_{11} plots for each closure

model generally shows that best agreement between numerical and experimental trends occurs at 54, 96 and 170 mm from the mold inlet. This is borne out by the profile in Figure 6.27, where the deviation at these locations is less than 45% for all the closures. The agreement between the two sets of data is best at the shell region of the flow (0.0002 to 0.001m and 0.0022 to 0.003m along the mold height) as observed in Figures 6.15, 6.19 and 6.23. This observation may be confirmed in closer detail with reference to the a_{11} orientation plots in Appendix H, I and J of this thesis. With the exception of the orientation results 9mm from the inlet, it is clear that the quadratic closure produces the most accurate prediction as the average deviation is the lowest of all three closure models. The hybrid closure is only slightly worse. As described in the introduction of this work, the quadratic closure is exact for aligned orientation. The mold-filling flow encountered in this work has strong bulk shearing characteristics (with exception of the core and skin layer), thus a closure model that performs well where the fiber orientation is predominantly in a single direction, would be expected to produce the best results. This is in fact observed with the quadratic closure.

The orientation results measured at the location of 9mm from the inlet are close enough to encounter the near-gate effects, resulting in a more randomized orientation due to significant fluid convection. Here the linear closure performs better than the others, as the a_{11} orientation results are predicted with better accuracy as compared to the quadratic and hybrid closure. As described in Chapter 1, the linear closure model is exact for completely random in space fiber orientation, thus, this explains why the a_{11} values are best predicted by the linear closure in the near gate region.

The deviation between numerical and experimental data of all three closure models is reduced where the prediction of the a_{22} component is concerned as seen in Figure 6.28. The difference between the numerical and experimental data is less significant here than for the a_{11} component. The linear and quadratic closures demonstrate similar qualitative trends; however, the hybrid closure performs better than either the linear or quadratic closures as the trend consistently shows the least deviation from the experimental results. It may be observed from Figures 6.16 and 6.20 that the closest agreement between the numerical and experimental data for the linear and quadratic trends occurs in the shell region (0.0002 to 0.001m and 0.0022

111

to 0.003m). For the hybrid closure shown in Figure 6.24 however, the numerical results in the shell zone demonstrate a consistent under-prediction of the a_{22} orientation which is best explained by the over prediction of the a_{11} orientation component.

The deviation of the a_{33} orientation component is of the same order of magnitude as that of the a_{11} orientation, however for this component, the hybrid closure performs worse than either the linear or quadratic closure models. In a manner similar to the a_{11} trend, the deviation trends of the a_{22} component for both the linear and quadratic closure are very close together. For all three closure models, the closest agreement between the numerical and experimental trends is observed in the shell region (0.0002 to 0.001m and 0.0022 to 0.003m) of the flow.

For the a_{13} orientation component, the trends in Figure 6.30 demonstrate that the difference between the numerical and experimental data is highest for the hybrid closure followed by the quadratic and linear closure. In contrast to Figures 6.27 through 5.29, it may be observed that the deviation trends produced by each of the closure models are considerably different from one another. In addition, the deviation trends are spread over a broader range as compared to those of the other orientation components. From Figure 6.30, it is apparent that the linear closure predicts the a_{13} orientation with the least deviation from experiment.

An assessment of the closure model performance in terms of the deviation from the experimental results may thus be made. Comparing the linear, quadratic and hybrid model performance against the experimental data reveals that for the a_{11} the deviation profiles of all three closures are similar and are relatively close to one another. However, the linear closure performs better in the near-gate region. For the a_{22} orientation component, the deviation profiles of all three closures are confined to a small range of about 20 to 35% from experiment and demonstrate the same qualitative trend. Similarly for the a_{33} component, with the exception of the near-gate region, the deviation trends of all three closures fall within a range of about 25 to 36% and are thus close to one another. For the a_{13} component however, it is clear that the linear closure outperforms the other two closure models considerably as the deviation in the numerical data produced by the linear closure is considerably

112

smaller as compared to the quadratic and hybrid closure. Thus, from this analysis it is concluded that the linear closure exhibits the best all – round performance.
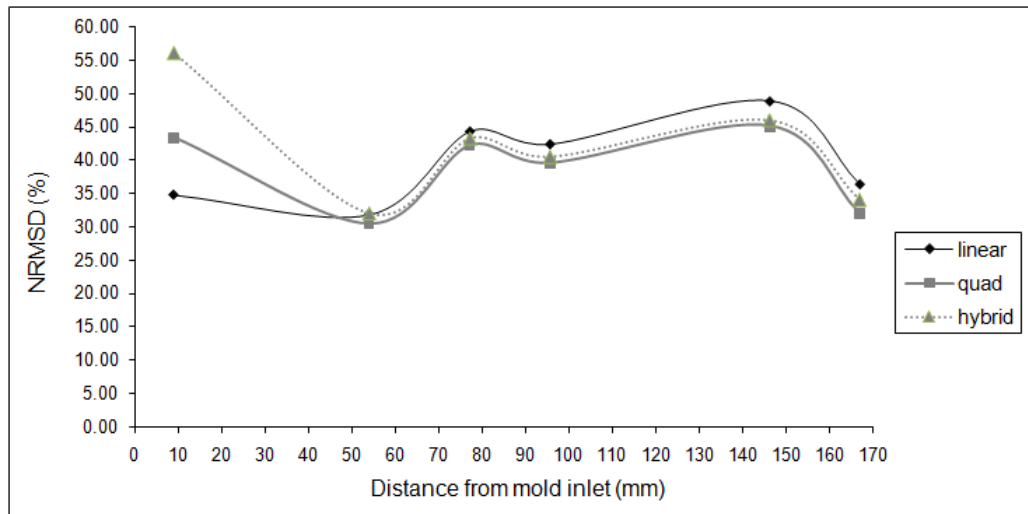

Fig. 6.27: The NRMSD of the computed a_{11} orientation tensor at distances from the mold inlet.
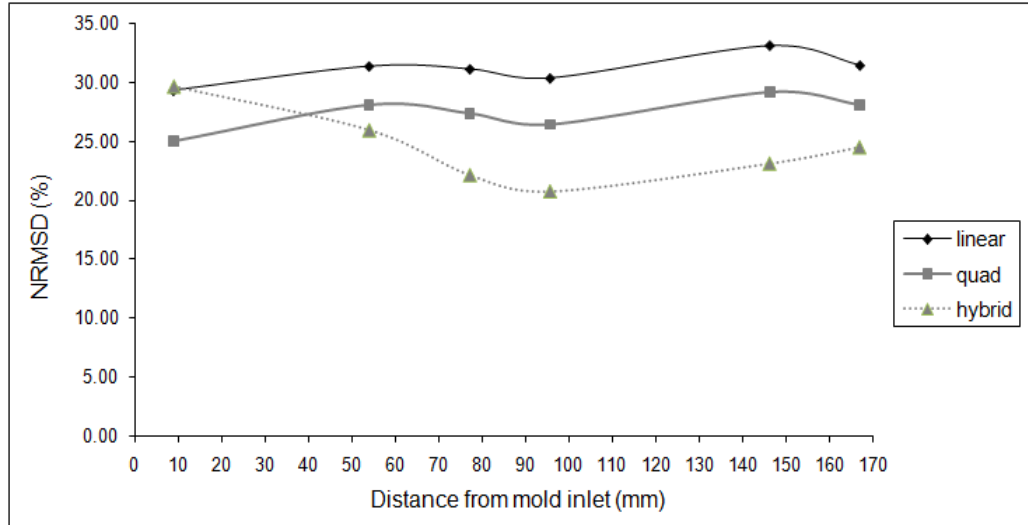

Fig. 6.28: The NRMSD of the computed a_{22} orientation tensor at distances from the mold inlet.
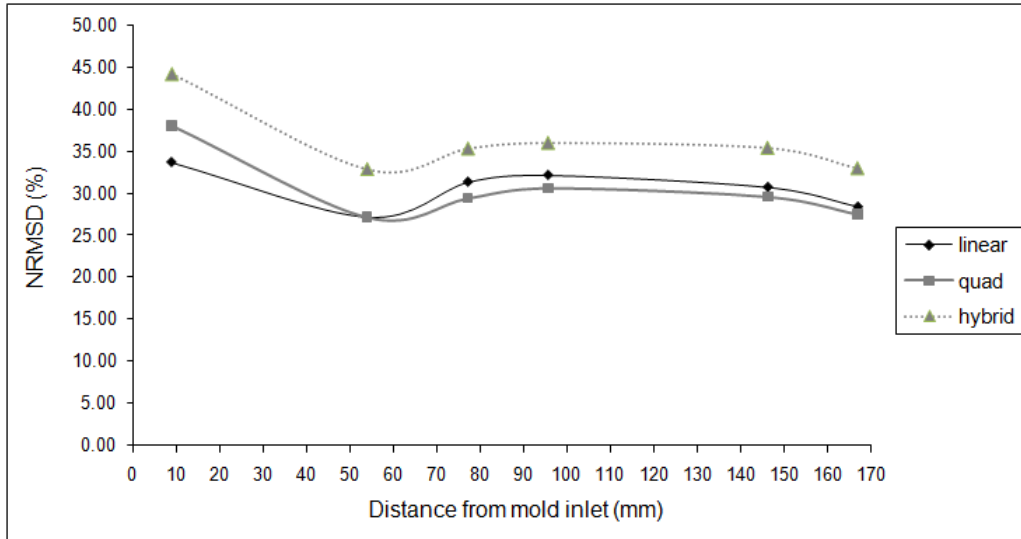
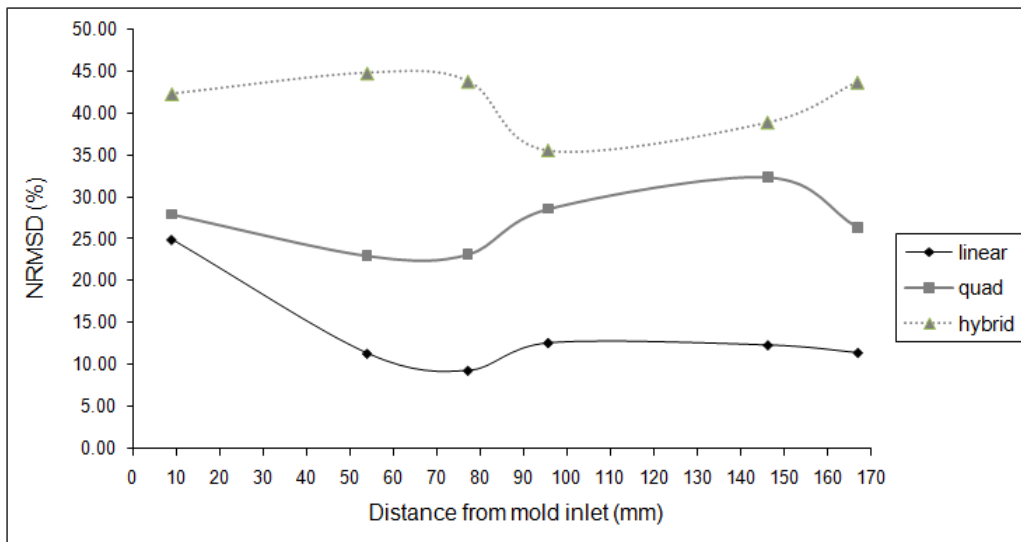Fig. 6.29: The NRMSD of the computed a_{33} orientation tensor at distances from the mold inlet.

Fig. 6.30: The NRMSD of the computed a_{13} orientation tensor at distances from the mold inlet.

114

6.3.4 Error Analysis

The discrepancies between the numerical and experimental data are analyzed in order to ascertain the probable causes. Closure model deficiencies and fiber-flow coupling effects have been identified as probable causes of these discrepancies and are discussed in the following sections. The effect of partial solidification of the suspension during the filling process on the flow field may be safely neglected as the flow has a Graetz number [21] of 1019.06. This analysis is demonstrated in Appendix K.

As the a_{11} component tensor is the dominant one here, deviations in the predicted values heavily affect the other component tensors. As mentioned earlier, there is considerable under-prediction of the a_{11} orientation in the regions at the core (0.001 to 0.0016m along the mold height) and in the skin (0 to 0.0002m and 0.003 to 0.0032m along the mold height) region. This may be visually confirmed by viewing Figures 6.15, 6.19 and 6.23. Further clarification of this point may be obtained from the figures in Appendix H, I and J. These are also areas where the fluid shearing in the flow direction is reduced. This highlights the possibility that the linear, quadratic and hybrid models do not work well with domains of the flow where fluid stretching is prominent. The suspension flow simulation predicts that the maximum strain rates occur at some distance away from the wall and they coincide with positions where the a_{11} orientation results match the experimental data well. Figure 6.31 presents the plots of a_{11} orientation results for the linear, quadratic and hybrid closure and the experimental data at the mold location 54mm from the inlet. Figure 6.32 presents the γ_{13} strain rate data (the dominant strain rate component in the flow direction across the mold height) at the same location.
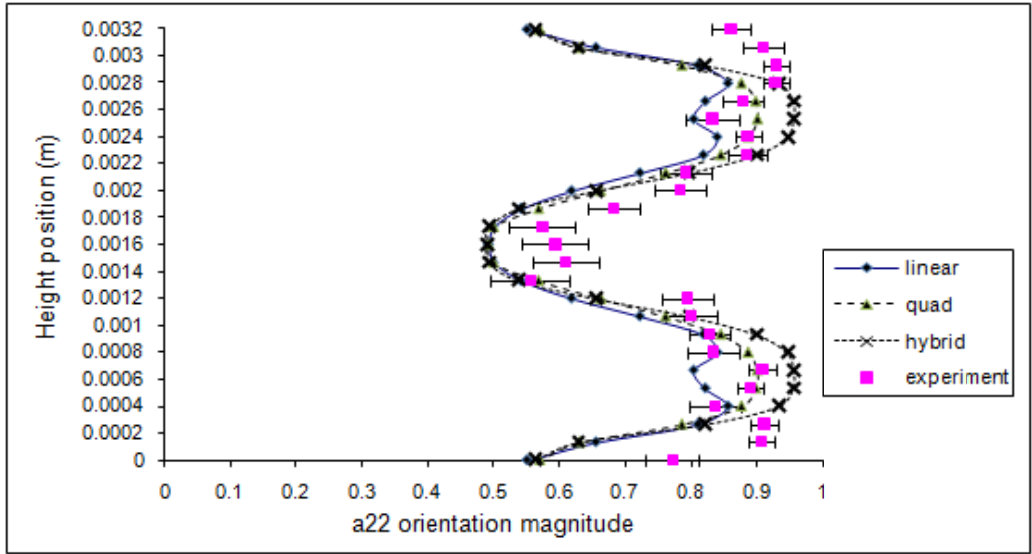
Fig. 6.31: a_{11} orientation tensor plots 54mm from the mold inlet
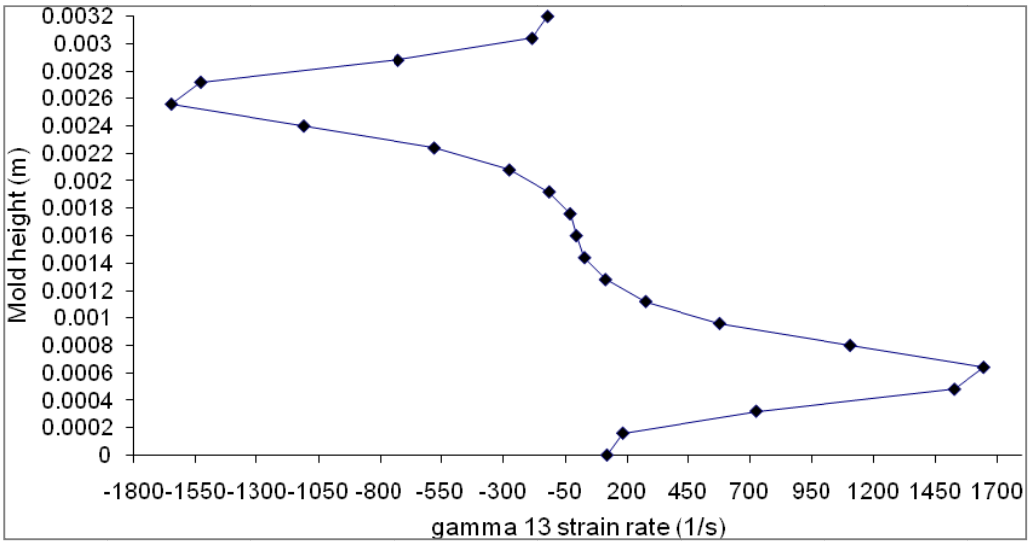
Fig. 6.32: γ_{13} strain rate data at the mold location of 54mm from the inlet.

As may be observed, the maximum γ_{13} strain rate coincides with the locations where the predicted a_{11} orientation is at a maximum and the degree of agreement between the numerical and experimental results is best. In the high strain rate regions, the hybrid closure noticeably over-predicts the a_{11} orientation. This behavior has also been observed in previous work [23, 58], where coupled analyses were performed. As this observation is made regardless of a coupled or decoupled analysis, it leads us to infer that the closure models themselves have in-built

116

inaccuracies and demonstrates the degree to which the mathematical formulation fails to capture the actual phenomena.

The a_{22} values are best predicted by the hybrid closure and a_{33} values by the quadratic closure, as seen in Figures 6.28 and 6.29. The discrepancy between the numerical and experimental results for these two orientation components may be attributed to the knock – on effect from the error in the a_{11} orientation prediction, where the considerable under – prediction of the a_{11} in the low shear regions, results in the over prediction of a_{22} and a_{33} which are linked directly to a_{11} through the normalization criteria described in Chapter 3.5.

For the hybrid closure, the discrepancy in the a_{13} values between measured and computed tensor values are noticeably greater than that of the linear and quadratic closure. Verweyst [13], who performed a coupled analysis with the same geometry, has noted that the hybrid closure predicts the a_{13} orientation reasonably well. However, in this work, this is not the case, although the predicted trend is stable and qualitatively agrees with the experimental results as seen in Figure 6.26. This may be due to coupling effects. The simulation results of the a_{13} tensor for the quadratic closure also follow the experimental results qualitatively as seen in Figure 6.22, although there is a constant deviation between the two sets of data. Compared to these two models, the performance of the linear closure is the best as the predicted a_{13} values agree well with the experimental results as shown in Figure 6.18, with the exception of values 9mm from the mold inlet. This deviation may be attributed to convection effects at the inlet. In addition, it may be observed that the maximum experimental a_{13} values typically occur near the middle of the flow as is the case at locations 54, 77, 96, 146 and 170mm from the inlet. As the a_{13} orientation describes the degree to which fibers are oriented in the x – z plane, thus it may be used as a measure of the size of the flow core [13]. As Figure 6.18 demonstrates, the peak a_{13} numerical values are further from the middle of the flow then the experimental values, thus they predict a larger core than the actual case.

As mentioned earlier, the justification for the de-coupling of the fiber orientation evolution equation from the suspension momentum equation was that a decoupled approach significantly eases implementation. However, there are consequences to this, which also help explain the discrepancies between the numerically computed

and experimental values. The coupling between the two sets of equations means that the fiber orientation affects the fluid momentum directly, via the local fluid shear stress. The presence of fibers creates resistance to fluid stretching [33] which in this case occurs near the core and skin region, contributing to an increase in viscosity. As fluid stretching increases the degree of orientation transverse to the flow direction (a_{22} and a_{33} components), resistance to stretching would serve to increase the degree of orientation in the flow direction (a_{11}) near the middle of the flow. Thus the under-prediction observed with the decoupled solution presented here is expected. This agrees with previous findings [25] that for the film-gate geometry, the fiber – flow coupling is significant in regions near the middle of the flow, and that this effect is reduced in the high shear regions.

6.4 Summary

The validation of the numerical setup of the mold-filling flow was successfully performed, where the velocity and temperature trends obtained agree with those from literature. An identical setup was used for the three-dimensional mold-filling simulation where it was observed that the interface progression of the filling mold was realistic. The velocity profiles obtained agreed with observations from literature, and the implementation of the dynamic slip model allowed for the capture of the fountain flow phenomena at the interface. In addition, it was found that the dynamic slip model allowed for savings in terms of computational resources. The numerical solution of the fiber orientation evolution equation was carried out with the implementation of the linear, quadratic and hybrid closure where it was found that the linear closure produced the best all round performance. The best agreement between the numerical and experimental data was observed in the shell zone, and significant under-prediction of the a_{11} orientation was observed in the core and skin layer for all the closure models.

CHAPTER 7

CONCLUSIONS

In this work, a simulation of the fiber orientation evolution encountered in a mold-filling process was done. For a non–isothermal, laminar, three-dimensional simulation of mold-filling flow, the velocity and temperature results of the simulation demonstrated agreement with the validation case. From the grid independence tests carried out, it was further concluded that the application of the dynamic slip condition resulted in an accurate simulation which was cheaper computationally as compared to one carried out with the traditional no-slip boundaries applied to both phases. As for the simulation of the decoupled fiber orientation equation, it was found that the linear closure model demonstrated the best overall performance of the three closures tested. This finding is limited to the film-gated strip mold geometry, characterized by a large length to height ratio, thus the findings are not readily extended to arbitrary mold geometries, where the flow conditions may differ significantly from the one under study here. The dominant orientation tensor, a_{11} was found to produce results in agreement with the experimental data for all three closure models and the performance of all three closure models was similar as the deviation trends were close together. The quality of numerical predictions of the non-dominant components a_{22}, a_{33} and a_{13} were consistent with those observed for the a_{11} component, however the deviation ranges were considerably broader especially for the a_{13} component. The quality of the numerical predictions were also found to vary with respect to the mold height, where it was observed that the fiber orientation simulation accuracy was highest in regions of high fluid shear (shell) and lowest where extensional flow dominated (skin and core). This observation agrees with other findings from literature.

7.1 Recommendations and Future Work

Throughout the research work, several areas have been highlighted in which improvements can be made in order to improve the quality of the numerical simulation of the fiber orientation evolution during the mold-filling process.

First, a strict adherence to the scaling analysis performed by Tucker [35], described in the introduction of this theses imply that with exception to a very narrow selection of actual mold-filling cases, the decoupling of the fiber orientation from the suspension momentum equation compromises the results quality. Thus, expanding the current fiber orientation solution algorithm to complex mold geometries as encountered in the industry will require the development of a three dimensional coupled solver. A coupled solver would also be required to address heavily time-dependant flow problems.

Second, the use of bounding functions to restrict blow-up in the numerical solution of the fiber orientation evolution equation as used in this theses reveals the high sensitivity to values outside its defined domain. This could be resolved through the use of a fully implicit solver utilizing very small time steps, as well as heavy under-relaxation in the solution algorithm.

Third, improved closure models such as the natural and orthotropic closure described in the introduction of this thesis may be applied in order to improve the prediction of fiber orientation especially in regions of low fluid shear. In addition, direct solution of the Fokker-Planck equation for fiber orientation for a broader case of flow problems should also be a real possibility given the improvement in computing power expected in the coming years.

Last, the post-filling effects of solidification and packing definitely affect the fiber orientation once the mold is fully filled and allowed to cool. This presents an unknown source of error to mold-filling simulations that only account for the filling phase of the process as there would be deviations between the predicted results and the orientation of the final, finished piece. Thus, in order to develop an accurate code to simulate the fiber orientation evolution during the mold-filling process, as well as to apply these results in the industry, the post-filling effects have to be modeled as well.

REFERENCES

[1] J. Azaiez, K. Chiba, F. Chinesta and A. Poitou. "State-of-the-Art on Numerical Simulation of Fiber-Reinforced Thermoplastic Forming Processes." *Arch. Comput. Meth. Engng.* Vol. 9, 141-198, February 2002

[2] D. Guell and A. Benard. "Flow-induced alignment in composite materials: current applications and future prospects" in *Flow-induced Alignment in Composite Materials*, Eds. T.D Papanathasiou and D. C. Guell, Woodhead Publishing Ltd, 1997, pp 1-34.

[3] R. Brooks. "Materials property modeling and design of short fibre composites," in *Flow-induced Alignment in Composite Materials*, Eds. T.D Papanathasiou and D. C. Guell, Woodhead Publishing Ltd, 1997, pg. 293-321.

[4] M. J. Folkes. *Short Fibre Reinforced Thermoplastics.* Research Studies Press, 1984, pg. 101

[5] T.D. Papanathasiou. "Flow – induced alignment in injection molding of fibre – reinforced polymer composites," in *Flow-induced Alignment in Composite Materials*, Eds. T.D Papanathasiou and D. C. Guell, Woodhead Publishing Ltd, 1997, pg. 112.

[6] P.F Bright, R.J Crowson and M.J Folkes. "A study of the effect of injection speed on fibre orientation in simple mouldings of short glass fibre-filled polypropylene." J. Mat. Sci., Vol. 13, pp. 2497-2506, 1978.

[7] C. Lhymm and J.M. Schultz, "Fracture of glass-fibre reinforced poly(phenylene sulphide)," *J. Mater. Sci. Letters*, Vol. 4, pp.1244-1248, 1985.

[8] M.W. Darlington and A.C. Smith, "Some features of the injection molding of short fiber reinforced thermoplastics in center sprue – gated cavities," *Polym. Compos.* Vol. 8(1), pp. 16-21, 1987.

[9] R.S. Bay and C.L. Tucker III, "Fiber orientation in simple injection moldings. Part 2: Experimental results," *Polym. Compos.* Vol. 13, pp. 317-321, 1992b

[10] G.B. Jeffery, "The Motion of Ellipsoidal Particles Immersed in a Viscous Fluid." *Proceedings of the Royal Society of London.* Series A, Vol. 102(No. 715), 1922, pp. 161-179.

[11] F.P Bretherton, "The motion of rigid particles in a shear flow at low Reynolds number," *J. Fluid Mech.*, Vol. 14, 284 - 304, 1962

[12] S. Ranganathan and S.G. Advani, "Fiber – fiber and fiber – wall interactions during the flow of non – dilute suspensions in *Flow-induced Alignment in Composite Materials*, Eds. T.D Papanathasiou and D. C. Guell, Woodhead Publishing Ltd, 1997, pg. 43.

[13] B E. Verweyst "Numerical predictions of flow induced fiber orientation in three dimensional geometries" PhD thesis, University of Illinois at Urbana-Champaign, Urbana, IL (1998).

[14] N. Phan – Thien and R. Zheng , "Macroscopic modeling of the evolution of fibre orientation during flow in *Flow-induced Alignment in Composite Materials*, Eds. T.D Papanathasiou and D. C. Guell, Woodhead Publishing Ltd, 1997, pg. 43.

[15] P.J. Krochak, J.A. Olson and D.M. Martinez, "Fiber suspension flow in a tapered channel: The effect of flow/fiber coupling," *International Journal of Multiphase Flow*, Vol. 35, 7, pp. 676-688, 2009.

[16] J.Ferec, M. Heniche, M.C. Heuzey, G. Ausias and P.J. Carreau, "Numerical solution of the Fokker-Planck equation for fiber suspensions: Application to the Folgar-Tucker-Lipscomb model," *Journal of Non-Newtonian Fluid Mechanics*, Vol. 155, pp. 20-29, 2008.

[17] F. Chinesta, G. Chaidron and A. Poitou, "On the solution of Fokker-Planck equations in steady recirculating flows involving short fiber suspensions," *Journal of Non-Newtonian Fluid Mechanics*, Vol. 113, pp. 97-125, 2003.

[18] E.J. Hinch and L.G. Leal, "Constitutive equations in suspension mechanics. Part 1", *J. Fluid. Mech.*, Vol. 71, 3, pp. 481-495, 1975.

[19] E.J. Hinch and L.G. Leal, "Constitutive equations in suspension mechanics. Part 2: Approximate forms for a suspension of rigid particles affected by Brownian rotations", *J. Fluid Mech.,* Vol. 76, 1, pp. 187-208 , 1976.

[20] S.G. Advani and C.L. Tucker III, "The use of tensors to describe and predict fiber orientation in short fiber composites", J. Rheol., Vol. 31, 751-784, 1987.

[21] R.S. Bay,"Fiber orientation in simple injection moldings. Part 1: Theory and numerical methods," *Polym. Compos.,* Vol. 13(4), pp 317 – 331, 1992a

[22] S. T. Chung and T. H. Kwon, "Numerical simulation of fibre orientation in injection molding of short – fibre – reinforced – thermoplastics." *Polym. Eng. Sci.,*Vol.35 , pp 604 – 618, 1995.

[23] D.H Chung and T.H Kwon, "Fiber orientation in the processing of polymer composites" *Korea-Australia Rheology Journal,* Vol. 14(4), pp. 175-188, 2002.

[24] D. H. Chung and T. H. Kwon, "Applications of recently proposed closure approximations to injection molding filling simulation of short-fiber reinforced plastics," Korea-Australia Rheology Journal, Vol. 12, No. 2, pp. 125-133, 2000.

[25] D.H Chung and T.H. Kwon, "Numerical studies of fiber suspensions in an axisymmetric radial diverging flow: the effects of modelling and numerical assumptions," *J. Non-Newtonian Fluid Mech.* Vol. 107, pp. 67–96, 2002.

[26] G.L. Hand, "A Theory of Anisotropic Fluids *J. Fluid. Mech*, Vol. 13, pp 33-46, 1962.

[27] L.G. Leal and E.J. Hinch , " Theoretical studies of a suspension of rigid particles affected by Brownian couples," Rheol Acta, Vol. 12, pp. 127-132, 1972.

[28] S.G. Advani and C. L. Tucker III, "Closure approximations for three-dimensional structure tensors", *J. Rheol.* Vol. 34,3, pp. 367-386, 1990.

[29] R.S. Bay."Fiber orientation in injection molded composites: a comparison of theory and experiment." PhD thesis, University of Illinois at Urbana-Champaign, Urbana, IL (1991).

[30] B.E. Verweyst and C.L. Tucker III (2002), "Fiber Suspensions in Complex Geometries: Flow/Orientation Coupling," The Canadian Journal of Chemical Engineering, Vol. 80, pp. 1093-1106

[31] J.S. Cintra, Jr and C.L. Tucker III. "Orthotropic closure approximations for flow-induced fiber orientation," *J. Rheol*. Vol. 39, 6, pp. 1095-1121, 1995.

[32] F. Dupret and V. Verleye, "Numerical Prediction of Fiber Orientation in Complex Injection Molded Parts," *Proc. of the ASME Winter Annual Mtg.* MD-Vol 49. HTD-Vol283, pp.264-279, 1994

[33] G.G Lipscomb, M.M. Denn, D.U. Hur and D.V. Boger. "The flow of fiber suspensions in complex geometries." *J. Non-Newtonian Fluid Mech*., Vol. 26, pp. 297-325, 1988

[34] Dinh S.M. and R.C. Armstrong, " A Rheological Equation of State for Semiconcentrated Fiber Suspensions." *J. Rheol.* Vol. 28, 3,pp. 207-227, 1984.

[35] C.L. Tucker, "Flow regimes for fiber suspensions in narrow gaps." *J. Non-Newtonian Fluid Mech.*, Vol. 39, pp 239-268, 1991.

[36] F.P. Folgar, C.L. Tucker III, "Orientation behavior of fibers in concentrated suspensions," *J. Reinforced Plastics Composites*, Vol. 3, pp. 98-119, 1984

[37] C.F. Hung and Y.K. Shen, "Numerical simulation of fiber orientation in injection mold filling," *Int. Comm. Heat Mass Transfer*, Vol. 22(6), pp. 791 – 802, 1995.

[38] C.A. Hieber, S.F. Shen, "A finite-element/finite-difference simulation of the injection-molding filling process", *J. Non-Newtonian Fluid Mech*. Vol. 7, pp. 1–32, 1980.

[39] C.A. Hieber , "Melt Viscosity Characterization and Its Application to Injection Molding, in: Injection and Compression Molding Fundamentals," A.I. Isayev, Eds. Marcel Dekker, New York, 1997.

[40] A.Caboussat, "Numerical Simulation of Two-phase Free Surface Flows," *Arch. Comput. Meth. Eng.* Vol. 12, 2, pp. 165-224, 2005.

[41] S. Ranganathan, "Mechanics of fiber -fiber interactions during the flow of non-dilute short fiber suspensions." PhD thesis, University of Delaware, Newark, DE 1993

[42] J. Ferziger and M. Peric . *Computational methods for fluid dynamics*. 3rd. ed, Springer – Verlag, 2002

[43] H. K. Versteeg and W. Malalasekera. *An introduction to computational fluid dynamics: the finite volume method.* Longman Scientific and Technical, pg. 135 – 155, 1995.

[44] J.D. Anderson, Jr.*Computational fluid dynamics: the basics with applications*. McGraw – Hill, 1995

[45] Patankar, S.V. and D.B. Spalding, "A calculation procedure for heat, mass and momentum transfer in three-dimensional parabolic flows", *Int. J.Heat Mass Transfer*, Vol. 15, pp. 1787-1806, 1972

[46] C.W. Hirt, B.D. Nichols, "Volume of Fluid (VOF) method for the dynamics of free boundaries," *J. Comput. Phys.,* Vol. 39, pp. 201–225, 1981

[47] S. Muzaferija, M. Peric, P. Sames, T. Schelin, "A two-fluid Navier-Stokes solver to simulate water entry," *Proc. Twenty-Second Symposium on Naval Hydrodynamics*, 1998

[48] Leonard BP, "The ULTIMATE conservative difference scheme applied to unsteady one-dimensional advection.," *Comput Math Appl Mech Eng,* Vol. 88, pp. 17–74, 1981

[49] G.A.A.V Haagh, F.N. Van De Vosse. "Simulation of three-dimensional polymer mould filling processes Using a Pseudo-Concentration Method," Int. J. Numer. Meth. Fluids, Vol. 28, pp. 1355–1369, 1998.

[50] C. Huh, L.E. Scriven. "Hydrodynamic model of steady movement of a solid/liquid contact line," *Journal of Colloid and Interface Science* Vol..35, 1, pp. 85 – 101, 1971

[51] User Inputs for Time-Dependent Problems 25.17.1, FLUENT User Manual, Fluent. Inc. 2009

[52] W. H. Press, S.A. Teukolsky, W.V. Vetterling, B.P. Flannery, *Numerical recipes: the art of scientific computing.* 3rd ed. Pg 1045, 2007

[53] S.C. Chapra and R.P. Canale.*Numerical methods for engineers.* 4th ed. McGraw – Hill International edition, pg. 289, 2003

[54] B.E. Verweyst, C.L. Tucker III, and P.H. Foss. "The optimized quasi-planar approximation for predicting fiber orientation in injection-molded composites," *Int. Polym. Process.* Vol. 12, 3, pp. 238-248, 1997.

[55] G.P. Galdi and B.D. Reddy. "Well-posedness of the problem of fiber suspension flows," J. Non-Newtonian Fluid Mech., Vol. 83, pp. 205–230, 1999.

[56] Z.Tadmor, C.G. Gogos. *Principles of polymer processing.* 2nd edition, John Wiley & Sons, pg. 767, 2006

[57] R.Y Chang, W.H Yang, "Numerical simulation of mold filling in injection molding using a three-dimensional finite volume approach," *Int.J.Numer. Meth. Fluids,* Vol. 37, pp. 125–148, 2001

[58] D.H Chung and T.H Kwon. "Improved closure approximation for numerical simulation of fiber orientation in fiber – reinforced composite," *The Korean Journal of Rheology*, pp. 202-216, 1998

[59] FLUENT User Manual, Fluent. Inc. 2009

[60] " File:Injection molding.png." Wikipedia, The Free Encyclopedia. Wikimedia Foundation, Inc. 22 , February 2009. Web. 22 January 2011.

124